TITLE

Development in context: interferon response networks regulate human fetal thymic epithelial cell differentiation

AUTHORS

Abdulvasey Mohammed,[1] Benjamin D. Solomon,[2] Priscila F. Slepicka,[1] Kelsea M. Hubka,[1] Hanh Dan Nguyen,[1] Wenqing Wang,[1] Martin Arreola,[1] Michael G. Chavez,[3] Christine Y. Yeh,[4] Doo Kyung Kim,[3] Virginia Winn,[5] Casey A. Gifford,[6] Veronika Kedlian,[7] Jong-Eun Park,[7] Georg A. Hollander,[8] Vittorio Sebastiano,[5] Purvesh Khatri,[9] Sarah A. Teichmann,[7] Andrew J. Gentles,[4, 10*†] and Katja G. Weinacht,[1*†]

AFFLILATIONS

[1] Department of Pediatrics, Division of Stem Cell Transplantation and Regenerative Medicine, Stanford School of Medicine, Stanford CA, USA

[2] Department of Pediatrics, Division of Allergy and Immunology, Stanford School of Medicine, Stanford CA, USA

[3] Department of Bioengineering, Stanford University, Stanford, CA, USA

[4] Department of Biomedical Data Science, Stanford University, Stanford, CA, USA

[5] Department of Obstetrics and Gynecology, Stanford School of Medicine, Stanford CA, USA

[6] Department of Pediatrics, Division of Cardiology, Stanford School of Medicine, Stanford CA, USA

[7] Wellcome Sanger Institute, Cambridge, UK

[8] Department of Pediatrics and Institute of Developmental and Regenerative Medicine, University of Oxford, Oxford, United Kingdom

[9] Institute for Immunity, Transplantation, and Infection, Stanford University, Stanford, CA, USA.

[10] Department of Pathology, Stanford School of Medicine, Stanford, CA, USA

*Corresponding authors. Email: Katja G. Weinacht, kgw1@stanford.edu; Andrew J. Gentles, andrewg@stanford.edu

†These authors contributed equally to this work

ABSTRACT

The thymus instructs T cell immunity and central tolerance, yet its therapeutic potential remains untapped. The quest to regenerate thymic function for clinical application is lagging while the signals that drive thymic epithelial cell differentiation remain incompletely understood. Here, we elucidate pathways instructing commitment and specialization of the human thymic epithelial stroma through complementary single cell transcriptomic approaches. First, we identify gene regulatory networks that define fetal thymic epithelium in the thus far unexplored context of other anterior foregut-derived organs; then, we characterize lineage trajectories within the thymic epithelial compartment across embryonic, fetal, and early postnatal stages. Activation of interferon response gene regulatory networks distinguished epithelial cells of the thymus from those of all other anterior foregut-derived organs. Interferon signals were processed differentially within thymic cortical and medullary lineages, reflected in distinct *NFκB* and *IRF* signatures, respectively. Our study reveals novel, translatable insights into the developmental programs underlying thymic epithelial cell differentiation that may advance the field of regenerative cell therapies.

SUMMARY

Single cell transcriptomics of anterior foregut-derived organs identifies pathways governing thymic epithelial commitment and specialization.

INTRODUCTION

The thymic epithelium comprises a highly specialized set of cells that attract lymphoid progenitors, promote their proliferation and maturation into thymocytes, and facilitate the selection of a diverse, self-tolerant T cell receptor repertoire[1-4]. As such, the thymus is central to the development of the adaptive immune system. Thymic function naturally declines in the second decade of life[5]. In addition, thymic output is susceptible to a wide range of pathogenic insults including medications, radiation, infection and graft-versus-host disease[2,3,6,7]. Endogenous or acquired thymic compromise leads to immunodeficiency, autoimmunity and inflammation[7-9]. Regenerating thymic function, such as through induced pluripotent stem cell (iPSC)-derived thymic epithelial cells, holds great therapeutic promise.

The thymus is derived from the anterior foregut endoderm. During development, the anterior foregut gives rise to the ventrally located respiratory system and the dorsally located esophagus[10]. The anterior-most segment of the foregut develops into the pharyngeal apparatus. Essential to the development of the mammalian pharyngeal apparatus is the out-pocketing of the pharyngeal pouches[11]. The thymic primordium, also referred to as thymus anlage, forms from the ventro-caudal region of the third pharyngeal pouch, while the dorsal aspect gives rise to the parathyroid (Fig. 1A). The signals that induce iPSCs into anterior foregut endoderm have long been described and protocols to differentiate anterior foregut endoderm further into epithelial cells of lung and esophagus *in vitro* have successfully been established[12-17]. Recent studies of murine and human thymus using single cell transcriptomics have greatly expanded our understanding of thymic epithelial cell (TEC) diversity[18-27], yet the signals that drive TEC fate

beyond the anterior foregut stage remain incompletely understood. Elucidating these signals is essential to derive TECs from iPSCs in an effort to enable regenerative cell therapies.

In human embryonic samples, the third pharyngeal pouch transcriptional regulators HOXA3, PAX9, TBX1 and FOXG1 are detected as early as the beginning of post conception week (pcw) 6 and precede the expression of the master thymic transcription factor FOXN1 mid-week 6[28]. Lymphoid progenitors enter the thymus anlage as early as pcw 7[21,28]. At pcw 8, less than 5% of cells in the developing human thymus are of hematopoietic origin ($CD45^{+}$)[23]. In contrast, by pcw 10, more than 90% of cells in the thymus are of hematopoietic orgin[23], highlighting the dramatic expansion of thymocytes (i.e. immature T cell precursors) and other immune cells during thymic development.

Important insights into the developmental programs that instruct thymic organogenesis have been derived from mice with biallelic loss of function mutations in Foxn1, which result in an athymic and hairless (nude) phenotype[29,30]. Thymic development in nude mice arrests before colonization with lymphoid progenitors occurs[31,32]. The thymic rudiment of $Foxn1^{null}$ mice displays nonfunctional cystic features strongly resembling respiratory epithelium in morphology and gene expression. It has therefore been suggested that Foxn1 overwrites respiratory cell fate as the default pathway in the anterior foregut[32-35]. Notably, NOD-scid $IL2Rg^{null}$ (NSG) mice with genetically impaired immune functions of hematopoietic origin leading to a lack of thymocytes also display distorted thymic architecture with cystic features resembling respiratory epithelium[36]. Although NSG mice do not have cell-intrinsic genetic defects in thymic epithelial cell differentiation, they often exhibit permanently impaired thymic function leading to poor T

cell reconstitution even if healthy hematopoietic stem cells are transplanted later in life[36,37]. This suggests that Foxn1 is necessary but not sufficient to fully induce thymic epithelial cell fate. While thymic defects in NSG mice[36] support that development of thymic epithelial and lymphoid niches during embryogenesis are intertwined, the corresponding gene regulatory networks governing the lymphoid-driven commitment and maturation of the thymic epithelial stroma have not yet been characterized.

Here we identify regulators underlying thymic epithelial differentiation by comparing epithelial cells from human fetal organs of shared anterior foregut origin (thymus, bronchus, lung, esophagus and parathyroid) using single cell transcriptomics. We characterize developmental programs unique to specific TEC subsets by analyzing human samples from embryonic, fetal, and early postnatal stages. Our studies yield translatable insights designed to advance regenerative cell therapy approaches.

RESULTS

Human fetal anterior foregut-derived organs at single cell resolution

Single cell RNA-sequencing (scRNA-seq) was performed on 17 samples from 15 distinct biological specimens. For the comparison of human fetal anterior foregut-derived organs, we sampled midgestation tissues from thymus (pcw 16, 17, 18), airway/bronchus (pcw 16, 17, 18), lung parenchyma (pcw 16, 17,18) and esophagus (pcw 16 and 17). We refer to the comparison of different tissues from the same stage of development as *horizontal* comparison. We also performed *vertical* comparisons between human thymus samples obtained during early gestation (pcw 6, 7), midgestation (pcw 16, 17, 18) and postnatally (age 3 months) to examine lineage

trajectories and epithelial cell diversification within the thymus (Fig. 1A). The earliest thymus samples were used unmanipulated due to very low numbers of thymocytes at this stage of development. At later stages, thymic samples were depleted of $CD45^+$ thymocytes. All samples were then enriched for $EPCAM^+$ epithelial cells (Fig. 1B). Sample characteristics are summarized in Supplementary Table S1.

Preprocessing and integration of scRNA-seq samples using Seurat yielded a dataset of 52,162 single cell transcriptomes with a mean of 3522 unique genes per cell, and an average of 14,839 total counts per cell. Cells within unsupervised clusters were annotated in concordance with previously published human single cell datasets for thymus[21], respiratory system[38,39] and esophagus[40], respectively.

In fetal thymus, we identified 18 epithelial and non-epithelial cell populations (Fig. 1C). Epithelial cells included cortical thymic epithelial cells (cTEC) and medullary thymic epithelial cells (mTECI). An intertypic mcTEC[21] population with dim expression of cTEC and mTEC markers and uniquely high expression of *CTGF* and *DLK2,* was the third most abundant population. mTECII were characterized by high expression of *AIRE* and *CLDN4*. The medullary TEC subpopulations mTECIII and mTECIV were defined by expression of *KRT1* and *POU2F3,* respectively, which correspond to the post-*AIRE* keratinocyte-like mTEC and Tuft cells in the mouse[19,20,41,42]. The recently characterized neuroendocrine (TECneuro) and muscle-like (TECmyo) TEC populations were also observed[21]. Immune cell clusters within the thymus included a spectrum of developing thymocytes from double-negative (DN) through double-positive (DP) thymocytes to single-positive stages, thymus-resident macrophages and dendritic

cells. Other nonepithelial clusters included vascular smooth muscle cells, aldehyde dehydrogenase-positive fibroblasts (thymic fibroblasts type 1[21]), fibronectin-high fibroblasts (thymic fibroblasts type 2[21]), vascular endothelial cells, lymphatic endothelial cells and neuronal cells (Fig. 1C, D and fig. S1).

Tissues of the bronchus clustered into airway epithelial basal cells and epithelial cells from the adjacent respiratory parenchyma. In addition, the airway microenvironment was comprised of immune cells (B cells, T cells), myoepithelial cells, smooth muscle, vascular smooth muscle, fibroblasts, cartilage, endothelial cells and neuronal cells. Lung tissue expectedly shared many of the same cell types surrounding the airway, albeit in reverse ratios. Cell types not derived from the foregut included neuroendocrine cells, immune cells (B cells, T cells, macrophages), fibroblasts, mesothelial cells, vascular smooth muscle cells, smooth muscle cells, endothelial cells, lymphatic endothelial cells and neuronal cells. The esophageal tissue included epithelial basal cells, suprabasal epithelial and gastric epithelial cells. Nonepithelial cells of the esophagus were comprised of immune cells (T cells, macrophages), smooth muscle, vascular smooth muscle, fibroblasts, endothelial cells and a cluster of neuronal cells (Fig. 1C, D and fig. S1). All identified cell pollutions and their defining markers are summarized in Supplementary Table S2.

Integrated data sets from thymus, bronchus, lung and esophagus revealed shared epithelial, mesenchymal, immune, endothelial, myoepithelial and neuronal clusters regardless of organ of origin (Fig. 1E and fig. S2). To investigate human thymic epithelial fate in the thus far unexplored context of developmentally related epithelia, we subclustered epithelial cells from all anterior foregut-derived organs and identified top differentially expressed genes unique to the

thymus. Expectedly, we detected key markers of thymic development and function, including *PAX1*, *PRSS16, CCL19, CCL25, TBATA*. Unexpectedly, we discovered numerous interferon-inducible or interferon-modulating genes including *IRF1, IFI6, IFI27, IFIT3, MX1, ISG15* and *NFKBIA* with uniquely high expression in epithelial cells of the thymus, raising the possibility that interferon (IFN) exerts unique effects in the developing thymus.

Selective IFN response network activation in TECs

IFNs induce cell intrinsic programs mediating a wide range of biological responses, e.g. through the JAK-STAT pathway[43-45] and NF-κB[46]. To explore the role of IFN signaling during thymic development, we investigated gene regulatory networks across anterior foregut-derived epithelial cells using the single cell regulatory network inference and clustering algorithm SCENIC[47, 48]. Modules, composed of a transcription factor and its inferred targets, are in the following referred to as regulons. UMAP visualization of organ-specific regulon expression distinctly separated the thymic epithelium from epithelial cells of bronchus, lung and esophagus (Fig. 2A). Across all epithelial cells, top differentially expressed regulons specific to the thymus encompassed a broad selection of inflammatory response regulators including IFN regulatory factors (*IRF1, IRF4, IRF6, IRF7, IRF9)*, signal transducer and activator of transcription factors (*STAT1, STAT2, STAT3, STAT5A*), nuclear factor-κB (NF-κB) complex components or modifiers thereof (*NFKB1, NFKB2, RELB, NFATC2, HIVEP1*[49]*)*, and additional modulators of inflammatory response signaling such as *BHLHE40*[50] and *BATF*[51]. Also identified were the key regulators of thymic patterning and development, *FOXN1*, *PAX9*, *FOXG1*[28] and *TP63*[52] (Fig. 2B).

To investigate interactions between individual regulons, a global network of significant connections was constructed using the Leiden algorithm[53,54,55]. This process delineated 7 unique subnetworks (A-G) for which linkage is inferred (Fig. 2C and fig. S3). Modular expression of the transcription factors defining these subnetworks demonstrated organ and cell type specificity for select subnetworks (A-C) while others were broadly shared between organ systems (D-G) (Fig. 2D). Subnetworks A and B were unique to the thymus with subnetwork A defining the primary TEC populations cTEC, mcTEC and mTECI while subnetwork B defined mTECII, mTECIII/IV and TECneuro. Subnetwork A linked the IFN regulatory factor regulons *IRF1, IRF3, IRF7, IRF8* and *IRF9* with the STAT family regulons *STAT1, STAT2, STAT3 STAT5A,* and *STAT6,* the NF-κB family regulons *NFKB1, NFKB2, REL, RELA, RELB,* and the NF-κB modulators *HIVEP1*[49] and *BHLHE40*[50], all of which either transmit or modulate the cellular response to IFNs (Fig. 2E). *IRF8, IRF1* and *NFKB1* regulons comprised most of the interactions found in subnetwork A through co-expression with numerous additional *IRF*-, *STAT*-, and NF-κB-associated regulons unique to thymic epithelium. Notably, the developmental thymic transcription factors *FOXN1* and *FOXG1* were also part of the IFN response-centric subnetwork A and inferred targets of *IRF1* and *IRF8* (Fig. 2E). A biological association between *FOXG1* and IFN signaling has recently been made by a report describing that congenital viral infections recapitulate the spectrum of birth defects found in congenital *FOXG1* syndrome[56]. Together, these observations suggest that an intricate network of IFN regulated signaling pathways is selectively activated during TEC development but not in epithelial cells of other anterior foregut-derived organs.

IFN responses in TECs increase with developmental age

To investigate if alternate methods of analysis would also demonstrate evidence of increased IFN response signaling in the thymic epithelium, we performed Gene Set Enrichment Analysis (GSEA) on select anterior foregut-derived epithelial clusters: mcTEC, cTEC, mTECI, mTECII, bronchial epithelial basal cells, esophageal epithelial basal cells and lung bud tip progenitor cells (Fig. 3A). GSEA network visualization of positively enriched gene sets revealed three main clusters (Fig. 3B and fig. S4, S5A). Within the cTEC/mTECI/mTECII cluster, mTECI was highly enriched for genes involved in IFN signaling, cytokine immune signaling, and antigen presentation. Gene sets with core enrichment of MHC genes constituted the remainder of gene sets within the cluster and were enriched in both cTEC and mTECII (Fig. S5B). In a separate cTEC-specific cluster, genes involved in TCR signaling, proteasome peptide processing, cross presentation of exogenous antigens, and IL-1 signaling were enriched. Enrichment of ribosomal and translational gene sets was shared between mcTEC, esophageal epithelial basal and lung bud tip progenitors. To gain a more granular understanding of the effects induced by IFNs we interrogated enriched IFN signaling gene sets for the most differentially expressed genes (Fig. 3C). In addition to the previously noted regulators and transducers of IFN signaling, cTEC, mTECI and mTECII exhibited differential expression of MHC class I and II genes, as well as the IFNγ receptor genes *IFNGR1* and *IFNGR2*. Notably, MHC class I and II are upregulated by IFNγ[57].

IFNα and IFNβ are type I IFNs, IFNγ represents type II IFN[43,58]. To establish a quantifiable measure of IFN responses across queried cell types, we integrated IFN response gene sets into type I and II IFN specific expression modules, hereby referred to as module I and II. At midgestation (pcw 16-18), module I showed highest expression in mTECI while mTECII showed highest expression of module II. In contrast age-matched epithelial cell populations from

bronchus, lung and esophagus showed significantly reduced expression across both modules (Fig. 3D). Early in gestation (pcw 6-7), mcTEC, cTEC, mTECI and mTECII showed higher expression of modules I and II relative to age-matched parathyroid epithelial cells (PTEC) (Fig. 3E). When compared longitudinally across samples of advancing gestational ages, modules I and II demonstrated an increasing trajectory over time (Fig. 3F) paralleling the age-dependent increase in the number of immune cells in the developing thymus.

Antigen presenting cells such as dendritic cells and macrophages are widely recognized producers of type I IFN[59]. Activated T cells, together with NK cells, are widely recognized as producers of type II IFN[60], yet less is known about the capacity of developing T cells to produce type II IFN during human thymopoiesis. To investigate a possible link between the expansion of the lymphoid niche and the increase in type II IFN response in the thymic epithelium over time, we sought to quantify the relative contributions of immune and stromal cells to the production of *IFNG*. Because *IFNG* as well as *IFNA1, IFNA2* and *IFNB1* single cell transcripts largely evaded detection across our data set, we performed bulk RNA-sequencing on magnetic bead-enriched fractions of thymocytes, TEC, bronchial epithelial cells and lung epithelial cells. Thymocyte samples expressed notably higher levels of *IFNG* than epithelial cells from thymus, bronchus or lung suggesting thymocytes were primary producers of IFNγ in the thymus (Fig. 3G). The increase in IFN response during development combined with the higher expression of *IFNG* in thymocytes points to IFNγ as a mediator of the lymphoid-driven maturation of the thymic epithelium.

Modifiers of IFN responses in thymic epithelial subsets

To examine TEC diversification throughout development we integrated TECs from samples of subsequent gestational ages (pcw 6, 7, 16, 17, 18) and 3 months post birth (*vertical* integration). UMAP visualization revealed a new TEC cluster in spatial proximity to mcTEC (Fig. 4A and fig. S6), not identified in our earlier analysis (*Figure 1*). The newly identified population clustered independently due to high differential expression of genes implicated in cell cycle, DNA synthesis and proliferation (*TOP2A, CENPF, NUSAP1, TUBAB1, MKI67*) (fig. S7 and S8) and demonstrated the highest average expression of G2M and S phase gene sets among all clusters (fig. S9). Accordingly, we designated this population cycling TEC (cyTEC). CyTEC were most predominant in the earliest (embryonic) samples and decreased in frequency with increasing developmental age. mTECII showed a relative increase in frequency over time but remained infrequent compared to mTECI. mTECIII/IV largely appeared after birth (Fig. 4A, left).

Retinoic acid signaling plays an important role in vertebrate morphogenesis, specifically in the patterning of the pharyngeal pouches[61-63]. Moreover, the retinoic acid and IFN signaling axes intersect, with retinoic acid augmenting the effect of IFN[64]. To investigate differences in retinoic acid metabolism in thymic epithelial subsets, we integrated a curated set of developmentally relevant retinoic acid genes[65,66] into expression modules for (I) retinoic acid synthesis, (II) retinoic acid nuclear receptor activity and (III) retinoic acid degradation (Fig. 4B). There were no gross differences in the retinoic acid synthetic capacity across analyzed TEC subsets. Retinoic acid nuclear activity showed lowest expression in AIRE-positive mTECII but peaked in post-AIRE mTECIII/IV. cTEC had a considerably higher expression of the retinoic acid degradation module (Fig. 4C). Retinoic acid degradation in cTEC, mcTEC and mTECI declined substantially

during transition from early to midgestation (Fig. 4D). These data suggest distinct TEC subsets differentially metabolize retinoic acid.

Histone acetyltransferases and histone deacetylases (HDACs) are regulators of chromatin remodeling that can alter IFNα- and IFNγ-inducible transcription[67,68]. Recently, Hdac3 has been described as master regulator of murine mTEC development[69], yet little is known about HDAC specificity in human TECs. Therefore, we examined *HDAC1-8* in our dataset. *HDAC4* showed uniquely high expression in cTEC that peaked midgestation and persisted after birth (Fig. 4E). CyTEC showed highest expression of *HDAC1*; mcTEC showed a similar HDAC profile as cyTEC, albeit confined to a smaller fraction of cells. The most highly expressed HDACs in mTECIII/IV and TECmyo/neuro were *HDAC5* and *HDAC2,* respectively. To corroborate preferential expression of *HDAC4* in cTEC, we performed IHC on human fetal thymus. HDAC4 preferentially colocalized with the cTEC marker PSMB11 (Fig. 4F), supporting our transcriptional findings. Distinct retinoic acid metabolism and HDAC expression profiles in individual TEC subsets raise the possibility that diverse TEC populations process IFN signals differentially.

Patterns of peripheral tissue antigen expression

Central tolerance is induced in the thymus through negative selection of autoreactive T cells[70,71]. Negative selection of T cells recognizing peripheral tissue antigens (PTAs) is enabled by the TF *AIRE*[72]. To investigate signatures of PTA expression and their relationship to *AIRE*, we subclustered the medullary subpopulations mTECII, mTECIII/IV, TECmyo and TECneuro within the *vertical* dataset. mTECII and mTECIII/IV separated distinctly from the TECmyo and

TECneuro populations (Fig. 5A). Further increase in granularity delineated six populations, including immature *AIRE*^{low} mTECII (*CCL19*), cycling mTECII (*TOP2A*), mature *AIRE*^{high} mTECII, post-*AIRE* mTECIII/IV (*SPINK5*), muscle-like TEC (*ACTA1*) and neuroendocrine-like TEC (*BEX1*) (Fig. 5B). Mature *AIRE*^{high} mTECII and post-*AIRE* mTECIII/IV populations significantly increased in frequency throughout the observed developmental interval, while muscle and neuroendocrine-like TEC did not expand notably beyond midgestation (Fig. 5C and D). Maturation and specification of medullary TECs from mTECI to mature *AIRE*^{high} mTECII stages was marked by decreasing *CCL19* and *TP63* expression. *AIRE*^{high} mTECII cells exclusively co-expressed *AIRE* and *FEZF2*. mTECIII/IV were high in *SPINK5* and *IVL* indicating their post-*AIRE* provenance[19,42,73]. Defining signatures in post-*AIRE* TECs included *GRHL1*, *GRHL3* and *KRTDAP*, denoting the keratinocyte-like state of mTECIII, while *POU2F3* indicated the emergence of Tuft-like cells (mTECIV)[19,20,42]. Neuroendocrine-like TEC (*NEUROD1)*, and muscle-like TEC (*MYOG1)* exhibited minimal keratinization and absent *FOXN1* expression but were high in *EPCAM*, supporting their epithelial nature (Fig. 5E). To assess if the transcriptional signatures defining TECmyo and TECneuro represent stable cellular phenotypes or isolated, possibly promiscuous gene expression, we probed for transcription factor-target gene interactions using SCENIC. Muscle and neuroendocrine-like TECs showed full expression of muscle- (*MYOD1, MYOG1, MEF2A, MEF2C, TEAD4, MYF6*) and neuroendocrine-specific (*NEUROD1, NEUROD2, SOX4, SOX11, POU4F1, NPDC1, ZEB1*) regulons, respectively (Fig. 5F), while *AIRE*-positive and post-*AIRE* medullary TECs did not express comprehensive sets of peripheral tissue defining regulons. Mature *AIRE*^{high} mTECII displayed highest MHC class I and II expression (Fig. 5G), in line with their highest type II IFN module score (Fig. 3D), whereas muscle and neuroendocrine-like TECs expressed low levels of

MHC class I and no MHC class II (Fig. 5G). These findings point to divergent patterns of PTA expression in discrete thymic epithelial cell subsets. Absent expression of MHC class II molecules combined with low expression IFN response regulons (Fig. 2D) in TECmyo and TECneuro point to an IFN-independent developmental trajectory.

Distinct IFN response networks direct cortical and medullary lineage specification

To dissect the transcriptional sequences that give rise to cortical and medullary thymic epithelial lineages across the *vertical* dataset, we employed tSpace, an algorithm optimized to elucidate developmental pathways from high-dimensional datasets[74]. The tSpace projection rendered an mcTEC-centric view of the thymus with cTEC and mTECI populations flanking mcTEC on both sides (Fig. 6A and fig. S10). Using Slingshot[75] on the core populations cyTEC, mcTEC, cTEC and mTECI, we inferred two distinct trajectories along pseudotime, denoting cortical (trajectory 1) and medullary lineages (trajectory 2) (Fig. 6B). Notably, the trajectories originated at the cyTEC population but did not branch until midway through the mcTEC cluster.

To explore transcriptional drivers directing the cortico-medullary lineage bifurcation, we investigated dynamic changes in gene expression along lineage trajectories using tradeSeq[76]. Gene expression was modeled along defined points (knots) in pseudotime. To uncover early signals that demarcate the cortico-medullary lineage branchpoint, we identified genes with differential expression across the immediate bifurcation (pseudotime region between knots 2 and 3). The key thymic regulators *PAX1* and *FOXN1*, together with *NFKB1* and *ASCL2,* demonstrated increased expression early along the cortical trajectory, whereas *IRF7*, *IRF9*,

STAT1, the IFN-stimulated antigens *SP100*, *SP110*, and the immunomodulator *BHLHE40*[50] showed an early medullary increase in expression (Fig. 6C and fig. S11).

To obtain a global view of the gene regulatory networks governing the divergent maturation of cTEC and mTECI, we applied SCENIC to populations with the highest canonical cortical (cTEC^{Hi}) and medullary (mTECI^{Hi}) lineage marker expression (fig. S12). Significant interactions between cTEC^{Hi} and mTEC^{Hi} markers and regulon-defining transcription factors were visualized in a network which formed distinct cortical and medullary clusters (Fig. 6D). In the cortical cluster, notable transcription factors with abundant target gene cross talk with cortex-defining markers included the basic helix-loop-helix-leucine zipper (bHLH-Zip) *SREBF1*, along with *FOXN1*, *NFKB1* and *ASCL2*, which shared interactions with *HDAC4*, the retinoic acid-binding and metabolizing proteins *FABP5* and *CYP26B1*, the thymic regulators *PAX1* and *TBATA* and other cTEC-defining markers such as *CXCL12* and *LY75*. Within the medullary cluster, *IRF1*, *IRF7, IRF9, STAT1* and *STAT2* shared abundant targets including the type II IFN response genes *CXCL9* and *CXCL10,* along with *CXCL11, CCL19, CCL21,* and multiple *KRT* genes. Upregulation of ribosomal proteins was unique to mTECI. To gain insights into the maturation of AIRE-positive TECs, we specifically evaluated the differential expression of regulons along the region of pseudotime corresponding to the onset of *AIRE* expression (Fig. 6E and fig. S13). The *AIRE*-targeting regulons *SPIB, SPIC, CREB3L1, IKZF1*, *POU2F3* and *RELB* exhibited a steady gain in expression along the extended medullary trajectory, followed by a brisk increase in *AIRE, TFAP2A* and *MSC* expression that marked the mTECII stage. This was paralleled by a sharp decline in *JUNB, FOSB, EGR1, TP63* and *TP73*. Notably, *SPIB, SPIC, CREB3L1, IKZF1* and *POU2F3* shared *FEZF2* and *AIRE* as target genes, while *FEZF2* emerged as *AIRE's* most

highly co-expressed target gene (Fig. 6F and fig. S14). MHC class I and II expression demonstrated consistent transcriptional gain along the medullary trajectory (Fig. 6G).

Using different computational models at varied points along pseudotime, *FOXN1, ASCL2*, *PAX1* and *NFκB1* consistently emerged as gene regulatory networks preferentially governing cortical lineage development while an activation of the interferon regulatory factor networks was predominantly observed in the medullary lineage. The expression of well-described signature genes defining cortical and medullary TEC validated the analysis.

DISCUSSION

Progress in genomic analysis methods has redefined our concept of thymic epithelial architecture. The goal of this study was to understand the dynamic signals that drive thymic fate and lineage diversification during development. Unlike prior studies which solely focused on the thymus, we sought to gain novel insights by studying thymic development in an unprecedented context. Comparing human fetal epithelial cells from different anterior foregut-derived organs, we provide evidence that type I and II IFNs exert inductive signals on the thymic epithelial stroma. We further show that the pervasive effects of IFNs extend differentially into the thymic epithelial compartment, reflected in characteristic *NFκB* and *IRF* signatures specific to cortical and medullary lineages. Previous studies pointed to an activation of the TNF signaling axis, mediated by CD40 and RANK, during medullary TEC development[77,78]. These signals were shown to stimulate the NFκB pathway and proved essential for various aspects of mTEC fate and function[77,79,80]. Our data highlights a central role for type I and II IFNs during thymic morphogenesis with IRFs, STATs and NFκB emerging as downstream mediators that fine-tune

IFN responses along cortical and medullary lineage trajectories. How exactly the global effects of type I and II IFNs are differentially mediated in cTECs and mTECs, is subject to ongoing investigations. Multiple lines of inquiry exist: Retinoic acid is known to increase the effect of type II IFN[64]. Type II IFN, in turn, has been shown to selectively increase the expression of *IRF1* and *STAT1*[81-83]. Our data indicates that retinoic acid is preferentially degraded in cTECs, which could explain the relatively lower average expression of IFN target genes in the cortex relative to the medulla. A similar rationale applies to HDACs as regulators IFN-inducible transcription[67,68]. Hence, we posit that differential expression patterns in genes altering the IFN response, along with other cytokines and their receptors, orchestrate spatially distinct niches within the thymus that ultimately give rise to diverse TEC subsets. However, this framework does not preclude that subtle differences in patterning underlying the thymic cortex and medulla precede the recruitment of IFN-releasing hematopoietic elements into the thymus and contribute to the higher baseline expression of *FOXN1*, *PAX1* and *ASCL2* in the cortex.

Starting at midgestation, the medullary lineage represents the largest fraction of TECs, highlighting its importance in negative selection. Negative selection must "anticipate" that T cells will encounter PTAs. This was originally believed to occur by cellular mimicry of medullary TECs resembling peripheral tissues[84]. The concept was largely abandoned with the discovery of the transcription factor Auto Immune Regulator (AIRE) in a subset of medullary TECs[72]. AIRE's function is unique in that it triggers PTA expression independent of target-sequence specificity by leveraging chromatin plasticity[85]. FEZF2 has been described as an additional regulator of PTA expression[86], although its mechanistic underpinnings remain less clear[87]. Together, AIRE and FEZF2 are thought to account for approximately 60% of PTA

expression[134], raising the question where the remaining PTA expression originates from. A recent study found that small numbers of mTECs with high PTA expression displayed distinct motif enrichments for lineage-defining transcription factors in a manner that was only partially Aire-dependent[42]. These findings led to the hypothesis that mTECs co-opt lineage defining transcription factors to induce tolerance[88]. We did not identify such motif enrichment in our human data set; however, our study suggests that AIRE-dependent PTA expression is an evolving process that may not yet be fully completed at birth. Of all queried TEC subsets, mature *AIRE*^{high} mTECII showed the strongest IFNγ response signature, while IFN signaling did not seem to play a role in the development of TECmyo and TECneuro. In stark contrast to mature AIRE-positive TECs, TECmyo and TECneuro mimicked native muscle and neuroendocrine tissue signatures but lacked *FOXN1* expression, known post-AIRE markers, antigen presenting molecules and significant keratinization. These findings point to divergent patterns of AIRE-dependent and possibly AIRE-independent PTA expression in discrete thymic epithelial cell subsets.

Recently, a role for IL1b in the development of lung epithelial cells has been described[89]. Our work expands the emerging concept that local immune cell niches are essential for the development of different epithelial organs.

Between the extended maturation of the thymic medulla, i.e. mTECII/III/IV expand further after birth, and the involution of the thymus in the second decade of life, the window of thymic peak performance is short-lived. In addition, genetic defects and a myriad of iatrogenic and biological insults to the thymus can compromise its structural integrity and function. This underscores the

urgent need for therapies to regenerate thymic tissues. Our study dissecting the transcriptional framework underlying commitment and specialization of the human thymic epithelial stroma during development reveals novel regulators of thymic epithelial differentiation and may offer actionable insights to advance the differentiation of thymic epithelial cells *in vitro.*

MATERIALS AND METHODS

Tissue Acquisition

Human fetal tissues from thymus, bronchus, lung and esophagus were obtained under Stanford School of Medicine IRB-approved protocols from the Department of Obstetrics and Gynecology at Stanford Hospital. Samples were derived from deidentified fetal tissue donations with written informed consent after elective termination of pregnancy. The study does not qualify as human subjects research, as defined by the Stanford School of Medicine IRB. Single cell transcriptomic data from pcw 6-7 samples was obtained in collaboration with the laboratory of Prof. Sarah Teichmann, from the MRC/Wellcome Trust-funded Human Developmental Biology Resources (HDBR, http://www.hdbr.org). Developmental age at embryonic stages up to pcw 8 was estimated using the Carnegie staging method (Molecular Genetics of Early Development, ISBN 1859960316). Sample C41 was originally estimated to be pcw 8 by the Carnegie staging method but was corrected to pcw 6 by comparison to other samples in the dataset. In fetal samples, developmental age was estimated from measurements of foot length and heel to knee length, compared against a standard growth chart[90], and matched with the gestational age.

Tissue Digestion

Human fetal thymus and lung samples (pcw 16 -18) were mechanically dissected into <2 mm^3 pieces using surgical scissors. Human fetal bronchus and esophagus samples (pcw 16 -18) were opened longitudinally and mechanically scraped with scalpel to harvest the inner epithelial layer of bronchus and esophagus, respectively. All tissue samples were enzymatically digested with DNAse (10 mg/ml) and Liberase (2.5 mg/ml, Sigma Aldrich) per 10 g tissue using a tissue dissociator (gentleMACS, C tube, program m_spleen_02 (Miltenyi), 1-3 runs depending on tissue). Tissue fragments were transferred to a 50 ml tube and incubate at 37°C for 20 min. Cells were pelleted at 110 g, at RT for 2 min and resuspended in 10 ml PBS. For persisting fragments, the procedure was repeated 1-2 times to yield single cells. Cells were resuspended in MACS buffer (PBS, 1 % BSA, 2 mM EDTA), filtered through a 100 um cell strainer and counted.

Epithelial Cell Enrichment

For fetal thymic tissue (16-18 pcw) only, cell suspension was depleted of thymocytes and other immune cells using Human CD45 MicroBeads (Miltenyi) and LD depletion columns (Miltenyi), 10^8 cells/column, according to the manufacturer's instructions. Single cell suspensions of all tissues, (CD45-depleted thymus, bronchus, lung, and esophagus) were enriched for epithelial cells using Human CD326 (EPCAM) Microbeads and LS positive selection columns (Miltenyi) according to the manufacturer's instructions. Quality control for thymocyte depletion and epithelial cell enrichment for thymic single cell suspensions was performed by flow cytometry on FACSAria II with CD45-APC, CD3-FITC, CD205-PE, EPCAM-APC, and Live Dead-Near InfraRed-APC-Cy7 prior to MACS purification. Due to epitope blockage from magnetic bead antibodies, additional markers, i.e. CD7-AF647 (thymocytes) and CD105-PerCP/Cy5.5 (thymic mesenchymal cells) were used to assess post enrichment purity.

scRNAseq Library Preparation and Sequencing

Gel-Bead in Emulsions (GEMs) were generated from single cell suspensions using the 3′ V3 chemistry and Chromium microfluidics system (10X Genomics). After reverse transcription, barcoded cDNA was extracted from the GEMs by Post-GEM RT-cleanup and amplified for 12 cycles. Amplified cDNA was subjected to 0.6x SPRI beads cleanup (Beckman, B23318). 25% of the amplified cDNA was subjected to enzymatic fragmentation, end-repair, A tailing, adaptor ligation and 10X specific sample indexing as per manufacturer's protocol. Libraries were quantified using Bioanalyzer (Agilent) analysis. Libraries were pooled and sequenced on a NovaSeq 6000 instrument (Illumina) using the recommended sequencing read lengths of 28 bp (Read 1), 8 bp (i7 Index Read), and 91 bp (Read 2).

scRNA-seq data processing

Single cell data were aligned to human genome library. After genome alignment and filtering for mitochondrial content and number of genes/reads per cell, the data was normalized with regularized negative Binomial regression using Seurat V.4.0[91]. Cells from different samples were then combined using integration anchors[92]. The dataset was organized by performing PCA dimensionality reduction on the 3000 most variable genes followed by unsupervised Louvain clustering on the 50 top principal components and visualized using Seurat's UMAP function.

Cumulative (bulk) RNA-seq Preparation and Sequencing

Total RNA was extracted from thymocytes and EPCAM positive-selected epithelial cells from thymus, bronchus and lung samples using the Qiagen RNeasy kit. Libraries were prepared from

Total RNA using the SMART-Seq v4 Ultra low Input RNA kit (Takara Bio) and quantified using Bioanalyzer (Agilent) analysis. Libraries were pooled and sequenced on a NovaSeq 6000 instrument (Illumina) at 20 million paired reads per sample.

Cumulative (bulk) RNA-seq processing and analysis

Bulk RNA-seq FASTQ data were processed through latch.bio, a cloud data platform to provide computing infrastructure and visualization tools for biological data analysis. The resulting count matrix was analyzed using the standard DESeq2/1.36.0 workflow. Normalized gene counts were visualized using ggplot2/3.40.

Differential gene expression

Differential gene expression between single-cell clusters was determined using the FindAllMarkers function within Seurat.

Single Cell Heatmap

The top 60 differentially expressed genes (DEGs) specific to fetal thymic epithelial cells compared to fetal epithelial clusters of all other organs were identified (p<10^-300). Downsampled cluster expression (30 cells per cluster using R's sample function) of DEGs was visualized using Seurat's DoHeatmap function.

Gene set analysis

Gene sets were obtained from the Molecular Signature Database (MSigDB) curated C2 dataset[58]. We then performed gene set enrichment analysis (GSEA) using these sets and differential gene

expression between annotated single-cell clusters as determined in Seurat. GSEA was performed with clusterProfiler/4.5.1.902 using the GSEA function ($p<0.05$). In order to visualize biological themes, we created a network representation of positively enriched gene set expression across single-cell clusters. In these networks, gene sets represent nodes and edges are drawn between nodes based on the proportion of shared genes between them (Jaccard similarity coefficient = 0.2). Each node is then colored proportionally by the relative enrichment of that gene set in each single-cell cluster. Gene set network visualization was performed using enrichplot/1.17.0.992[59].

Module scores

We determined gene module scores by applying the AddModuleScore function within Seurat to gene lists of interest.

Gene regulatory network inference

The single cell regulatory network inference and clustering algorithm, SCENIC, was used to identify transcription factor (TF) regulons as previously described[47, 48]. Prior to pySCENIC/0.12.0 input (Python/3.9.0), log1p normalized expression matrices were filtered to remove low quality genes according to an average expression threshold value across all cells of 0.01.

In brief, sets of genes that are co-expressed with TFs are identified during SCENIC's first step using the GRNBoost2[93] algorithm. Then, each potential TF-target interaction was subjected to *cis*-regulatory motif analysis to detect putative direct-binding targets during the RcisTarget step. Interactions with significant motif enrichment of the respective upstream TF were retained while indirect targets lacking motif support were removed. Lastly, predicted regulons and an

aggregate of their targets from all potential motifs were used to determine cellular enrichment for each regulon during the AUCell step.

SCENIC AUCell Seurat Integration

SCENIC's AUCell output matrix was passed into Seurat/4.3 and normalized across features using Seurat's centered log ratio transformation. The data was subjected to a standard Seurat processing pipeline consisting of FindVariableFeatures(), ScaleData(), followed by RunPCA(). UMAP dimensionality reduction was carried out using the top 15 principal components for fetal anterior foregut epithelial cells. Differential regulons were identified with a log2fc.threshold = 0.01.

SCENIC Network Visualization

The network visualization found in Figure 2C was made using the RcisTarget output of fetal anterior foregut epithelial cells. An adjacency matrix was constructed by drawing an edge if a regulon-defining TF was the target of another regulon-defining TF. To filter the network for the most highly co-expressed interactions, only interactions with a GRNBoost2 importance score >10 were retained (970 interactions out of a total of 7522). The resultant edge list was then passed into igraph/1.3.5 and clustered using igraph's cluster_leiden function (resolution = 1). The network visualization found in Figure 6D was made using the RcisTarget output of cTEC and mTECI cells from all developmental stages with high canonical marker expression (*PRSS16* and *CCL19* log1p normalized expression value > 4). Seurat's FindMarkers function was used to identify DEGs between populations (400 marker genes per population, p<10^-30). An adjacency matrix was constructed by drawing an edge if a regulon defining TF targeted a marker gene.

Highly co-expressed interactions were retained using a GRNBoost2 importance score >5 (1027 interactions out of a total of 5763). Only regulons with a minimum of 5 interactions were visualized. The network visualization found in Figure 5F was made using the RcisTarget output of mTECII, mTECIII/IV, and TEC myo/neuro cells from all developmental stages. Seurat's FindMarkers function was used to identify DEGs between muscle-like and neuroendocrine-like clusters (p<10^-10). If a regulon-defining TF had >= 15 targets that intersected with the top 50 markers of either population, an edge was drawn. Highly co-expressed interactions were retained using a GRNBoost2 importance score >5 (300 interactions out of a total of 417). Network visualization of all networks was done using igraph/1.3.5, ggplot2/3.40, and ggnetwork/0.5.12.

Trajectory and pseudotime analysis

We utilized tSpace/0.1.0 [60] to represent continuous relationships between single-cell expression profiles. In brief, tSpace determines cellular distances based on the shortest path between cellular k-nearest neighbor (KNN) subgraphs using the Wanderlust algorithm. These distances were then reduced using uniform manifold approximation and projection (UMAP). We then fit principal curves through dimensionally reduced tSpace data using slingshot/1.8.0 and SingleCellExperiment/1.12.0. Cycling TEC were selected as the starting-point cluster, while end-point clusters were not specified. We then extracted principal curve coordinates and cellular pseudotime values based on the resulting principal curves.

Modeling gene expression along pseudotime

We utilized tradeSeq/1.4.0[61] to build a negative binomial generalized additive model of single-cell gene expression and SCENIC AUCell values along pseudotime. This allowed for statistical

testing of both within-trajectory and between-trajectory gene expression differences as well as smoothing of gene expression along pseudotime for the purpose of visualization. The earlyDETest function was used to identify the key differential TFs between lineages 1 and 2 across knots 2-3. The 40 TFs with the highest Wald Statistic value ($p<0.05$) were visualized. Tradeseq's startVsEndTest function was used to identify within-lineage differentially expressed regulons along a pseudotime range corresponding to the onset of *AIRE* expression (medullary lineage, pseudotime range 22-28). The pseudotime range corresponding to the onset of *AIRE* expression was determined visually (Figure S14B). Regulons with a $p<0.05$ were visualized.

Trajectory Heatmap Construction

Scaled expression values (Seurat's ScaleData function) and quantile scaled (SCORPIUS/1.0.8 scale_quantile function) SCENIC Regulon AUC values were used to construct expression matrices along Slingshot pseudotime. The rolling average of these matrices (zoo/1.8-11) were then passed into pheatmap/1.0.12 for visualization.

Co-expression Heatmap Construction

Inferred interactions between a regulon-defining TF and its target were identified using SCENIC's RcisTarget output. These interactions were visualized according to co-expression values (GRNBoost2's importance score) using ggplot2/3.40.

Immunohistochemistry and confocal imaging

Paraffin-embedded human fetal thymus tissues were deparaffinized in xylene and rehydrated with ethanol solutions of decreasing concentrations until a final wash step with milliQ water.

Antigen retrieval was performed with IHC-Tek™ Epitope Retrieval Solution (#IW-1100-1L, IHC World) using steam. Tissue slices were permeabilized with permeabilization solution (PBS, 0.2%TritonX-100) for 30 minutes at room temperature, blocked with PBS containing 10% of Donkey Serum (DS) and 1% Bovine Serum Albumin for 1 hour at room temperature, and incubated with primary antibodies (see table 1 for reference) diluted in PBS with 1% DS in a humid chamber for 16 hours at 4˚C. Slides were washed with PBS and incubated with fluorescently-labeled secondary antibody for 1 hour at room temperature. After subsequent washes with PBS, tissue autofluorescence was quenched with Vector TrueVIEW Autofluorescence Quenching Kit (# SP-8400, Vector Labs). Nuclei were stained with 5 µg/ml of DAPI in PBS for 10 minutes at room temperature. Slides were mounted with VectaMount. Tissue visualization and image collection was performed using a Leica Stellaris 5 Confocal microscope and LAS X software (Leica Microsystems). All images were acquired using 40X (HC PL APO CS2, NA 1.30) or 63X (HC PL APO CS2, NA 1.40) oil-immersion objectives.

Table 1. List of Antibodies

Antibody	Dilution	Source	Identifier
Mouse anti-human Histone deacetylase 4 (HDAC4)	1:50	Santa Cruz	sc-46671
Mouse anti-rabbit Pan-Keratin	1:100	Santa Cruz	sc-81714
Rabbit anti-human PSMB11	1:50	Abcam	ab170832
Rabbit anti-human Keratin 5	1:100	Biolegend	905501
Donkey anti-rabbit Alexa Fluor 488	1:500	Abcam	ab150073
Donkey anti-mouse Alexa Fluor 647	1:500	Abcam	ab150107

REFERENCES

1. Miller JF, Osoba D. Current concepts of the immunological function of the thymus. *Physiol Rev*. Jul 1967;47(3):437-520. doi:10.1152/physrev.1967.47.3.437
2. Abramson J, Anderson G. Thymic Epithelial Cells. *Annu Rev Immunol*. Apr 26 2017;35:85-118. doi:10.1146/annurev-immunol-051116-052320
3. Kadouri N, Nevo S, Goldfarb Y, Abramson J. Thymic epithelial cell heterogeneity: TEC by TEC. *Nat Rev Immunol*. Apr 2020;20(4):239-253. doi:10.1038/s41577-019-0238-0
4. Miller JF. The golden anniversary of the thymus. *Nat Rev Immunol*. May 27 2011;11(7):489-95. doi:10.1038/nri2993
5. Palmer S, Albergante L, Blackburn CC, Newman TJ. Thymic involution and rising disease incidence with age. *Proc Natl Acad Sci U S A*. Feb 20 2018;115(8):1883-1888. doi:10.1073/pnas.1714478115
6. Hollander GA, Widmer B, Burakoff SJ. Loss of normal thymic repertoire selection and persistence of autoreactive T cells in graft vs host disease. *J Immunol*. Feb 15 1994;152(4):1609-17.
7. Haynes BF, Markert ML, Sempowski GD, Patel DD, Hale LP. The role of the thymus in immune reconstitution in aging, bone marrow transplantation, and HIV-1 infection. *Annu Rev Immunol*. 2000;18:529-60. doi:10.1146/annurev.immunol.18.1.529
8. Thomas R, Wang W, Su DM. Contributions of Age-Related Thymic Involution to Immunosenescence and Inflammaging. *Immun Ageing*. 2020;17:2. doi:10.1186/s12979-020-0173-8
9. McElhaney JE, Effros RB. Immunosenescence: what does it mean to health outcomes in older adults? *Curr Opin Immunol*. Aug 2009;21(4):418-24. doi:10.1016/j.coi.2009.05.023
10. Zorn AM, Wells JM. Vertebrate endoderm development and organ formation. *Annu Rev Cell Dev Biol*. 2009;25:221-51. doi:10.1146/annurev.cellbio.042308.113344
11. Graham A, Richardson J. Developmental and evolutionary origins of the pharyngeal apparatus. *Evodevo*. Oct 1 2012;3(1):24. doi:10.1186/2041-9139-3-24
12. Kishimoto K, Iwasawa K, Sorel A, et al. Directed differentiation of human pluripotent stem cells into diverse organ-specific mesenchyme of the digestive and respiratory systems. *Nat Protoc*. Aug 17 2022;doi:10.1038/s41596-022-00733-3
13. Green MD, Chen A, Nostro MC, et al. Generation of anterior foregut endoderm from human embryonic and induced pluripotent stem cells. *Nat Biotechnol*. Mar 2011;29(3):267-72. doi:10.1038/nbt.1788
14. Miller AJ, Dye BR, Ferrer-Torres D, et al. Generation of lung organoids from human pluripotent stem cells in vitro. *Nat Protoc*. Feb 2019;14(2):518-540. doi:10.1038/s41596-018-0104-8
15. Trisno SL, Philo KED, McCracken KW, et al. Esophageal Organoids from Human Pluripotent Stem Cells Delineate Sox2 Functions during Esophageal Specification. *Cell Stem Cell*. Oct 4 2018;23(4):501-515 e7. doi:10.1016/j.stem.2018.08.008
16. Zhang Y, Yang Y, Jiang M, et al. 3D Modeling of Esophageal Development using Human PSC-Derived Basal Progenitors Reveals a Critical Role for Notch Signaling. *Cell Stem Cell*. Oct 4 2018;23(4):516-529 e5. doi:10.1016/j.stem.2018.08.009

17. Huang SX, Green MD, de Carvalho AT, et al. The in vitro generation of lung and airway progenitor cells from human pluripotent stem cells. *Nat Protoc*. Mar 2015;10(3):413-25. doi:10.1038/nprot.2015.023
18. Kernfeld EM, Genga RMJ, Neherin K, Magaletta ME, Xu P, Maehr R. A Single-Cell Transcriptomic Atlas of Thymus Organogenesis Resolves Cell Types and Developmental Maturation. *Immunity*. Jun 19 2018;48(6):1258-1270 e6. doi:10.1016/j.immuni.2018.04.015
19. Bornstein C, Nevo S, Giladi A, et al. Single-cell mapping of the thymic stroma identifies IL-25-producing tuft epithelial cells. *Nature*. Jul 2018;559(7715):622-626. doi:10.1038/s41586-018-0346-1
20. Miller CN, Proekt I, von Moltke J, et al. Thymic tuft cells promote an IL-4-enriched medulla and shape thymocyte development. *Nature*. Jul 2018;559(7715):627-631. doi:10.1038/s41586-018-0345-2
21. Park JE, Botting RA, Dominguez Conde C, et al. A cell atlas of human thymic development defines T cell repertoire formation. *Science*. Feb 21 2020;367(6480)doi:10.1126/science.aay3224
22. Bautista JL, Cramer NT, Miller CN, et al. Single-cell transcriptional profiling of human thymic stroma uncovers novel cellular heterogeneity in the thymic medulla. *Nat Commun*. Feb 17 2021;12(1):1096. doi:10.1038/s41467-021-21346-6
23. Zeng Y, Liu C, Gong Y, et al. Single-Cell RNA Sequencing Resolves Spatiotemporal Development of Pre-thymic Lymphoid Progenitors and Thymus Organogenesis in Human Embryos. *Immunity*. Nov 19 2019;51(5):930-948 e6. doi:10.1016/j.immuni.2019.09.008
24. Handel AE, Cheuk S, Dhalla F, et al. Developmental dynamics of the neural crest-mesenchymal axis in creating the thymic microenvironment. *Sci Adv*. May 13 2022;8(19):eabm9844. doi:10.1126/sciadv.abm9844
25. Baran-Gale J, Morgan MD, Maio S, et al. Ageing compromises mouse thymus function and remodels epithelial cell differentiation. *Elife*. Aug 25 2020;9doi:10.7554/eLife.56221
26. Aad G, Abajyan T, Abbott B, et al. Measurement of top quark polarization in top-antitop events from proton-proton collisions at radicals=7 TeV using the ATLAS detector. *Phys Rev Lett*. Dec 6 2013;111(23):232002. doi:10.1103/PhysRevLett.111.232002
27. Ragazzini R, Boeing S, Zanieri L, et al. Defining the identity and the niches of epithelial stem cells with highly pleiotropic multilineage potency in the human thymus. *Dev Cell*. Nov 20 2023;58(22):2428-2446 e9. doi:10.1016/j.devcel.2023.08.017
28. Farley AM, Morris LX, Vroegindeweij E, et al. Dynamics of thymus organogenesis and colonization in early human development. *Development*. May 2013;140(9):2015-26. doi:10.1242/dev.087320
29. Corbeaux T, Hess I, Swann JB, Kanzler B, Haas-Assenbaum A, Boehm T. Thymopoiesis in mice depends on a Foxn1-positive thymic epithelial cell lineage. *Proc Natl Acad Sci U S A*. Sep 21 2010;107(38):16613-8. doi:10.1073/pnas.1004623107
30. Flanagan SP. 'Nude', a new hairless gene with pleiotropic effects in the mouse. *Genet Res*. Dec 1966;8(3):295-309. doi:10.1017/s0016672300010168
31. Nowell CS, Bredenkamp N, Tetelin S, et al. Foxn1 regulates lineage progression in cortical and medullary thymic epithelial cells but is dispensable for medullary sublineage divergence. *PLoS Genet*. Nov 2011;7(11):e1002348. doi:10.1371/journal.pgen.1002348
32. Munoz JJ, Tobajas E, Juara S, Montero S, Zapata AG. FoxN1 mediates thymic cortex-medulla differentiation through modifying a developmental pattern based on epithelial tubulogenesis. *Histochem Cell Biol*. Dec 2019;152(6):397-413. doi:10.1007/s00418-019-01818-z

33. Dooley J, Erickson M, Farr AG. An organized medullary epithelial structure in the normal thymus expresses molecules of respiratory epithelium and resembles the epithelial thymic rudiment of nude mice. *J Immunol*. Oct 1 2005;175(7):4331-7. doi:10.4049/jimmunol.175.7.4331
34. Dooley J, Erickson M, Roelink H, Farr AG. Nude thymic rudiment lacking functional foxn1 resembles respiratory epithelium. *Dev Dyn*. Aug 2005;233(4):1605-12. doi:10.1002/dvdy.20495
35. Cordier AC. Ultrastructure of the cilia of thymic cysts in "nude" mice. *Anat Rec*. Feb 1975;181(2):227-49. doi:10.1002/ar.1091810206
36. Shultz LD, Lyons BL, Burzenski LM, et al. Human lymphoid and myeloid cell development in NOD/LtSz-scid IL2R gamma null mice engrafted with mobilized human hemopoietic stem cells. *J Immunol*. May 15 2005;174(10):6477-89. doi:10.4049/jimmunol.174.10.6477
37. Zeleniak A, Wiegand C, Liu W, et al. De novo construction of T cell compartment in humanized mice engrafted with iPSC-derived thymus organoids. *Nature methods*. Oct 2022;19(10):1306-1319. doi:10.1038/s41592-022-01583-3
38. Miller AJ, Yu Q, Czerwinski M, et al. In Vitro and In Vivo Development of the Human Airway at Single-Cell Resolution. *Dev Cell*. Sep 28 2020;54(6):818. doi:10.1016/j.devcel.2020.09.012
39. Travaglini KJ, Nabhan AN, Penland L, et al. A molecular cell atlas of the human lung from single-cell RNA sequencing. *Nature*. Nov 2020;587(7835):619-625. doi:10.1038/s41586-020-2922-4
40. Busslinger GA, Weusten BLA, Bogte A, Begthel H, Brosens LAA, Clevers H. Human gastrointestinal epithelia of the esophagus, stomach, and duodenum resolved at single-cell resolution. *Cell Rep*. Mar 9 2021;34(10):108819. doi:10.1016/j.celrep.2021.108819
41. Metzger TC, Khan IS, Gardner JM, et al. Lineage tracing and cell ablation identify a post-Aire-expressing thymic epithelial cell population. *Cell Rep*. Oct 17 2013;5(1):166-79. doi:10.1016/j.celrep.2013.08.038
42. Michelson DA, Hase K, Kaisho T, Benoist C, Mathis D. Thymic epithelial cells co-opt lineage-defining transcription factors to eliminate autoreactive T cells. *Cell*. Jul 7 2022;185(14):2542-2558 e18. doi:10.1016/j.cell.2022.05.018
43. Pestka S, Krause CD, Walter MR. Interferons, interferon-like cytokines, and their receptors. *Immunol Rev*. Dec 2004;202:8-32. doi:10.1111/j.0105-2896.2004.00204.x
44. Der SD, Zhou A, Williams BR, Silverman RH. Identification of genes differentially regulated by interferon alpha, beta, or gamma using oligonucleotide arrays. *Proc Natl Acad Sci U S A*. Dec 22 1998;95(26):15623-8. doi:10.1073/pnas.95.26.15623
45. Darnell JE, Jr., Kerr IM, Stark GR. Jak-STAT pathways and transcriptional activation in response to IFNs and other extracellular signaling proteins. *Science*. Jun 3 1994;264(5164):1415-21. doi:10.1126/science.8197455
46. Pfeffer LM. The role of nuclear factor kappaB in the interferon response. *J Interferon Cytokine Res*. Jul 2011;31(7):553-9. doi:10.1089/jir.2011.0028
47. Aibar S, Gonzalez-Blas CB, Moerman T, et al. SCENIC: single-cell regulatory network inference and clustering. *Nature methods*. Nov 2017;14(11):1083-1086. doi:10.1038/nmeth.4463
48. Van de Sande B, Flerin C, Davie K, et al. A scalable SCENIC workflow for single-cell gene regulatory network analysis. *Nat Protoc*. Jul 2020;15(7):2247-2276. doi:10.1038/s41596-020-0336-2

49. Matsumoto H, Scicluna BP, Jim KK, et al. HIVEP1 Is a Negative Regulator of NF-kappaB That Inhibits Systemic Inflammation in Sepsis. *Frontiers in immunology*. 2021;12:744358. doi:10.3389/fimmu.2021.744358
50. Cook ME, Jarjour NN, Lin CC, Edelson BT. Transcription Factor Bhlhe40 in Immunity and Autoimmunity. *Trends Immunol*. Nov 2020;41(11):1023-1036. doi:10.1016/j.it.2020.09.002
51. Seo H, Gonzalez-Avalos E, Zhang W, et al. BATF and IRF4 cooperate to counter exhaustion in tumor-infiltrating CAR T cells. *Nat Immunol*. Aug 2021;22(8):983-995. doi:10.1038/s41590-021-00964-8
52. Candi E, Rufini A, Terrinoni A, et al. DeltaNp63 regulates thymic development through enhanced expression of FgfR2 and Jag2. *Proc Natl Acad Sci U S A*. Jul 17 2007;104(29):11999-2004. doi:10.1073/pnas.0703458104
53. Silva FN, Albeshri A, Thayananthan V, Alhalabi W, Fortunato S. Robustness modularity in complex networks. *Phys Rev E*. May 2022;105(5-1):054308. doi:10.1103/PhysRevE.105.054308
54. Tandon A, Albeshri A, Thayananthan V, Alhalabi W, Radicchi F, Fortunato S. Community detection in networks using graph embeddings. *Phys Rev E*. Feb 2021;103(2-1):022316. doi:10.1103/PhysRevE.103.022316
55. Traag VA, Waltman L, van Eck NJ. From Louvain to Leiden: guaranteeing well-connected communities. *Sci Rep*. Mar 26 2019;9(1):5233. doi:10.1038/s41598-019-41695-z
56. Lottini G, Baggiani M, Chesi G, et al. Zika virus induces FOXG1 nuclear displacement and downregulation in human neural progenitors. *Stem Cell Reports*. Jul 12 2022;17(7):1683-1698. doi:10.1016/j.stemcr.2022.05.008
57. Steimle V, Siegrist CA, Mottet A, Lisowska-Grospierre B, Mach B. Regulation of MHC class II expression by interferon-gamma mediated by the transactivator gene CIITA. *Science*. Jul 1 1994;265(5168):106-9. doi:10.1126/science.8016643
58. Platanias LC. Mechanisms of type-I- and type-II-interferon-mediated signalling. *Nat Rev Immunol*. May 2005;5(5):375-86. doi:10.1038/nri1604
59. Theofilopoulos AN, Baccala R, Beutler B, Kono DH. Type I interferons (alpha/beta) in immunity and autoimmunity. *Annu Rev Immunol*. 2005;23:307-36. doi:10.1146/annurev.immunol.23.021704.115843
60. Boehm U, Klamp T, Groot M, Howard JC. Cellular responses to interferon-gamma. *Annu Rev Immunol*. 1997;15:749-95. doi:10.1146/annurev.immunol.15.1.749
61. Cunningham TJ, Duester G. Mechanisms of retinoic acid signalling and its roles in organ and limb development. *Nat Rev Mol Cell Biol*. Feb 2015;16(2):110-23. doi:10.1038/nrm3932
62. Duester G. Retinoic acid synthesis and signaling during early organogenesis. *Cell*. Sep 19 2008;134(6):921-31. doi:10.1016/j.cell.2008.09.002
63. Kopinke D, Sasine J, Swift J, Stephens WZ, Piotrowski T. Retinoic acid is required for endodermal pouch morphogenesis and not for pharyngeal endoderm specification. *Dev Dyn*. Oct 2006;235(10):2695-709. doi:10.1002/dvdy.20905
64. Chelbi-Alix MK, Pelicano L. Retinoic acid and interferon signaling cross talk in normal and RA-resistant APL cells. *Leukemia*. Aug 1999;13(8):1167-74. doi:10.1038/sj.leu.2401469
65. Rhinn M, Dolle P. Retinoic acid signalling during development. *Development*. Mar 2012;139(5):843-58. doi:10.1242/dev.065938
66. Kam RK, Deng Y, Chen Y, Zhao H. Retinoic acid synthesis and functions in early embryonic development. *Cell Biosci*. Mar 22 2012;2(1):11. doi:10.1186/2045-3701-2-11

67. DaFonseca CJ, Shu F, Zhang JJ. Identification of two residues in MCM5 critical for the assembly of MCM complexes and Stat1-mediated transcription activation in response to IFN-gamma. *Proc Natl Acad Sci U S A*. Mar 13 2001;98(6):3034-9. doi:10.1073/pnas.061487598
68. Zhang JJ, Zhao Y, Chait BT, et al. Ser727-dependent recruitment of MCM5 by Stat1alpha in IFN-gamma-induced transcriptional activation. *EMBO J*. Dec 1 1998;17(23):6963-71. doi:10.1093/emboj/17.23.6963
69. Goldfarb Y, Kadouri N, Levi B, et al. HDAC3 Is a Master Regulator of mTEC Development. *Cell Rep*. Apr 19 2016;15(3):651-665. doi:10.1016/j.celrep.2016.03.048
70. Stritesky GL, Xing Y, Erickson JR, et al. Murine thymic selection quantified using a unique method to capture deleted T cells. *Proc Natl Acad Sci U S A*. Mar 19 2013;110(12):4679-84. doi:10.1073/pnas.1217532110
71. Klein L, Kyewski B, Allen PM, Hogquist KA. Positive and negative selection of the T cell repertoire: what thymocytes see (and don't see). *Nat Rev Immunol*. Jun 2014;14(6):377-91. doi:10.1038/nri3667
72. Anderson MS, Venanzi ES, Klein L, et al. Projection of an immunological self shadow within the thymus by the aire protein. *Science*. Nov 15 2002;298(5597):1395-401. doi:10.1126/science.1075958
73. Dhalla F, Baran-Gale J, Maio S, Chappell L, Hollander GA, Ponting CP. Biologically indeterminate yet ordered promiscuous gene expression in single medullary thymic epithelial cells. *EMBO J*. Jan 2 2020;39(1):e101828. doi:10.15252/embj.2019101828
74. Dermadi D, Bscheider M, Bjegovic K, et al. Exploration of Cell Development Pathways through High-Dimensional Single Cell Analysis in Trajectory Space. *iScience*. Feb 21 2020;23(2):100842. doi:10.1016/j.isci.2020.100842
75. Street K, Risso D, Fletcher RB, et al. Slingshot: cell lineage and pseudotime inference for single-cell transcriptomics. *BMC Genomics*. Jun 19 2018;19(1):477. doi:10.1186/s12864-018-4772-0
76. Van den Berge K, Roux de Bezieux H, Street K, et al. Trajectory-based differential expression analysis for single-cell sequencing data. *Nat Commun*. Mar 5 2020;11(1):1201. doi:10.1038/s41467-020-14766-3
77. Akiyama T, Shimo Y, Yanai H, et al. The tumor necrosis factor family receptors RANK and CD40 cooperatively establish the thymic medullary microenvironment and self-tolerance. *Immunity*. Sep 19 2008;29(3):423-37. doi:10.1016/j.immuni.2008.06.015
78. Boehm T, Scheu S, Pfeffer K, Bleul CC. Thymic medullary epithelial cell differentiation, thymocyte emigration, and the control of autoimmunity require lympho-epithelial cross talk via LTbetaR. *J Exp Med*. Sep 1 2003;198(5):757-69. doi:10.1084/jem.20030794
79. Burkly L, Hession C, Ogata L, et al. Expression of relB is required for the development of thymic medulla and dendritic cells. *Nature*. Feb 9 1995;373(6514):531-6. doi:10.1038/373531a0
80. Kinoshita D, Hirota F, Kaisho T, et al. Essential role of IkappaB kinase alpha in thymic organogenesis required for the establishment of self-tolerance. *J Immunol*. Apr 1 2006;176(7):3995-4002. doi:10.4049/jimmunol.176.7.3995
81. Pelicano L, Li F, Schindler C, Chelbi-Alix MK. Retinoic acid enhances the expression of interferon-induced proteins: evidence for multiple mechanisms of action. *Oncogene*. Nov 6 1997;15(19):2349-59. doi:10.1038/sj.onc.1201410
82. Matikainen S, Ronni T, Hurme M, Pine R, Julkunen I. Retinoic acid activates interferon regulatory factor-1 gene expression in myeloid cells. *Blood*. Jul 1 1996;88(1):114-23.

83. Kolla V, Lindner DJ, Xiao W, Borden EC, Kalvakolanu DV. Modulation of interferon (IFN)-inducible gene expression by retinoic acid. Up-regulation of STAT1 protein in IFN-unresponsive cells. *J Biol Chem*. May 3 1996;271(18):10508-14. doi:10.1074/jbc.271.18.10508
84. Farr AG, Rudensky A. Medullary thymic epithelium: a mosaic of epithelial "self"? *J Exp Med*. Jul 6 1998;188(1):1-4. doi:10.1084/jem.188.1.1
85. Kaiser C, Bradu A, Gamble N, Caldwell JA, Koh AS. AIRE in context: Leveraging chromatin plasticity to trigger ectopic gene expression. *Immunol Rev*. Jan 2022;305(1):59-76. doi:10.1111/imr.13026
86. Takaba H, Morishita Y, Tomofuji Y, et al. Fezf2 Orchestrates a Thymic Program of Self-Antigen Expression for Immune Tolerance. *Cell*. Nov 5 2015;163(4):975-87. doi:10.1016/j.cell.2015.10.013
87. Qi Y, Zhang R, Lu Y, Zou X, Yang W. Aire and Fezf2, two regulators in medullary thymic epithelial cells, control autoimmune diseases by regulating TSAs: Partner or complementer? *Frontiers in immunology*. 2022;13:948259. doi:10.3389/fimmu.2022.948259
88. Rode I, Rodewald HR. Transcription factor hijacking in the name of tolerance. *Cell*. Jul 7 2022;185(14):2398-2400. doi:10.1016/j.cell.2022.06.026
89. Barnes JL, Yoshida M, He P, et al. Early human lung immune cell development and its role in epithelial cell fate. *Sci Immunol*. Dec 15 2023;8(90):eadf9988. doi:10.1126/sciimmunol.adf9988
90. Hern WM. Correlation of fetal age and measurements between 10 and 26 weeks of gestation. *Obstet Gynecol*. Jan 1984;63(1):26-32.
91. Hafemeister C, Satija R. Normalization and variance stabilization of single-cell RNA-seq data using regularized negative binomial regression. *Genome Biol*. Dec 23 2019;20(1):296. doi:10.1186/s13059-019-1874-1
92. Stuart T, Butler A, Hoffman P, et al. Comprehensive Integration of Single-Cell Data. *Cell*. Jun 13 2019;177(7):1888-1902 e21. doi:10.1016/j.cell.2019.05.031
93. Moerman T, Aibar Santos S, Bravo Gonzalez-Blas C, et al. GRNBoost2 and Arboreto: efficient and scalable inference of gene regulatory networks. *Bioinformatics*. Jun 1 2019;35(12):2159-2161. doi:10.1093/bioinformatics/bty916

ACKNOWLEDGEMENTS

We thank all members of Stanford 22q11 Deletion Syndrome Program, its directors and advisory board members (Maria Grazia Roncarolo, Irving Weissman, Gay Crooks, Antonio Baldini, Matthew Proteus) and all consortium participants (Kenneth I. Weinberg, Elizabeth Illingworth, Rosa Bacchetta, Andrea Cipriani, Hui Gai) for insightful input and discussions. We thank Hui Gai and MedGenome, Inc. for scRNA library preparation and sequencing, respectively. We thank Riley Suhar and Priscila F. Slepicka for graphical illustrations.

FUNDING

California Institute of Regenerative Medicine, DISC-2 11109

Emerson Collective 1263707

Baxter Foundation

Specifically, we thank the anonymous donors of the Stanford 22q11 Deletions Syndrome Program for their generous support of our work.

AUTHOR CONTRIBUTIONS

A.M., A.G., and K.G.W. interpreted the data and wrote the manuscript. The experiments were designed, performed and analyzed by A.M., B.S., A.G., and K.G.W.. P.F.S, K.M.H., H.D.N., W.W., M.A., D.K.K., M.C. and C.Y.Y. performed additional experiments and bioinformatic data processing. V.W., S.T., J.P. and V.K. provided samples and analytical input. G.A.H., C. G., V.S., and P.K. reviewed design, bioinformatic analysis and edited the manuscript.

COMPETING INTERESTS

None

DATA AVAILABILITY

Single cell RNA-seq data was deposited in GEO with accession number GSE212244. Bulk RNA-seq data was deposited in GEO with accession number GSE241479. All code is available at the following Github repository: https://github.com/abdulvasey/Thymic-Development-Figures.

All other data needed to support the conclusions of the paper are present in the paper or the Supplementary Materials.

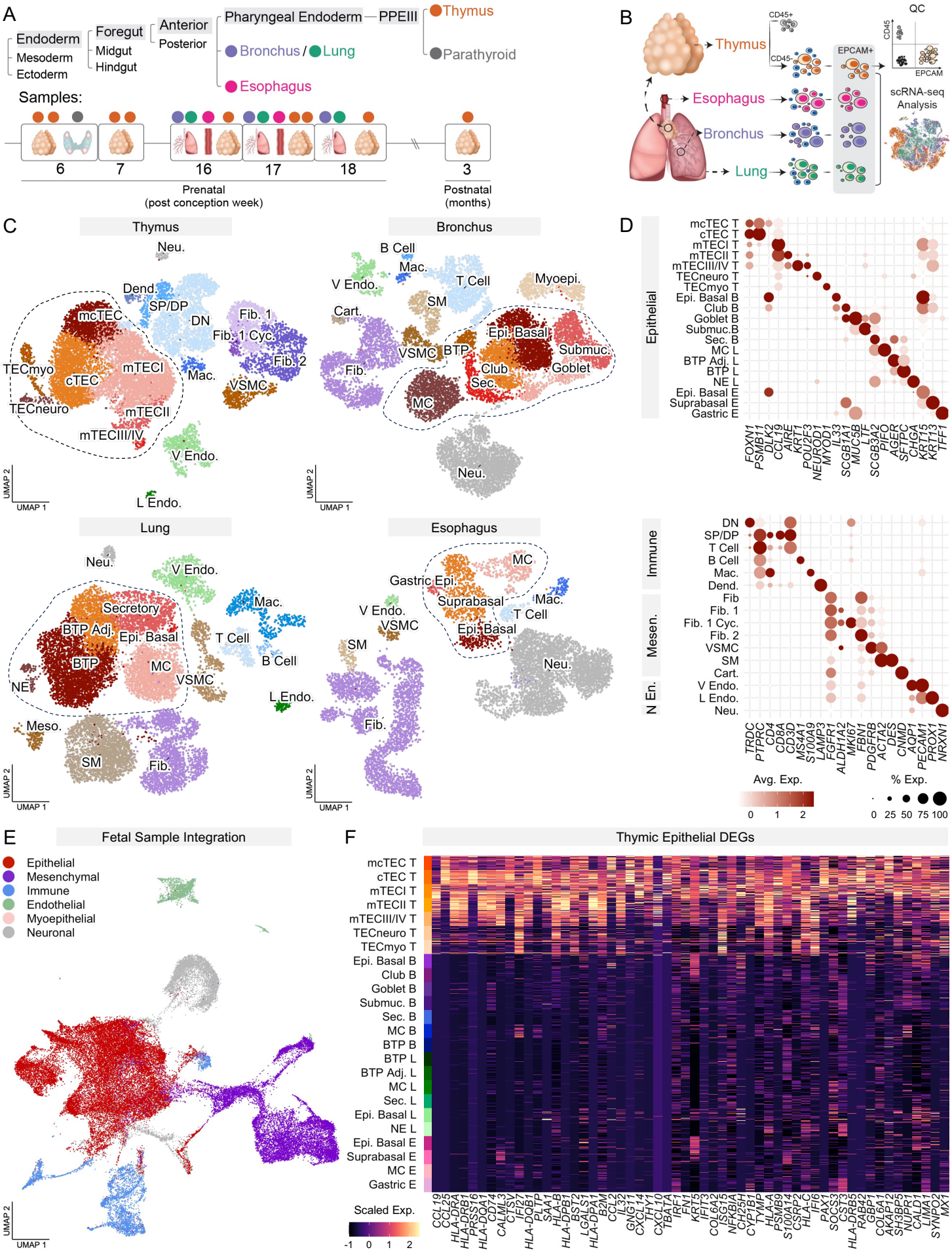
A
Endoderm
Mesoderm
Ectoderm
Foregut
Midgut
Hindgut
Anterior
Posterior
Pharyngeal Endoderm — PPEIII
Thymus
Parathyroid
Bronchus / Lung
Esophagus
Samples:
6
7
16
17
18
3
Prenatal
(post conception week)
Postnatal
(months)
B
Thymus
Esophagus
Bronchus
Lung
CD45+
CD45-
EPCAM+
QC
CD45
EPCAM
scRNA-seq
Analysis
C
Thymus
Neu.
Dend.
SP/DP
mcTEC
DN
Fib. 1
Fib. 1 Cyc.
Fib. 2
TECmyo
cTEC
mTECI
Mac.
VSMC
TECneuro
mTECII
mTECIII/IV
V Endo.
L Endo.
UMAP 2
UMAP 1
Bronchus
B Cell
Mac.
V Endo.
T Cell
Myoepi.
SM
Cart.
Epi. Basal
Submuc.
VSMC
BTP
Fib.
Club
Goblet
Sec.
MC
Neu.
Lung
Neu.
V Endo.
Mac.
Secretory
BTP Adj.
Epi. Basal
T Cell
BTP
MC
B Cell
NE
VSMC
L Endo.
Meso.
SM
Fib.
Esophagus
MC
Gastric Epi.
Suprabasal
Mac.
V Endo.
T Cell
VSMC
Epi. Basal
SM
Neu.
Fib.
D
Epithelial
mcTEC T
cTEC T
mTECI T
mTECII T
mTECIII/IV T
TECneuro T
TECmyo T
Epi. Basal B
Club B
Goblet B
Submuc.B
Sec. B
MC L
BTP Adj. L
BTP L
NE L
Epi. Basal E
Suprabasal E
Gastric E
FOXN1
PSMB11
DLK2
CCL19
AIRE
KRT1
POU2F3
NEUROD1
MYOD1
IL33
SCGB1A1
MUC5B
LTF
SCGB3A2
PIFO
AGER
SFTPC
CHGA
KRT15
KRT13
TFF1
Immune
DN
SP/DP
T Cell
B Cell
Mac.
Dend.
Mesen.
Fib
Fib. 1
Fib. 1 Cyc.
Fib. 2
VSMC
SM
Cart.
N En.
V Endo.
L Endo.
Neu.
TRDC
PTPRC
CD4
CD8A
CD3D
MS4A1
S100A9
LAMP3
FGFR1
ALDH1A2
MKI67
FBN1
PDGFRB
ACTA2
DES
CNMD
AQP1
PECAM1
PROX1
NRXN1
Avg. Exp.
0
1
2
% Exp.
0
25
50
75
100
E
Fetal Sample Integration
Epithelial
Mesenchymal
Immune
Endothelial
Myoepithelial
Neuronal
UMAP 2
UMAP 1
F
Thymic Epithelial DEGs
mcTEC T
cTEC T
mTECI T
mTECII T
mTECIII/IV T
TECneuro T
TECmyo T
Epi. Basal B
Club B
Goblet B
Submuc. B
Sec. B
MC B
BTP B
BTP L
BTP Adj. L
MC L
Sec. L
Epi. Basal L
NE L
Epi. Basal E
Suprabasal E
MC E
Gastric E
Scaled Exp.
-1
0
1
2
CCL19
CCL25
HLA-DRA
HLA-DRB1
PSS16
HLA-DQA1
CD74
CALML3
CTSV
HLA-DQB1
FLTP
SAA1
HLA-B
HLA-DPB1
SST2
LGALS1
HLA-DPA1
B2M
CCL2
IL32
GNG11
CXCL14
THY1
CXCL10
TBATA
IRF1
FN1
KRT5
IFIT3
COL6A2
ISG15
NFKBIA
CH25H
CYP1B1
TYMP
HLA-A
PSMB9
S100A14
CSRP2
HLA-C
IFI6
PAX1
SOCS3
CST3
HLA-DRB5
RAB42
GBP1
COL6A1
AKAP12
SH3BP5
NUPR1
CALD1
LIMA1
SYNPO2
MX1

Figure 1. Cellular composition of human fetal anterior foregut-derived tissues.

(A) Ontogeny of anterior foregut-derived organs. Thymus, bronchus, lung, esophagus and parathyroid arise from the endodermal germ layer (PPEIII, third pharyngeal pouch endoderm) (top). Summary of samples including developmental age and tissue of origin. Colors denote tissue type (thymus, orange; bronchus, blue; lung, green; esophagus, pink; parathyroid, grey) (bottom). (B) Workflow of cell processing and quality control prior to transcriptional profiling. (C) UMAP visualization of human anterior foregut-derived tissues colored by cell type (DN, double negative thymocytes; SP/DP, double positive/single positive thymocytes; Mac, macrophages; Dend, dendritic cells; Fib, fibroblasts; Cyc, cycling; VSMC, vascular smooth muscle cells; SM, smooth muscle cells; Cart, cartilage; V Endo, vascular endothelial cells; L Endo cells, lymphatic endothelial cells; Neu, neuronal cells; Epi, epithelial cells; Submuc, submucosal cells; Sec, secretory cells; MC, multiciliated; BTP, bud tip progenitor cells; adj, adjacent; NE, neuroendocrine cells). Dotted line denotes epithelial clusters. (D) Dot plot of select, cell type-defining genes in individual anterior foregut-derived tissues. Here and onwards, color represents average expression of marker genes in each cell type. Dot size represents percentage of cells in each cell type expressing the selected marker gene (T, thymus; B, bronchus; L, lung; E, esophagus; Mesen, mesenchymal; En, endothelial; N, neuronal). (E) UMAP visualization of integrated anterior foregut-derived tissues at the fetal stage of development (horizontal integration), colored by organ of origin. (F) Heat map of the top thymic epithelial differentially expressed genes (DEGs) across all epithelial clusters from (C) downsampled to 30 cells per cluster.

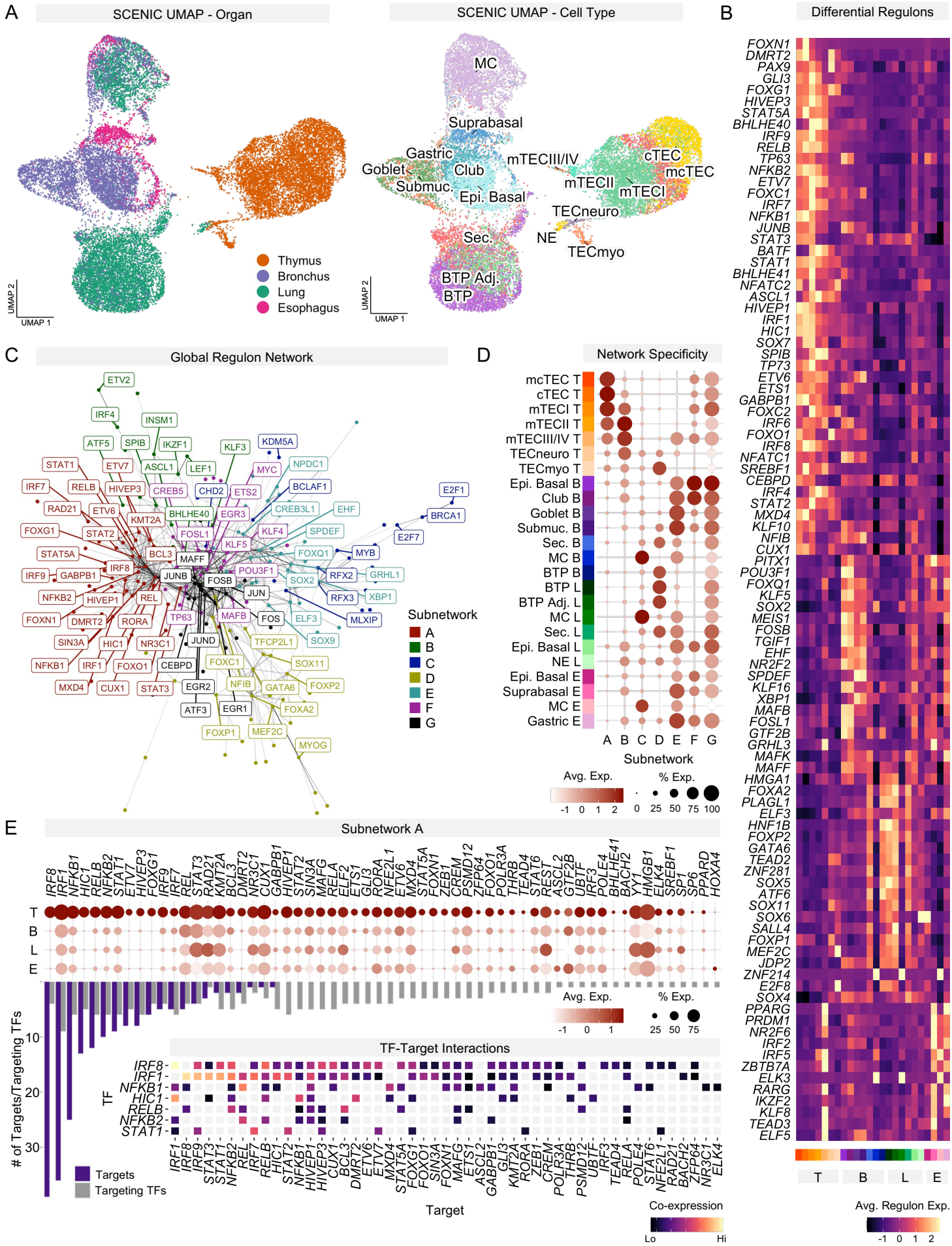
A
SCENIC UMAP - Organ
Thymus
Bronchus
Lung
Esophagus
UMAP 1
UMAP 2
SCENIC UMAP - Cell Type
MC
Suprabasal
Gastric
Goblet
Club
Submuc.
Epi. Basal
mTECIII/IV
cTEC
mcTEC
mTECII
mTECI
TECneuro
NE
TECmyo
Sec.
BTP Adj.
BTP
B
Differential Regulons
T
B
L
E
Avg. Regulon Exp.
C
Global Regulon Network
Subnetwork
A
B
C
D
E
F
G
D
Network Specificity
mcTEC T
cTEC T
mTECI T
mTECII T
mTECIII/IV T
TECneuro T
TECmyo T
Epi. Basal B
Club B
Goblet B
Submuc. B
Sec. B
MC B
BTP B
BTP L
BTP Adj. L
MC L
Sec. L
Epi. Basal L
NE L
Epi. Basal E
Suprabasal E
MC E
Gastric E
Subnetwork
Avg. Exp.
% Exp.
E
Subnetwork A
# of Targets/Targeting TFs
Targets
Targeting TFs
TF-Target Interactions
TF
Target
Co-expression
Lo
Hi

Figure 2. Differential gene regulatory analysis across anterior foregut-derived epithelial cells.

(A) UMAP visualization of SCENIC transcription factor regulons in all fetal epithelial cells colored by tissue of origin (left) and cell type (right). **(B)** Heatmap of differentially expressed transcription factor regulons across anterior foregut-derived tissues (T, thymus; B, bronchus; L, lung; E, esophagus). Color key corresponds to annotated clusters from (D). **(C)** Visualization of transcription factor regulon subnetworks from (A) defined by Leiden algorithm. **(D)** Dot plot representing the average expression of individual transcription factor subnetworks in select epithelial cell subpopulations. **(E)** Dot plot of all subnetwork A genes across anterior foregut-derived tissues. Bar plot corresponds to number of target genes an individual transcription factor has (blue), and the number of regulons that target the respective transcription factor (gray) (top). Heatmap of top inferred interactions found in subnetwork A (TF, transcription factor) (bottom).

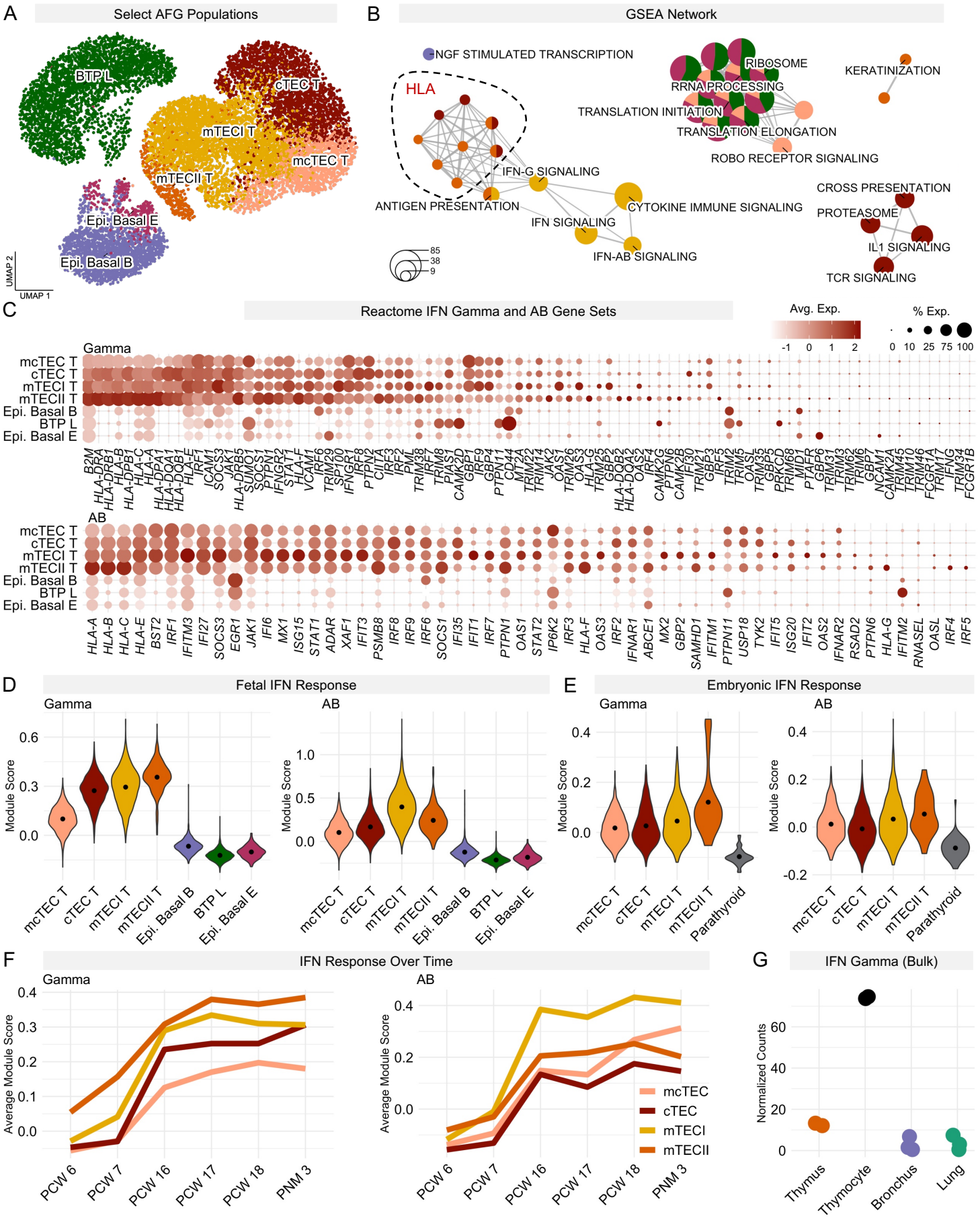
A
Select AFG Populations
BTP L
cTEC T
mTECI T
mcTEC T
mTECII T
Epi. Basal E
Epi. Basal B
UMAP 2
UMAP 1
B
GSEA Network
NGF STIMULATED TRANSCRIPTION
HLA
RIBOSOME
RRNA PROCESSING
TRANSLATION INITIATION
TRANSLATION ELONGATION
ROBO RECEPTOR SIGNALING
KERATINIZATION
IFN-G SIGNALING
ANTIGEN PRESENTATION
CYTOKINE IMMUNE SIGNALING
IFN SIGNALING
IFN-AB SIGNALING
CROSS PRESENTATION
PROTEASOME
IL1 SIGNALING
TCR SIGNALING
85
38
9
C
Reactome IFN Gamma and AB Gene Sets
Avg. Exp.
% Exp.
Gamma
AB
mcTEC T
cTEC T
mTECI T
mTECII T
Epi. Basal B
BTP L
Epi. Basal E
D
Fetal IFN Response
Module Score
E
Embryonic IFN Response
Parathyroid
F
IFN Response Over Time
Average Module Score
PCW 6
PCW 7
PCW 16
PCW 17
PCW 18
PNM 3
mcTEC
cTEC
mTECI
mTECII
G
IFN Gamma (Bulk)
Normalized Counts
Thymus
Thymocyte
Bronchus
Lung

Figure 3. IFN response signatures in select epithelial cell subpopulations throughout development.

(A) UMAP visualization of select epithelial cell subpopulations for thymus, bronchus, lung and esophagus at fetal stages of development. AFG, anterior foregut-derived epithelial cell. **(B)** Network visualization of differentially expressed GSEA gene sets across cell types from (A), colored accordingly. Each node represents a specific GSEA gene set ($p<0.05$). Edges between nodes denote a significant number of shared genes between nodes. Node size reflects the number of genes within each gene set. Gene set names have been abbreviated. Gene sets enriched primarily of *HLA* genes are within the dotted circle. **(C)** Dot plot of all detected Reactome-curated type I and II IFN response genes across populations from (A). **(D)** Violin plots depicting the average expression of Reactome-curated type I and II IFN response gene sets (modules) across populations from (A). Here and onwards, the dot within the violin plot indicates mean expression values. **(E)** Violin plot depicting the average expression of Reactome-curated type I and II IFN response modules in thymic and parathyroid epithelial cells at embryonic stages of development. **(F)** Average expression of Reactome-curated type I and II IFN response modules across embryonic, fetal and postnatal time points in select TEC subpopulations. **(G)** Cumulative (bulk) RNAseq expression of *IFNG* in thymocytes and EPCAM positive-selected epithelial cells from thymus, bronchus and lung.

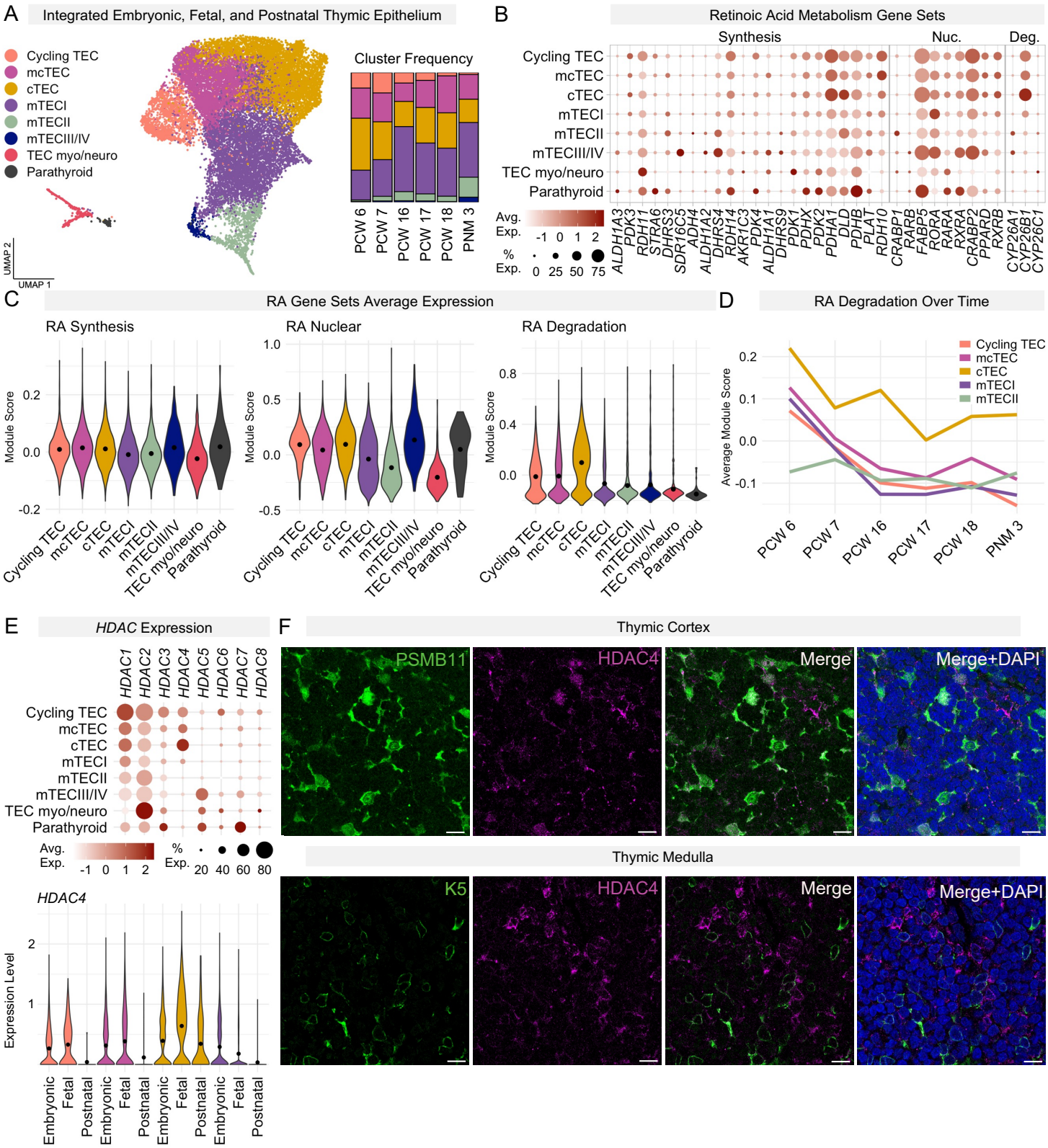
A
Integrated Embryonic, Fetal, and Postnatal Thymic Epithelium
Cycling TEC
mcTEC
cTEC
mTECI
mTECII
mTECIII/IV
TEC myo/neuro
Parathyroid
UMAP 2
UMAP 1
Cluster Frequency
PCW 6
PCW 7
PCW 16
PCW 17
PCW 18
PNM 3
B
Retinoic Acid Metabolism Gene Sets
Synthesis
Nuc.
Deg.
Avg. Exp.
% Exp.
ALDH1A3 PDK3 RDH11 STRA6 DHRS3 SDR16C5 ADH4 ALDH1A2 DHRS4 RDH14 AKR1C3 PDK4 ALDH1A1 DHRS9 PDK1 PDHX PDK2 PDHA1 DLD PDHB PLAT RDH10 CRABP1 RARB FABP5 RORA RARA RXRA CRABP2 PPARD RXRB CYP26A1 CYP26B1 CYP26C1
C
RA Gene Sets Average Expression
RA Synthesis
RA Nuclear
RA Degradation
Module Score
D
RA Degradation Over Time
Average Module Score
E
HDAC Expression
HDAC1 HDAC2 HDAC3 HDAC4 HDAC5 HDAC6 HDAC7 HDAC8
HDAC4
Expression Level
Embryonic
Fetal
Postnatal
F
Thymic Cortex
PSMB11
HDAC4
Merge
Merge+DAPI
Thymic Medulla
K5

Figure 4. Cellular composition of the human thymus during development

(A) UMAP visualization of integrated TECs across all sampled time points, colored by developmental/postnatal age (left). Relative frequency of cells from select TEC subsets across advancing developmental ages (right). **(B)** Dot plot of gene sets defining retinoic acid synthesis, nuclear signaling, and degradation across select TEC subsets (Nuc, nuclear; Deg, degradation). **(C)** Violin plot representing the average expression of retinoic acid metabolism gene sets from (B) across visualized cell types from (A). RA, retinoic acid. **(D)** Average expression of retinoic acid metabolism gene sets across embryonic, fetal, and postnatal time points for select TEC subsets. **(E)** Dot plot of *HDAC 1-8* gene expression across thymic and parathyroid epithelial cell subpopulations (top). Violin plot of *HDAC4* gene expression in select TEC subsets across advancing developmental ages. Embryonic: pcw 6-7, Fetal: pcw 16-18, Postnatal: 3 months post birth (bottom). **(F)** Representative immunohistochemistry images of human fetal thymus sections stained for PSMB11 (green) and HDAC4 (magenta) protein. Counterstain with DAPI (blue). Scale bars: 50um.

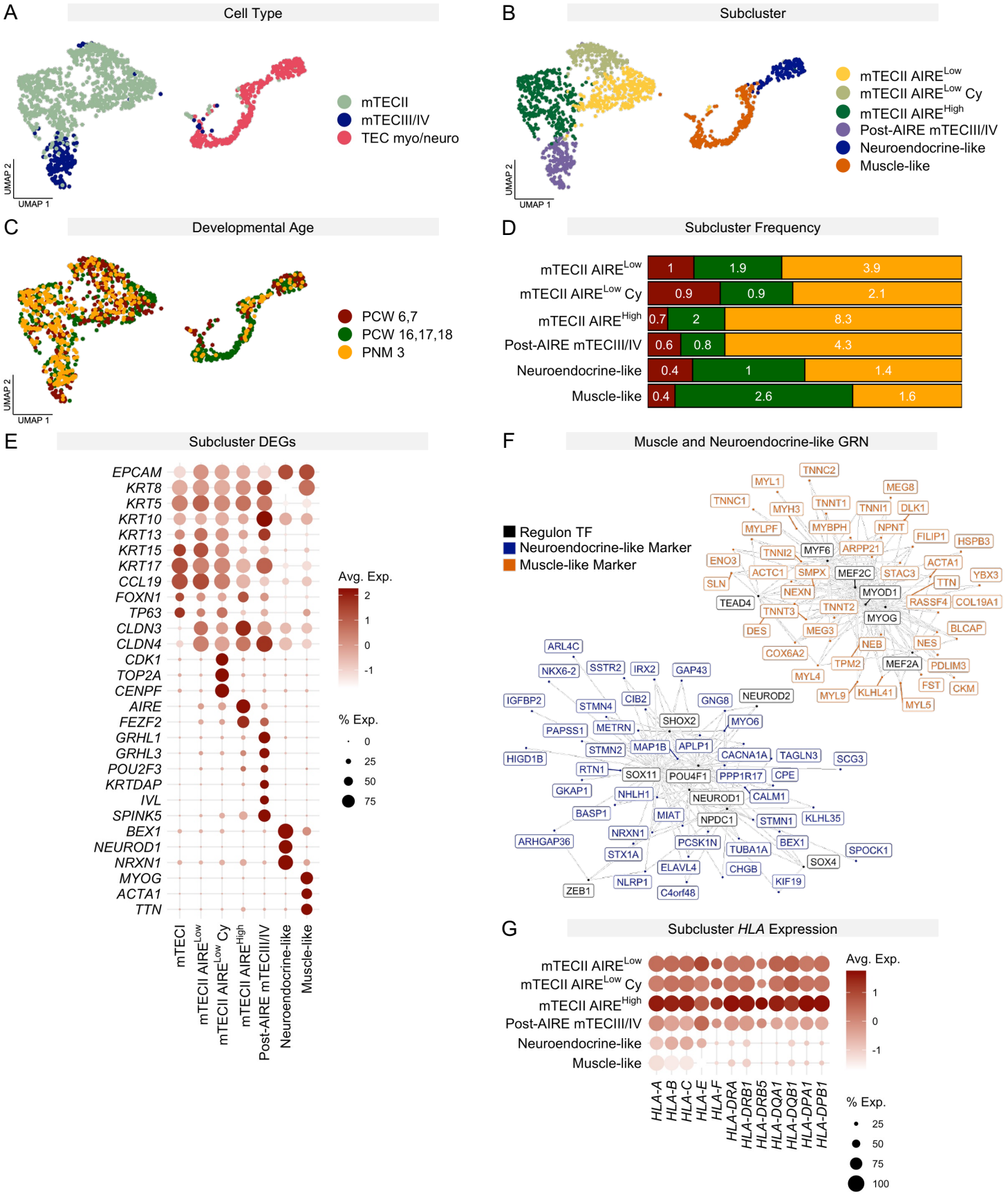
A
Cell Type
mTECII
mTECIII/IV
TEC myo/neuro
UMAP 2
UMAP 1
B
Subcluster
mTECII AIRE^Low
mTECII AIRE^Low Cy
mTECII AIRE^High
Post-AIRE mTECIII/IV
Neuroendocrine-like
Muscle-like
C
Developmental Age
PCW 6,7
PCW 16,17,18
PNM 3
D
Subcluster Frequency
mTECII AIRE^Low 1 1.9 3.9
mTECII AIRE^Low Cy 0.9 0.9 2.1
mTECII AIRE^High 0.7 2 8.3
Post-AIRE mTECIII/IV 0.6 0.8 4.3
Neuroendocrine-like 0.4 1 1.4
Muscle-like 0.4 2.6 1.6
E
Subcluster DEGs
EPCAM
KRT8
KRT5
KRT10
KRT13
KRT15
KRT17
CCL19
FOXN1
TP63
CLDN3
CLDN4
CDK1
TOP2A
CENPF
AIRE
FEZF2
GRHL1
GRHL3
POU2F3
KRTDAP
IVL
SPINK5
BEX1
NEUROD1
NRXN1
MYOG
ACTA1
TTN
mTECI
mTECII AIRE^Low
mTECII AIRE^Low Cy
mTECII AIRE^High
Post-AIRE mTECIII/IV
Neuroendocrine-like
Muscle-like
Avg. Exp.
% Exp.
F
Muscle and Neuroendocrine-like GRN
Regulon TF
Neuroendocrine-like Marker
Muscle-like Marker
G
Subcluster HLA Expression
HLA-A
HLA-B
HLA-C
HLA-E
HLA-F
HLA-DRA
HLA-DRB1
HLA-DRB5
HLA-DQA1
HLA-DQB1
HLA-DPA1
HLA-DPB1
Avg. Exp.
% Exp.

Figure 5. Expression patterns of rare TEC subsets.

(A) UMAP visualization of mTECII, mTECIII/IV, and TECmyo/neuro across all developmental time points. Cells colored by cell type, **(B)** cells colored by higher clustering granularity, **(C)** cells colored by developmental age. **(D)** Stacked bar chart representing cluster frequency of mTECII, mTECIII/IV, and TECmyo/neuro at embryonic (red), fetal (green) and postnatal (yellow) stages related to Fig. 4A. **(E)** Dot plot of marker gene expression defining select subclusters. **(F)** Network visualization of highly expressed regulons with inferred interactions between regulon defining transcription factors and target genes in neuroendocrine- and muscle-like TECs. **(G)** Dot plot of select HLA gene expression across individual TEC subsets.

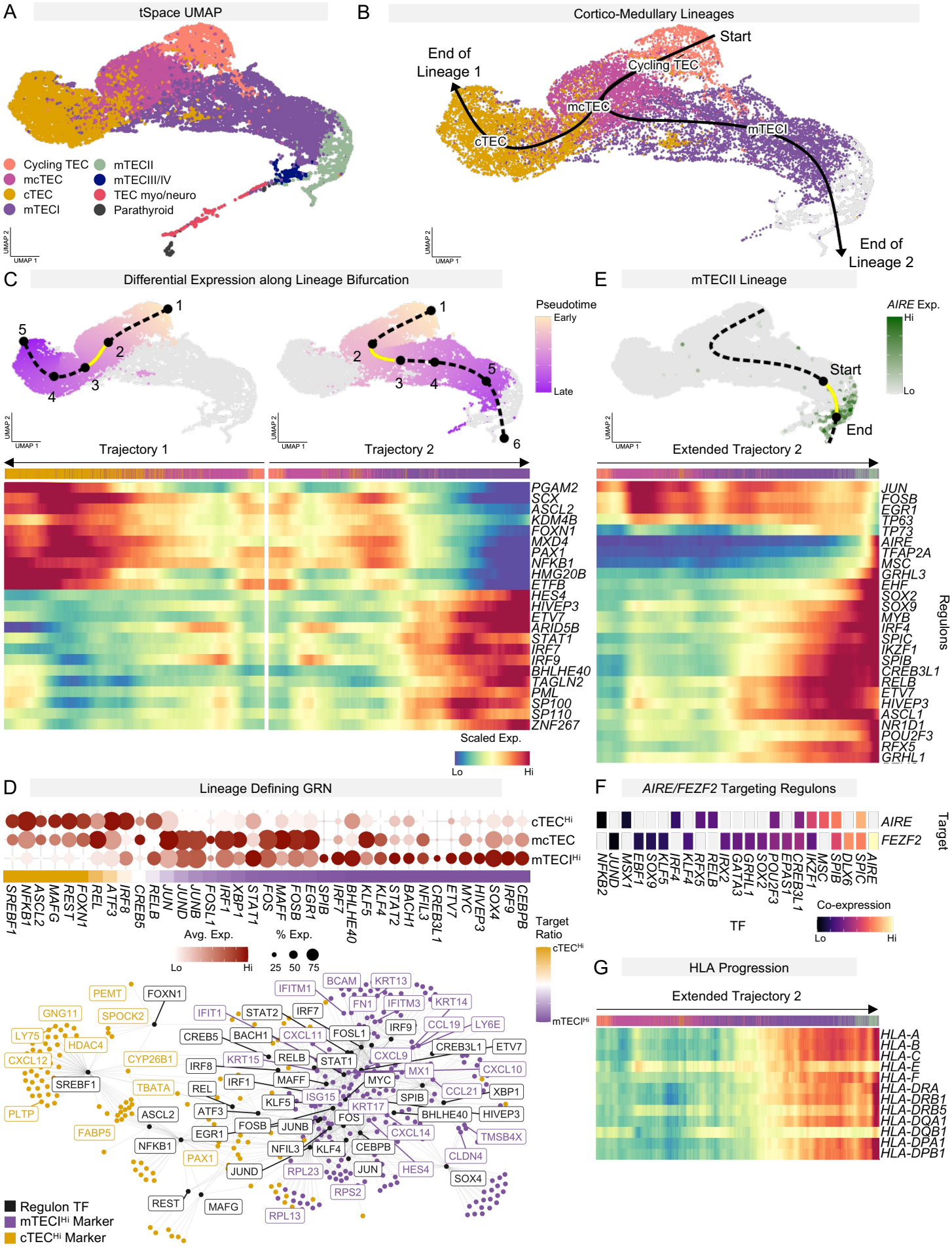
A
tSpace UMAP
Cycling TEC
mcTEC
cTEC
mTECI
mTECII
mTECIII/IV
TEC myo/neuro
Parathyroid
UMAP 2
UMAP 1
B
Cortico-Medullary Lineages
Start
End of Lineage 1
Cycling TEC
mcTEC
cTEC
mTECI
End of Lineage 2
C
Differential Expression along Lineage Bifurcation
Pseudotime
Early
Late
Trajectory 1
Trajectory 2
PGAM2
SCX
ASCL2
KDM4B
FOXN1
MXD4
PAX1
NFKB1
HMG20B
ETFB
HES4
HIVEP3
ETV7
ARID5B
STAT1
IRF7
IRF9
BHLHE40
TAGLN2
PML
SP100
SP110
ZNF267
Scaled Exp.
Lo
Hi
E
mTECII Lineage
AIRE Exp.
Start
End
Extended Trajectory 2
JUN
FOSB
EGR1
TP63
TP73
AIRE
TFAP2A
MSC
GRHL3
EHF
SOX2
SOX9
MYB
IRF4
SPIC
IKZF1
SPIB
CREB3L1
RELB
ETV7
HIVEP3
ASCL1
NR1D1
POU2F3
RFX5
GRHL1
Regulons
D
Lineage Defining GRN
cTECHi
mcTEC
mTECIHi
SREBF1
NFKB1
ASCL2
MAFG
REST
FOXN1
REL
ATF3
IRF8
CREB5
RELB
JUN
JUND
JUNB
FOSL1
IRF1
XBP1
STAT1
FOS
MAFF
FOSB
EGR1
SPIB
IRF7
BHLHE40
KLF5
KLF4
STAT2
BACH1
NFIL3
CREB3L1
ETV7
MYC
HIVEP3
SOX4
IRF9
CEBPB
Avg. Exp.
Lo
Hi
% Exp.
25
50
75
Target Ratio
cTECHi
mTECIHi
PEMT
FOXN1
GNG11
SPOCK2
LY75
HDAC4
CXCL12
CYP26B1
SREBF1
TBATA
PLTP
ASCL2
FABP5
NFKB1
PAX1
REST
MAFG
IFITM1
BCAM
KRT13
FN1
IFITM3
KRT14
IFIT1
STAT2
IRF7
IRF9
CCL19
LY6E
CREB5
BACH1
CXCL11
FOSL1
CREB3L1
ETV7
KRT15
RELB
STAT1
CXCL9
IRF8
MX1
CXCL10
IRF1
MAFF
MYC
REL
ISG15
SPIB
CCL21
XBP1
KLF5
KRT17
ATF3
FOS
BHLHE40
HIVEP3
EGR1
FOSB
JUNB
CXCL14
TMSB4X
NFIL3
KLF4
CEBPB
CLDN4
JUND
RPL23
JUN
HES4
SOX4
RPS2
RPL13
Regulon TF
mTECIHi Marker
cTECHi Marker
F
AIRE/FEZF2 Targeting Regulons
AIRE
FEZF2
Target
NFKB2
JUND
MSX1
EBF1
SOX9
KLF5
IRF4
KLF4
RFX5
RELB
IRX2
GATA3
GRHL1
SOX2
POU2F3
EPAS1
CREB3L1
IKZF1
MSC
SPIB
DLX6
SPIC
AIRE
TF
Co-expression
Lo
Hi
G
HLA Progression
Extended Trajectory 2
HLA-A
HLA-B
HLA-C
HLA-E
HLA-F
HLA-DRA
HLA-DRB1
HLA-DRB5
HLA-DQA1
HLA-DQB1
HLA-DPA1
HLA-DPB1

Figure 6. Regulatory networks defining cortical and medullary thymic epithelial lineages. **(A)** tSpace UMAP of TECs across advancing developmental and postnatal ages. Extended tSpace UMAP shown in supplementary figure S10. **(B)** Subset of tSpace UMAP from (A). Cortical and medullary lineage trajectories identified by Slingshot, plotted onto tSpace UMAP. **(C)** UMAP from (B) with cortical and medullary trajectories separately colored by pseudotime. Pseudotime intervals (knots) identified by TradeSeq are superimposed and numbered chronologically (top). Heatmaps representing the rolling average of select differentially expressed transcription factors between knots 2 and 3 along trajectories 1 (cortical) and 2 (medullary). From here onwards, heatmap color key corresponds to clusters in (A) (bottom). **(D)** Dot plot of regulon-defining transcription factors targeting lineage markers in populations with highest canonical lineage marker expression ($cTEC^{Hi}$ and $mTECI^{Hi}$) accompanied by heatmap representing the ratio of targets in the $cTEC^{Hi}$ and $mTECI^{Hi}$ populations, respectively (top). Network visualization of inferred interactions between regulon-defining transcription factors (black) and lineage markers (bottom). **(E)** tSpace UMAP from (B) with superimposed *AIRE* expression and extended medullary lineage trajectory. Highlighted pseudotime range corresponds to onset of *AIRE* expression (top). Heatmap representing the rolling average expression of select transcription factor regulons with differential expression within highlighted pseudotime range (bottom). **(F)** Heatmap of regulon-defining transcription factors targeting *AIRE* and *FEZF2.* **(G)** Heatmap of the rolling average expression of select *HLA* genes along the extended medullary lineage trajectory.

Supplemental Materials

1. Supplementary Figure S1
2. Supplementary Figure S2
3. Supplementary Figure S3
4. Supplementary Figure S4
5. Supplementary Figure S5
6. Supplementary Figure S6
7. Supplementary Figure S7
8. Supplementary Figure S8
9. Supplementary Figure S9
10. Supplementary Figure S10
11. Supplementary Figure S11
12. Supplementary Figure S12
13. Supplementary Figure S13
14. Supplementary Figure S14
15. Supplementary Table S1
16. Supplementary Table S2

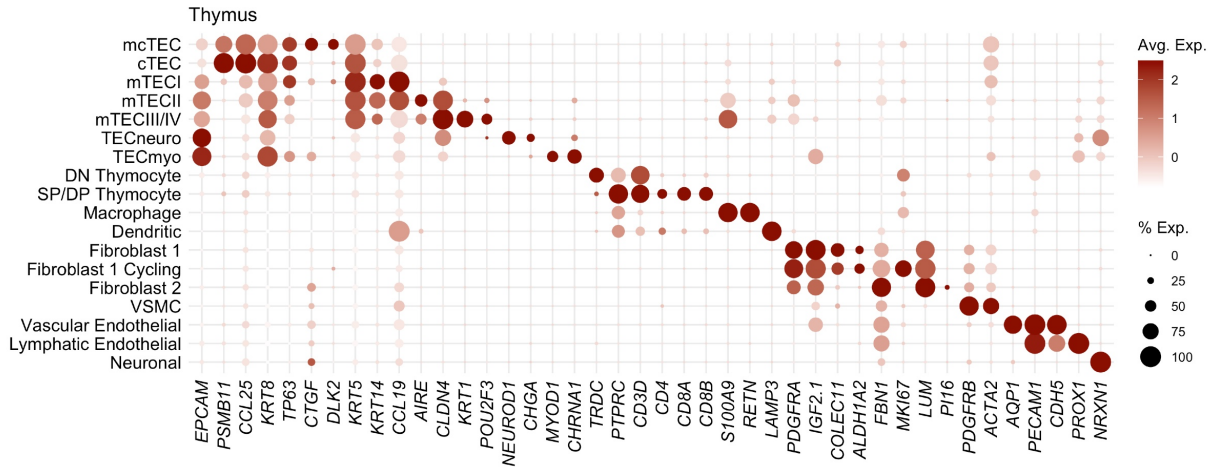
Thymus
mcTEC
cTEC
mTECI
mTECII
mTECIII/IV
TECneuro
TECmyo
DN Thymocyte
SP/DP Thymocyte
Macrophage
Dendritic
Fibroblast 1
Fibroblast 1 Cycling
Fibroblast 2
VSMC
Vascular Endothelial
Lymphatic Endothelial
Neuronal
EPCAM PSMB11 CCL25 KRT8 TP63 CTGF DLK2 KRT5 KRT14 CCL19 AIRE CLDN4 KRT1 POU2F3 NEUROD1 CHGA MYOD1 CHRNA1 TRDC PTPRC CD3D CD4 CD8A CD8B S100A9 RETN LAMP3 PDGFRA IGF2.1 COLEC11 ALDH1A2 FBN1 MKI67 LUM PI16 PDGFRB ACTA2 AQP1 PECAM1 CDH5 PROX1 NRXN1
Avg. Exp.
2
1
0
% Exp.
0
25
50
75
100

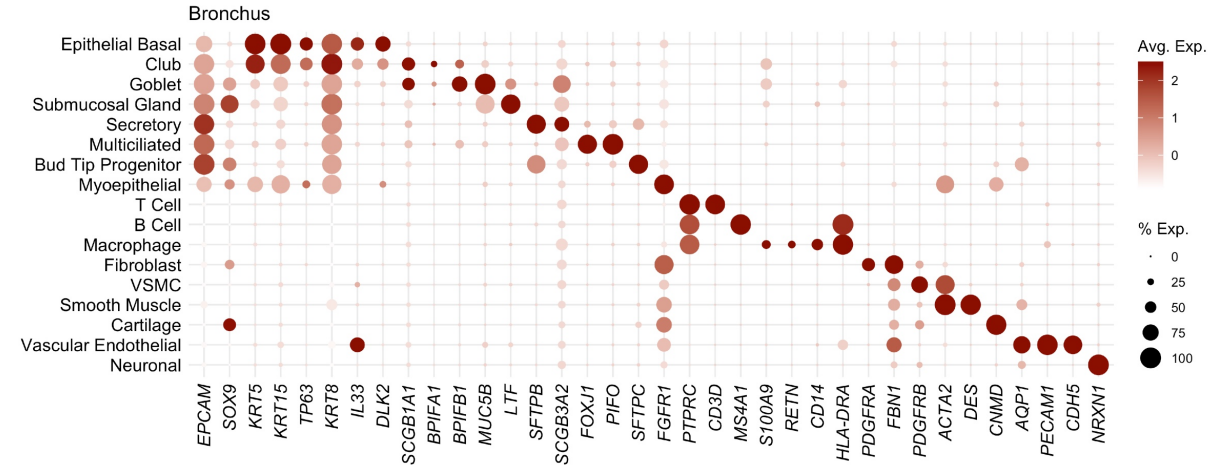
Bronchus
Epithelial Basal
Club
Goblet
Submucosal Gland
Secretory
Multiciliated
Bud Tip Progenitor
Myoepithelial
T Cell
B Cell
Macrophage
Fibroblast
VSMC
Smooth Muscle
Cartilage
Vascular Endothelial
Neuronal
EPCAM SOX9 KRT5 KRT15 TP63 KRT8 IL33 DLK2 SCGB1A1 BPIFA1 BPIFB1 MUC5B LTF SFTPB SCGB3A2 FOXJ1 PIFO SFTPC FGFR1 PTPRC CD3D MS4A1 S100A9 RETN CD14 HLA-DRA PDGFRA FBN1 PDGFRB ACTA2 DES CNMD AQP1 PECAM1 CDH5 NRXN1
Avg. Exp.
2
1
0
% Exp.
0
25
50
75
100

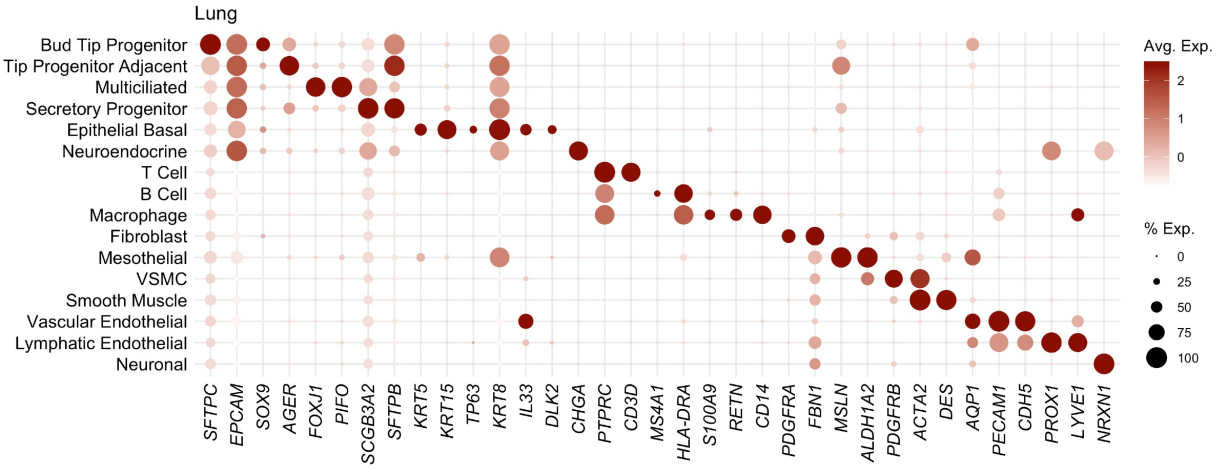
Lung
Bud Tip Progenitor
Bud Tip Progenitor Adjacent
Multiciliated
Secretory Progenitor
Epithelial Basal
Neuroendocrine
T Cell
B Cell
Macrophage
Fibroblast
Mesothelial
VSMC
Smooth Muscle
Vascular Endothelial
Lymphatic Endothelial
Neuronal
SFTPC EPCAM SOX9 AGER FOXJ1 PIFO SCGB3A2 SFTPB KRT5 KRT15 TP63 KRT8 IL33 DLK2 CHGA PTPRC CD3D MS4A1 HLA-DRA S100A9 RETN CD14 PDGFRA FBN1 MSLN ALDH1A2 PDGFRB ACTA2 DES AQP1 PECAM1 CDH5 PROX1 LYVE1 NRXN1
Avg. Exp.
2
1
0
% Exp.
0
25
50
75
100

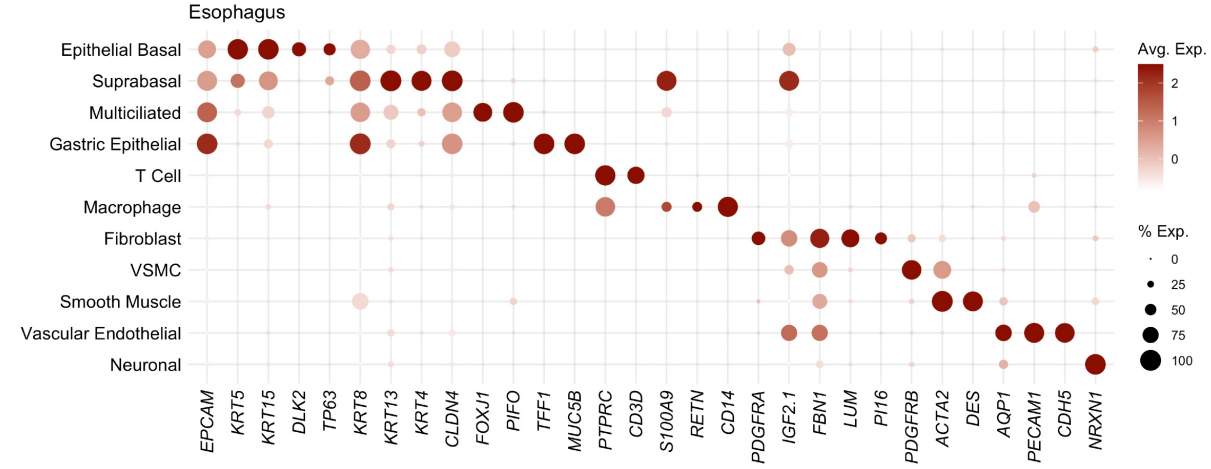
Esophagus
Epithelial Basal
Suprabasal
Multiciliated
Gastric Epithelial
T Cell
Macrophage
Fibroblast
VSMC
Smooth Muscle
Vascular Endothelial
Neuronal
EPCAM KRT5 KRT15 DLK2 TP63 KRT8 KRT13 KRT4 CLDN4 FOXJ1 PIFO TFF1 MUC5B PTPRC CD3D S100A9 RETN CD14 PDGFRA IGF2.1 FBN1 LUM PI16 PDGFRB ACTA2 DES AQP1 PECAM1 CDH5 NRXN1
Avg. Exp.
2
1
0
% Exp.
0
25
50
75
100

Supplementary Figure S1

Dot plot of marker gene expression for annotated cell types in fetal thymus, bronchus, lung, and esophagus.

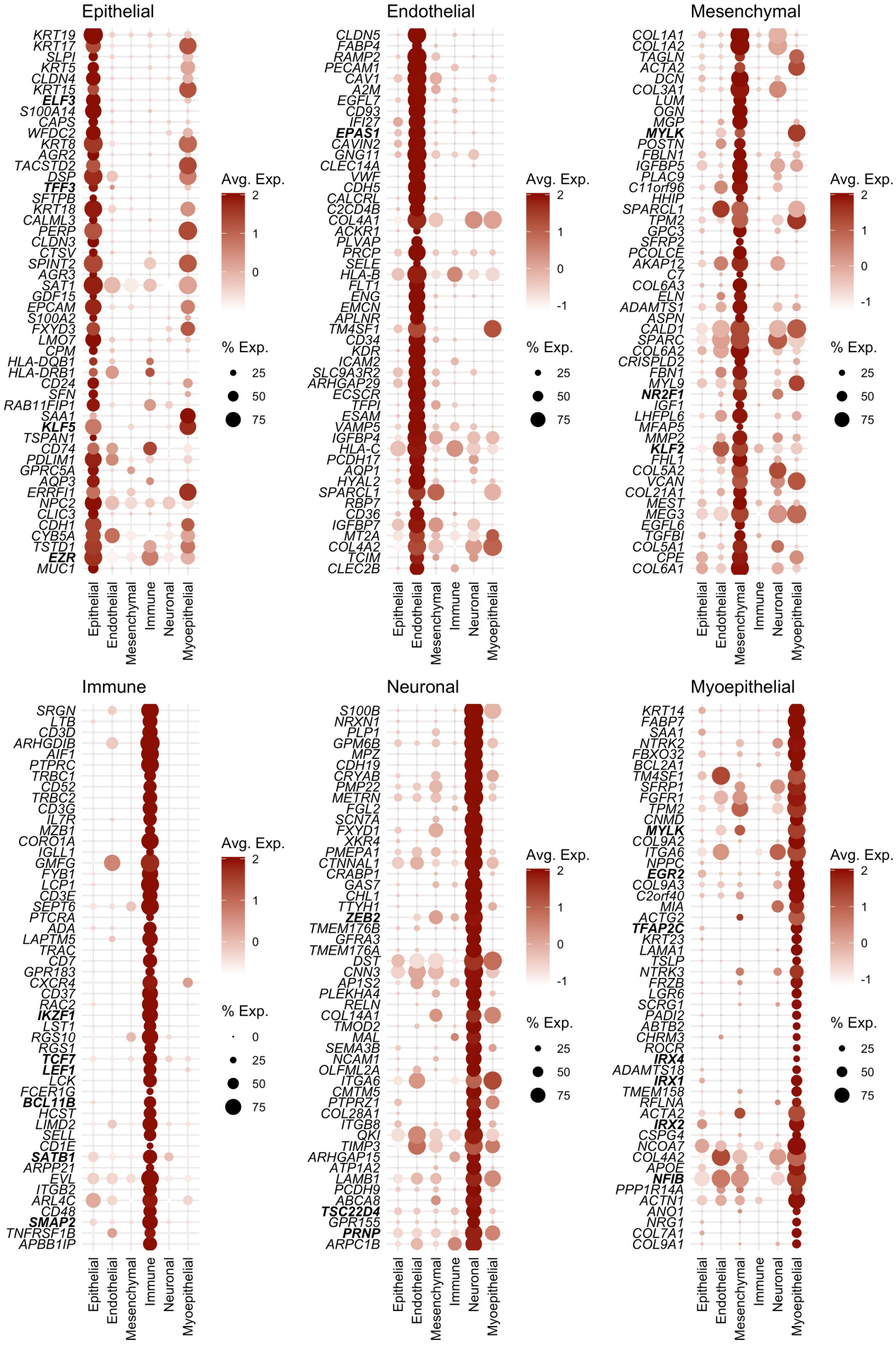
Epithelial
KRT19
KRT17
SLPI
KRT5
CLDN4
KRT15
ELF3
S100A14
CAPS
WFDC2
KRT8
AGR2
TACSTD2
DSP
TFF3
SFTPB
KRT18
CALML3
PERP
CLDN3
CTSV
SPINT2
AGR3
SAT1
GDF15
EPCAM
S100A2
FXYD3
LMO7
CPM
HLA-DQB1
HLA-DRB1
CD24
SFN
RAB11FIP1
SAA1
KLF5
TSPAN1
CD74
PDLIM1
GPRC5A
AQP3
ERRFI1
NPC2
CLIC3
CDH1
CYB5A
TSTD1
EZR
MUC1
Epithelial
Endothelial
Mesenchymal
Immune
Neuronal
Myoepithelial
Avg. Exp.
2
1
0
% Exp.
25
50
75
Endothelial
CLDN5
FABP4
RAMP2
PECAM1
CAV1
A2M
EGFL7
CD93
IFI27
EPAS1
CAVIN2
GNG11
CLEC14A
VWF
CDH5
CALCRL
C2CD4B
COL4A1
ACKR1
PLVAP
PRCP
SELE
HLA-B
FLT1
ENG
EMCN
APLNR
TM4SF1
CD34
KDR
ICAM2
SLC9A3R2
ARHGAP29
ECSCR
TFPI
ESAM
VAMP5
IGFBP4
HLA-C
PCDH17
AQP1
HYAL2
SPARCL1
RBP7
CD36
IGFBP7
MT2A
COL4A2
TCIM
CLEC2B
Epithelial
Endothelial
Mesenchymal
Immune
Neuronal
Myoepithelial
Avg. Exp.
2
1
0
-1
% Exp.
25
50
75
Mesenchymal
COL1A1
COL1A2
TAGLN
ACTA2
DCN
COL3A1
LUM
OGN
MGP
MYLK
POSTN
FBLN1
IGFBP5
PLAC9
C11orf96
HHIP
SPARCL1
TPM2
GPC3
SFRP2
PCOLCE
AKAP12
C7
COL6A3
ELN
ADAMTS1
ASPN
CALD1
SPARC
COL6A2
CRISPLD2
FBN1
MYL9
NR2F1
IGF1
LHFPL6
MFAP5
MMP2
KLF2
FHL1
COL5A2
VCAN
COL21A1
MEST
MEG3
EGFL6
TGFBI
COL5A1
CPE
COL6A1
Epithelial
Endothelial
Mesenchymal
Immune
Neuronal
Myoepithelial
Avg. Exp.
2
1
0
-1
% Exp.
25
50
75
Immune
SRGN
LTB
CD3D
ARHGDIB
AIF1
PTPRC
TRBC1
CD52
TRBC2
CD3G
IL7R
MZB1
CORO1A
IGLL1
GMFG
FYB1
LCP1
CD3E
SEPT6
PTCRA
ADA
LAPTM5
TRAC
CD7
GPR183
CXCR4
CD37
RAC2
IKZF1
LST1
RGS10
RGS1
TCF7
LEF1
LCK
FCER1G
BCL11B
HCST
LIMD2
SELL
CD1E
SATB1
ARPP21
EVL
ITGB2
ARL4C
CD48
SMAP2
TNFRSF1B
APBB1IP
Epithelial
Endothelial
Mesenchymal
Immune
Neuronal
Myoepithelial
Avg. Exp.
2
1
0
% Exp.
0
25
50
75
Neuronal
S100B
NRXN1
PLP1
GPM6B
MPZ
CDH19
CRYAB
PMP22
METRN
FGL2
SCN7A
FXYD1
XKR4
PMEPA1
CTNNAL1
CRABP1
GAS7
CHL1
TTYH1
ZEB2
TMEM176B
GFRA3
TMEM176A
DST
CNN3
AP1S2
PLEKHA4
RELN
COL14A1
TMOD2
MAL
SEMA3B
NCAM1
OLFML2A
ITGA6
CMTM5
PTPRZ1
COL28A1
ITGB8
QKI
TIMP3
ARHGAP15
ATP1A2
LAMB1
PCDH9
ABCA8
TSC22D4
GPR155
PRNP
ARPC1B
Epithelial
Endothelial
Mesenchymal
Immune
Neuronal
Myoepithelial
Avg. Exp.
2
1
0
-1
% Exp.
25
50
75
Myoepithelial
KRT14
FABP7
SAA1
NTRK2
FBXO32
BCL2A1
TM4SF1
SFRP1
FGFR1
TPM2
CNMD
MYLK
COL9A2
ITGA6
NPPC
EGR2
COL9A3
C2orf40
MIA
ACTG2
TFAP2C
KRT23
LAMA1
TSLP
NTRK3
FRZB
LGR6
SCRG1
PADI2
ABTB2
CHRM3
ROCR
IRX4
ADAMTS18
IRX1
TMEM158
RFLNA
ACTA2
IRX2
CSPG4
NCOA7
COL4A2
APOE
NFIB
PPP1R14A
ACTN1
ANO1
NRG1
COL7A1
COL9A1
Epithelial
Endothelial
Mesenchymal
Immune
Neuronal
Myoepithelial
Avg. Exp.
2
1
0
-1
% Exp.
25
50
75

Supplementary Figure S2

Dot plots of top differentially expressed genes for all major tissue types across cells from human fetal thymus, bronchus, lung and esophagus (transcription factors are labeled in bold).

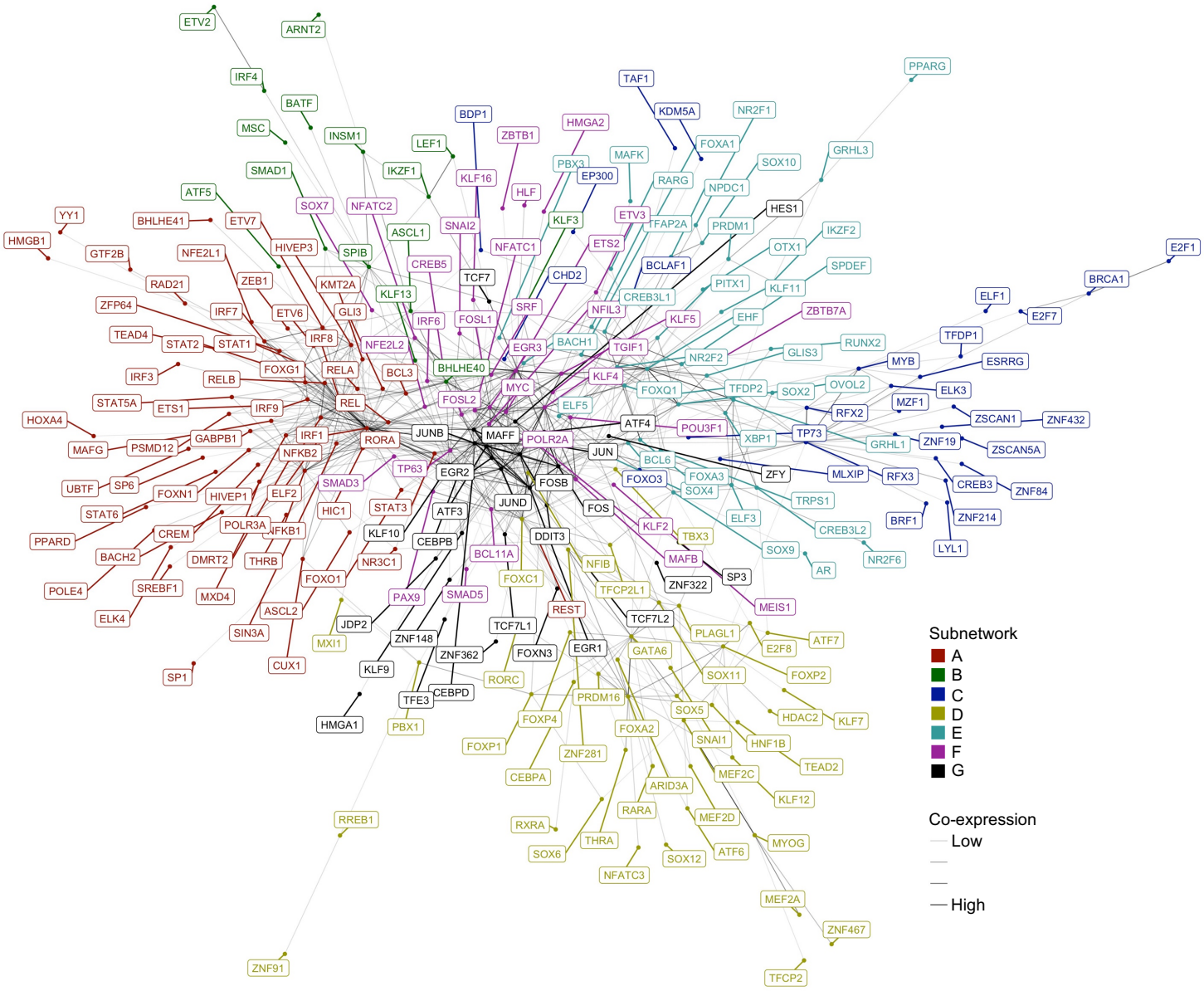
ETV2
ARNT2
IRF4
BATF
MSC
INSM1
SMAD1
ATF5
YY1
BHLHE41
ETV7
HMGB1
GTF2B
NFE2L1
RAD21
ZEB1
ZFP64
IRF7
ETV6
TEAD4
STAT2
STAT1
IRF8
IRF3
RELB
FOXG1
STAT5A
ETS1
IRF9
HOXA4
MAFG
PSMD12
GABPB1
UBTF
SP6
FOXN1
HIVEP1
STAT6
PPARD
CREM
BACH2
DMRT2
THRB
POLE4
SREBF1
MXD4
ELK4
SIN3A
SP1
CUX1
ASCL2
SOX7
NFATC2
HIVEP3
SPIB
KMT2A
GLI3
NFE2L2
RELA
REL
IRF1
NFKB2
RORA
SMAD3
HIC1
STAT3
KLF10
NR3C1
FOXO1
JDP2
MXI1
ZNF148
KLF9
TFE3
HMGA1
PBX1
ZNF362
CEBPD
ASCL1
CREB5
KLF13
IRF6
BCL3
BHLHE40
FOSL2
JUNB
TP63
EGR2
ATF3
CEBPB
PAX9
SMAD5
BDP1
LEF1
IKZF1
KLF16
SNAI2
TCF7
FOSL1
SRF
EGR3
MYC
MAFF
POLR2A
JUND
FOSB
DDIT3
BCL11A
FOXC1
REST
TCF7L1
FOXN3
EGR1
RORC
FOXP4
FOXP1
CEBPA
ZNF281
RREB1
RXRA
SOX6
THRA
NFATC3
ZNF91
ZBTB1
HLF
NFATC1
CHD2
HMGA2
PBX3
EP300
KLF3
ETS2
NFIL3
BACH1
TGIF1
KLF4
ELF5
ATF4
JUN
BCL6
FOXO3
FOS
KLF2
TBX3
NFIB
TFCP2L1
ZNF322
MAFB
SP3
MEIS1
TCF7L2
PLAGL1
GATA6
PRDM16
FOXA2
ARID3A
RARA
SOX12
ATF6
MEF2D
MEF2C
MYOG
KLF12
TEAD2
HNF1B
SNAI1
SOX5
HDAC2
KLF7
SOX11
FOXP2
E2F8
ATF7
MEF2A
ZNF467
TFCP2
TAF1
KDM5A
NR2F1
FOXA1
MAFK
RARG
NPDC1
SOX10
GRHL3
PPARG
HES1
ETV3
TFAP2A
PRDM1
IKZF2
OTX1
SPDEF
BCLAF1
PITX1
KLF11
CREB3L1
KLF5
EHF
ZBTB7A
RUNX2
GLIS3
NR2F2
TFDP2
SOX2
OVOL2
MYB
ESRRG
ELK3
MZF1
RFX2
ZSCAN1
ZNF432
TP73
XBP1
GRHL1
ZNF19
ZSCAN5A
ZFY
MLXIP
RFX3
CREB3
ZNF84
TRPS1
ELF3
CREB3L2
BRF1
ZNF214
LYL1
NR2F6
AR
SOX9
FOXA3
SOX4
E2F1
BRCA1
ELF1
E2F7
TFDP1
Subnetwork
A
B
C
D
E
F
G
Co-expression
Low
High

Supplementary Figure S3

Fully annotated version of network from Fig. 2C. Visualization of transcription factor regulon subnetworks in all fetal epithelial cells defined by Leiden algorithm. Line thickness corresponds to co-expression of interaction.

KEGG_OXIDATIVE_PHOSPHORYLATION
REACTOME_RESPIRATORY_ELECTRON_TRANSPORT
REACTOME_RESPIRATORY_ELECTRON_TRANSPORT_ATP_SYNTHESIS_BY_CHEMIOSMOTIC_COUPLING_AND_HEAT_PRODUCTION_BY_UNCOUPLING_PROTEINS
KEGG_PARKINSONS_DISEASE
REACTOME_METABOLISM_OF_AMINO_ACIDS_AND_DERIVATIVES
REACTOME_DISEASES_OF_METABOLISM
REACTOME_CELLULAR_RESPONSE_TO_STARVATION
REACTOME_ACTIVATION_OF_THE_MRNA_UPON_BINDING_OF_THE_CAP_BINDING_COMPLEX_AND_EIFS_AND_SUBSEQUENT_BINDING_TO_43S
REACTOME_RESPONSE_OF_EIF2AK4_GCN2_TO_AMINO_ACID_DEFICIENCY
REACTOME_SURFACTANT_METABOLISM
REACTOME_NUCLEAR_EVENTS_KINASE_AND_TRANSCRIPTION_FACTOR_ACTIVATION
KEGG_HYPERTROPHIC_CARDIOMYOPATHY_HCM
KEGG_DILATED_CARDIOMYOPATHY
REACTOME_NGF_STIMULATED_TRANSCRIPTION
REACTOME_NEUTROPHIL_DEGRANULATION
KEGG_CELL_ADHESION_MOLECULES_CAMS
REACTOME_KERATINIZATION
REACTOME_FORMATION_OF_THE_CORNIFIED_ENVELOPE
REACTOME_ANTIMICROBIAL_PEPTIDES
REACTOME_GENERATION_OF_SECOND_MESSENGER_MOLECULES
REACTOME_G_ALPHA_I_SIGNALLING_EVENTS
KEGG_TOLL_LIKE_RECEPTOR_SIGNALING_PATHWAY
REACTOME_INTERLEUKIN_10_SIGNALING
KEGG_NATURAL_KILLER_CELL_MEDIATED_CYTOTOXICITY
REACTOME_DDX58_IFIH1_MEDIATED_INDUCTION_OF_INTERFERON_ALPHA_BETA
KEGG_CHEMOKINE_SIGNALING_PATHWAY
REACTOME_INTERFERON_SIGNALING
REACTOME_ANTIVIRAL_MECHANISM_BY_IFN_STIMULATED_GENES
REACTOME_ANTIGEN_PRESENTATION_FOLDING_ASSEMBLY_AND_PEPTIDE_LOADING_OF_CLASS_I_MHC
REACTOME_INTERFERON_ALPHA_BETA_SIGNALING
REACTOME_CHEMOKINE_RECEPTORS_BIND_CHEMOKINES
REACTOME_ANTIGEN_PROCESSING_CROSS_PRESENTATION
REACTOME_INTERFERON_GAMMA_SIGNALING
REACTOME_STABILIZATION_OF_P53
REACTOME_DEGRADATION_OF_GLI1_BY_THE_PROTEASOME
REACTOME_ASYMMETRIC_LOCALIZATION_OF_PCP_PROTEINS
REACTOME_DEGRADATION_OF_DVL
REACTOME_DEFECTIVE_CFTR_CAUSES_CYSTIC_FIBROSIS
KEGG_ANTIGEN_PROCESSING_AND_PRESENTATION
REACTOME_MHC_CLASS_II_ANTIGEN_PRESENTATION
KEGG_VIRAL_MYOCARDITIS
REACTOME_CROSS_PRESENTATION_OF_SOLUBLE_EXOGENOUS_ANTIGENS_ENDOSOMES
KEGG_PROTEASOME
REACTOME_TCR_SIGNALING
KEGG_LEISHMANIA_INFECTION
KEGG_TYPE_I_DIABETES_MELLITUS
KEGG_GRAFT_VERSUS_HOST_DISEASE
KEGG_ALLOGRAFT_REJECTION
REACTOME_COSTIMULATION_BY_THE_CD28_FAMILY
KEGG_AUTOIMMUNE_THYROID_DISEASE
KEGG_SYSTEMIC_LUPUS_ERYTHEMATOSUS
KEGG_INTESTINAL_IMMUNE_NETWORK_FOR_IGA_PRODUCTION
KEGG_ASTHMA
REACTOME_METABOLISM_OF_RNA
REACTOME_TRANSLATION
REACTOME_SIGNALING_BY_ROBO_RECEPTORS
REACTOME_SRP_DEPENDENT_COTRANSLATIONAL_PROTEIN_TARGETING_TO_MEMBRANE
REACTOME_INFLUENZA_INFECTION
REACTOME_EUKARYOTIC_TRANSLATION_ELONGATION
REACTOME_MRNA_SPLICING
REACTOME_PROCESSING_OF_CAPPED_INTRON_CONTAINING_PRE_MRNA
REACTOME_REGULATION_OF_EXPRESSION_OF_SLITS_AND_ROBOS
REACTOME_EUKARYOTIC_TRANSLATION_INITIATION
REACTOME_RRNA_PROCESSING
KEGG_RIBOSOME
REACTOME_SELENOAMINO_ACID_METABOLISM
REACTOME_NONSENSE_MEDIATED_DECAY_NMD
REACTOME_COLLAGEN_CHAIN_TRIMERIZATION
REACTOME_SIGNALING_BY_PDGF
mcTEC T
cTEC T
mTECI T
mTECII T
Epi. Basal B
BTP L
Epi. Basal E
-log10(p.adjust)
4
6
8
enrichmentScore
0.75
0.50
0.25
0.00

Supplementary Figure S4

Dot plot of enriched gene sets across select epithelial cell subpopulations for thymus, bronchus, lung and esophagus at fetal stages of development. Dot size corresponds to p-value, color corresponds to enrichment score.

A

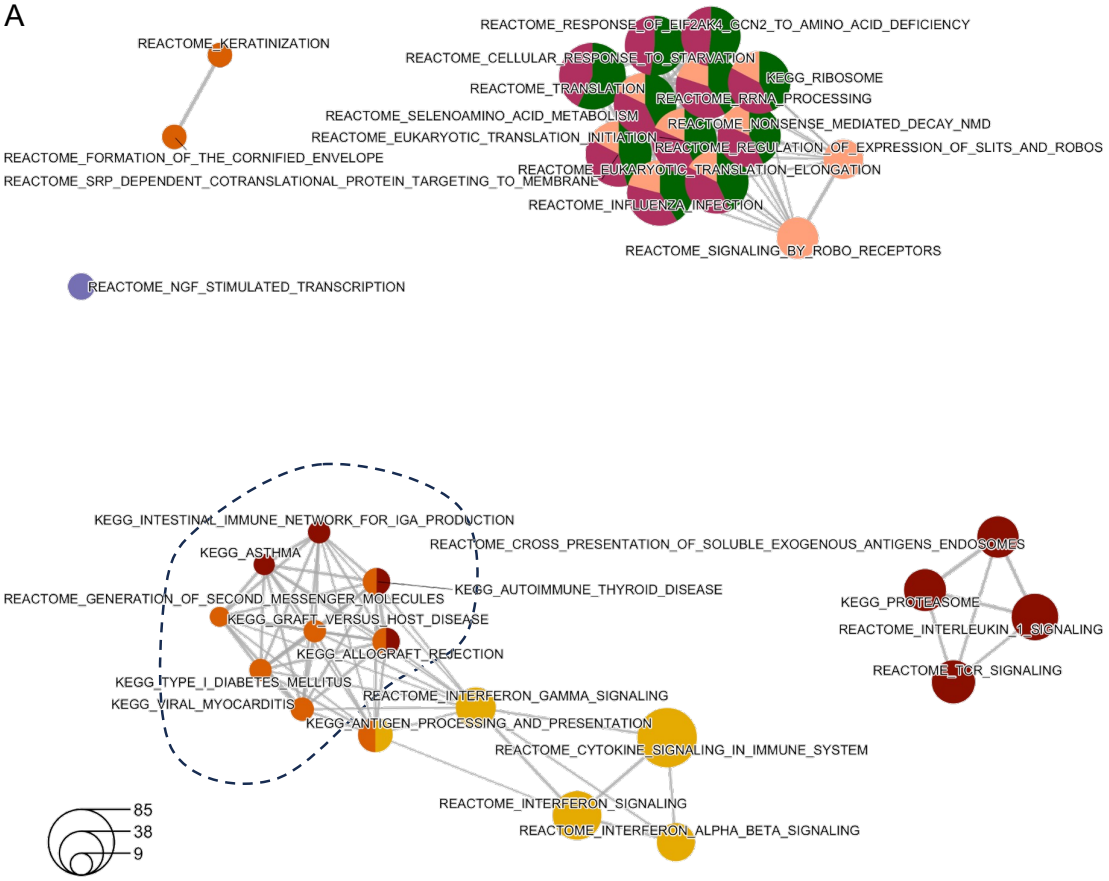
REACTOME_KERATINIZATION
REACTOME_FORMATION_OF_THE_CORNIFIED_ENVELOPE
REACTOME_SRP_DEPENDENT_COTRANSLATIONAL_PROTEIN_TARGETING_TO_MEMBRANE
REACTOME_NGF_STIMULATED_TRANSCRIPTION
REACTOME_RESPONSE_OF_EIF2AK4_GCN2_TO_AMINO_ACID_DEFICIENCY
REACTOME_CELLULAR_RESPONSE_TO_STARVATION
REACTOME_TRANSLATION
KEGG_RIBOSOME
REACTOME_RRNA_PROCESSING
REACTOME_SELENOAMINO_ACID_METABOLISM
REACTOME_NONSENSE_MEDIATED_DECAY_NMD
REACTOME_EUKARYOTIC_TRANSLATION_INITIATION
REACTOME_REGULATION_OF_EXPRESSION_OF_SLITS_AND_ROBOS
REACTOME_EUKARYOTIC_TRANSLATION_ELONGATION
REACTOME_INFLUENZA_INFECTION
REACTOME_SIGNALING_BY_ROBO_RECEPTORS
KEGG_INTESTINAL_IMMUNE_NETWORK_FOR_IGA_PRODUCTION
KEGG_ASTHMA
REACTOME_CROSS_PRESENTATION_OF_SOLUBLE_EXOGENOUS_ANTIGENS_ENDOSOMES
REACTOME_GENERATION_OF_SECOND_MESSENGER_MOLECULES
KEGG_AUTOIMMUNE_THYROID_DISEASE
KEGG_GRAFT_VERSUS_HOST_DISEASE
KEGG_PROTEASOME
REACTOME_INTERLEUKIN_1_SIGNALING
KEGG_ALLOGRAFT_REJECTION
REACTOME_TCR_SIGNALING
KEGG_TYPE_I_DIABETES_MELLITUS
KEGG_VIRAL_MYOCARDITIS
REACTOME_INTERFERON_GAMMA_SIGNALING
KEGG_ANTIGEN_PROCESSING_AND_PRESENTATION
REACTOME_CYTOKINE_SIGNALING_IN_IMMUNE_SYSTEM
REACTOME_INTERFERON_SIGNALING
REACTOME_INTERFERON_ALPHA_BETA_SIGNALING
85
38
9
Cluster
BTP L
cTEC T
Epi. Basal B
Epi. Basal E
mcTEC T
mTECI T
mTECII T

B

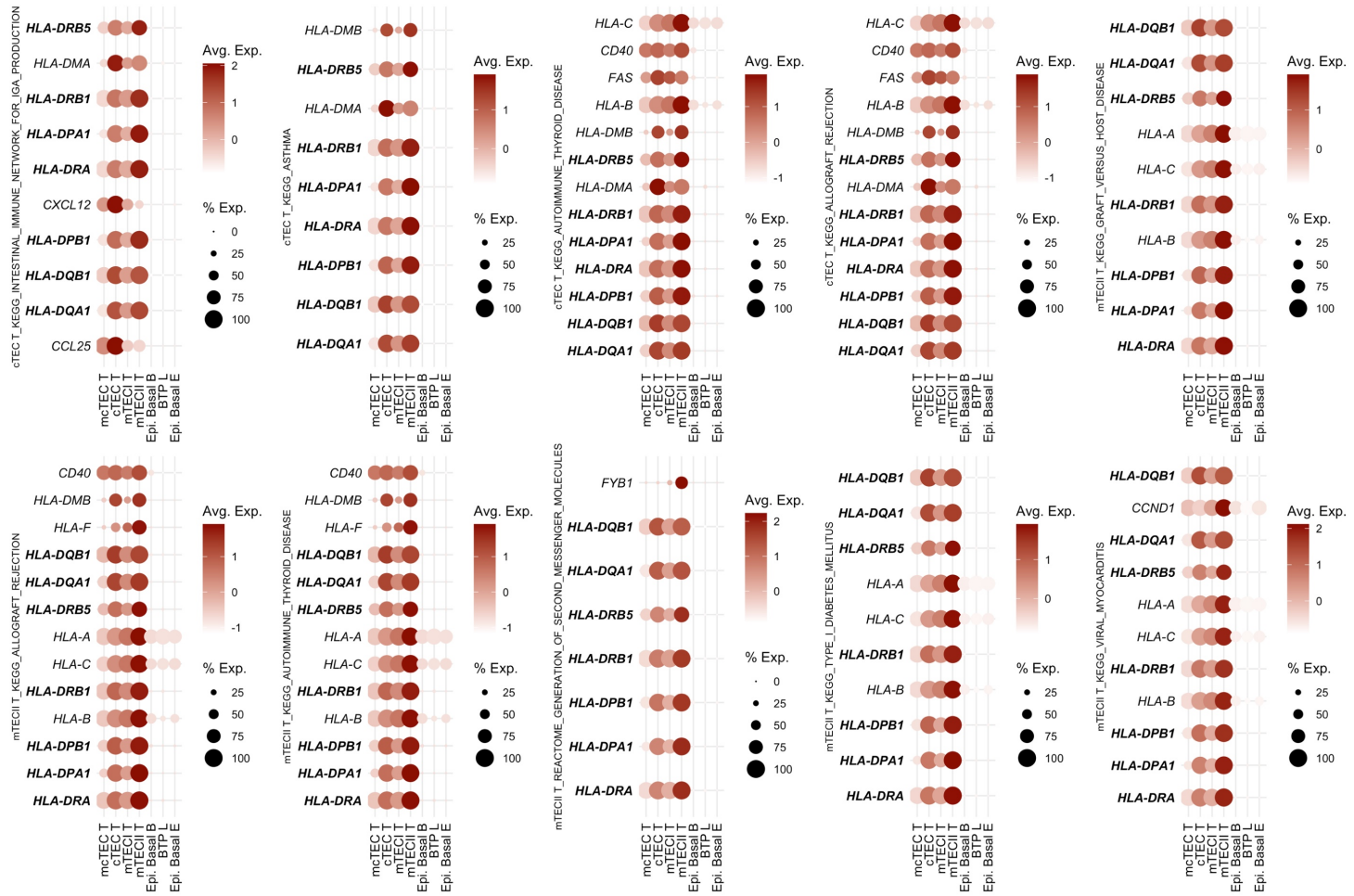
cTEC T_KEGG_INTESTINAL_IMMUNE_NETWORK_FOR_IGA_PRODUCTION
HLA-DRB5
HLA-DMA
HLA-DRB1
HLA-DPA1
HLA-DRA
CXCL12
HLA-DPB1
HLA-DQB1
HLA-DQA1
CCL25
cTEC T_KEGG_ASTHMA
HLA-DMB
cTEC T_KEGG_AUTOIMMUNE_THYROID_DISEASE
HLA-C
CD40
FAS
HLA-B
cTEC T_KEGG_ALLOGRAFT_REJECTION
mTECII T_KEGG_GRAFT_VERSUS_HOST_DISEASE
HLA-DQB1
HLA-DQA1
HLA-A
mTECII T_KEGG_ALLOGRAFT_REJECTION
HLA-F
mTECII T_KEGG_AUTOIMMUNE_THYROID_DISEASE
mTECII T_REACTOME_GENERATION_OF_SECOND_MESSENGER_MOLECULES
FYB1
mTECII T_KEGG_TYPE_I_DIABETES_MELLITUS
mTECII T_KEGG_VIRAL_MYOCARDITIS
CCND1
Avg. Exp.
% Exp.
mcTEC T
cTEC T
mTECI T
mTECII T
Epi. Basal B
BTP L
Epi. Basal E

Supplementary Figure S5

(A) Fully annotated version of GSEA network found from Fig. 3B. Network visualization of differentially expressed GSEA gene sets across select epithelial cell subpopulations for thymus, bronchus, lung and esophagus at fetal stages of development. Each node represents a specific GSEA gene set ($p<0.05$). Edges between nodes denote a significant number of shared genes between nodes. Node size reflects the number of genes within each gene set. **(B)** Enriched genes from the gene sets within the dotted circle are visualized in dot plots. Emboldened genes correspond to common genes across dot plots.

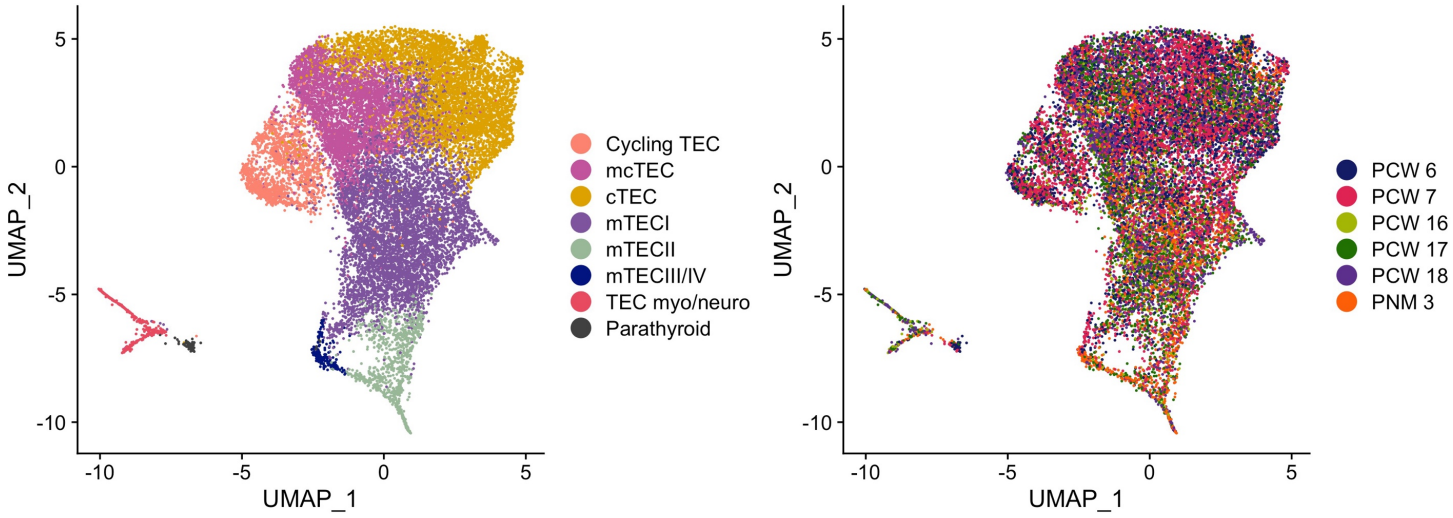
UMAP_2
UMAP_1
5
0
-5
-10
-10
-5
0
5
Cycling TEC
mcTEC
cTEC
mTECI
mTECII
mTECIII/IV
TEC myo/neuro
Parathyroid
PCW 6
PCW 7
PCW 16
PCW 17
PCW 18
PNM 3

Supplementary Figure S6

UMAP visualization of integrated TEC across all sampled time points, colored by developmental/postnatal age (left) and cell type (right).

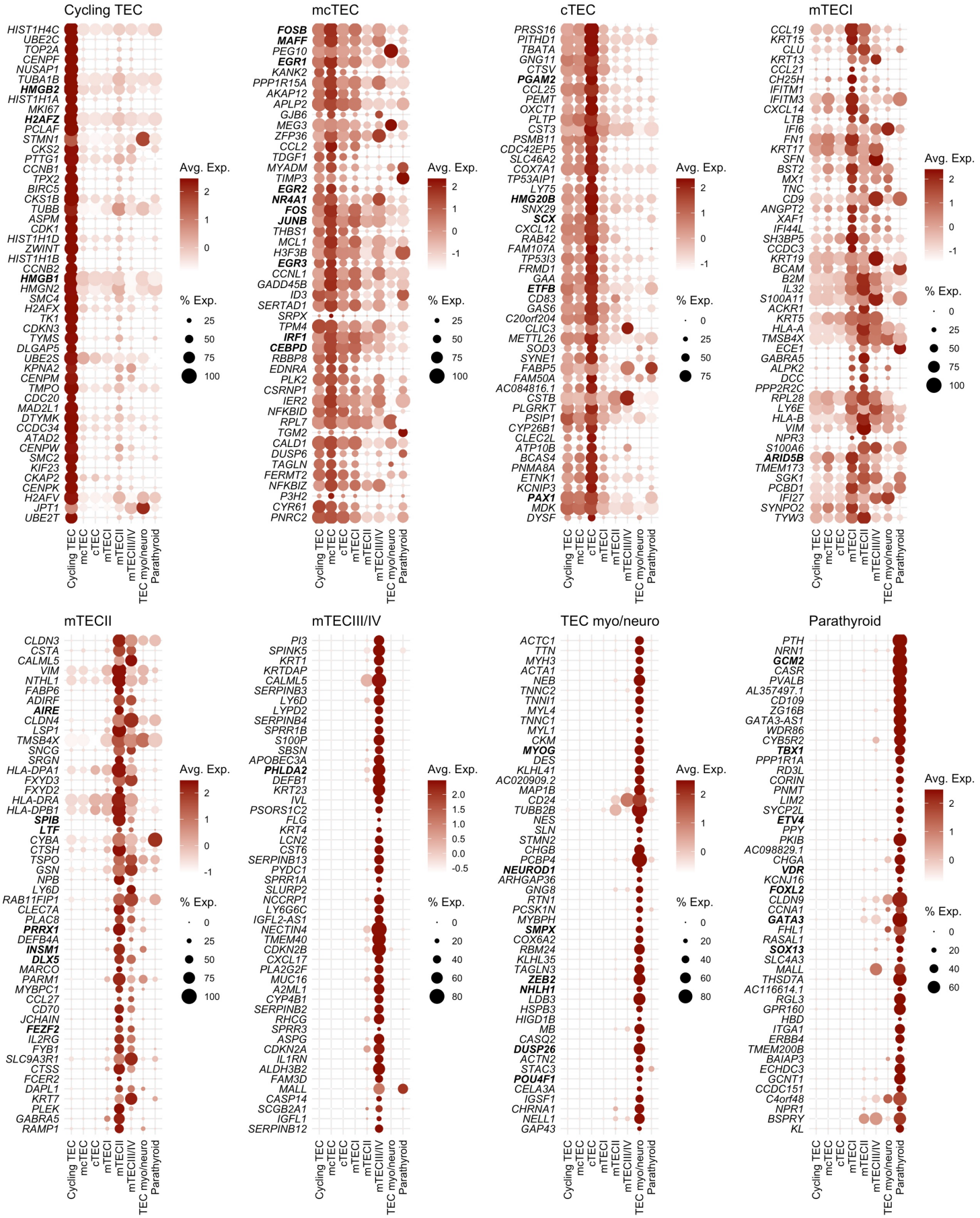
Cycling TEC
HIST1H4C
UBE2C
TOP2A
CENPF
NUSAP1
TUBA1B
HMGB2
HIST1H1A
MKI67
H2AFZ
PCLAF
STMN1
CKS2
PTTG1
CCNB1
TPX2
BIRC5
CKS1B
TUBB
ASPM
CDK1
HIST1H1D
ZWINT
HIST1H1B
CCNB2
HMGB1
HMGN2
SMC4
H2AFX
TK1
CDKN3
TYMS
DLGAP5
UBE2S
KPNA2
CENPM
TMPO
CDC20
MAD2L1
DTYMK
CCDC34
ATAD2
CENPW
SMC2
KIF23
CKAP2
CENPK
H2AFV
JPT1
UBE2T
mcTEC
FOSB
MAFF
PEG10
EGR1
KANK2
PPP1R15A
AKAP12
APLP2
GJB6
MEG3
ZFP36
CCL2
TDGF1
MYADM
TIMP3
EGR2
NR4A1
FOS
JUNB
THBS1
MCL1
H3F3B
EGR3
CCNL1
GADD45B
ID3
SERTAD1
SRPX
TPM4
IRF1
CEBPD
RBBP8
EDNRA
PLK2
CSRNP1
IER2
NFKBID
RPL7
TGM2
CALD1
DUSP6
TAGLN
FERMT2
NFKBIZ
P3H2
CYR61
PNRC2
cTEC
PRSS16
PITHD1
TBATA
GNG11
CTSV
PGAM2
CCL25
PEMT
OXCT1
PLTP
CST3
PSMB11
CDC42EP5
SLC46A2
COX7A1
TP53AIP1
LY75
HMG20B
SNX29
SCX
CXCL12
RAB42
FAM107A
TP53I3
FRMD1
GAA
ETFB
CD83
GAS6
C20orf204
CLIC3
METTL26
SOD3
SYNE1
FABP5
FAM50A
AC084816.1
CSTB
PLGRKT
PSIP1
CYP26B1
CLEC2L
ATP10B
BCAS4
PNMA8A
ETNK1
KCNIP3
PAX1
MDK
DYSF
mTECI
CCL19
KRT15
CLU
KRT13
CCL21
CH25H
IFITM1
IFITM3
CXCL14
LTB
IFI6
FN1
KRT17
SFN
BST2
MX1
TNC
CD9
ANGPT2
XAF1
IFI44L
SH3BP5
CCDC3
KRT19
BCAM
B2M
IL32
S100A11
ACKR1
KRT5
HLA-A
TMSB4X
ECE1
GABRA5
ALPK2
DCC
PPP2R2C
RPL28
LY6E
HLA-B
VIM
NPR3
S100A6
ARID5B
TMEM173
SGK1
PCBD1
IFI27
SYNPO2
TYW3
mTECII
CLDN3
CSTA
CALML5
VIM
NTHL1
FABP6
ADIRF
AIRE
CLDN4
LSP1
TMSB4X
SNCG
SRGN
HLA-DPA1
FXYD3
FXYD2
HLA-DRA
HLA-DPB1
SPIB
LTF
CYBA
CTSH
TSPO
GSN
NPB
LY6D
RAB11FIP1
CLEC7A
PLAC8
PRRX1
DEFB4A
INSM1
DLX5
MARCO
PARM1
MYBPC1
CCL27
CD70
JCHAIN
FEZF2
IL2RG
FYB1
SLC9A3R1
CTSS
FCER2
DAPL1
KRT7
PLEK
GABRA5
RAMP1
mTECIII/IV
PI3
SPINK5
KRT1
KRTDAP
CALML5
SERPINB3
LY6D
LYPD2
SERPINB4
SPRR1B
S100P
SBSN
APOBEC3A
PHLDA2
DEFB1
KRT23
IVL
PSORS1C2
FLG
KRT4
LCN2
CST6
SERPINB13
PYDC1
SPRR1A
SLURP2
NCCRP1
LY6G6C
IGFL2-AS1
NECTIN4
TMEM40
CDKN2B
CXCL17
PLA2G2F
MUC16
A2ML1
CYP4B1
SERPINB2
RHCG
SPRR3
ASPG
CDKN2A
IL1RN
ALDH3B2
FAM3D
MALL
CASP14
SCGB2A1
IGFL1
SERPINB12
TEC myo/neuro
ACTC1
TTN
MYH3
ACTA1
NEB
TNNC2
TNNI1
MYL4
TNNC1
MYL1
CKM
MYOG
DES
KLHL41
AC020909.2
MAP1B
CD24
TUBB2B
NES
SLN
STMN2
CHGB
PCBP4
NEUROD1
ARHGAP36
GNG8
RTN1
PCSK1N
MYBPH
SMPX
COX6A2
RBM24
KLHL35
TAGLN3
ZEB2
NHLH1
LDB3
HSPB3
HIGD1B
MB
CASQ2
DUSP26
ACTN2
STAC3
POU4F1
CELA3A
IGSF1
CHRNA1
NELL1
GAP43
Parathyroid
PTH
NRN1
GCM2
CASR
PVALB
AL357497.1
CD109
ZG16B
GATA3-AS1
WDR86
CYB5R2
TBX1
PPP1R1A
RD3L
CORIN
PNMT
LIM2
SYCP2L
ETV4
PPY
PKIB
AC098829.1
CHGA
VDR
KCNJ16
FOXL2
CLDN9
CCNA1
GATA3
FHL1
RASAL1
SOX13
SLC4A3
MALL
THSD7A
AC116614.1
RGL3
GPR160
HBD
ITGA1
ERBB4
TMEM200B
BAIAP3
ECHDC3
GCNT1
CCDC151
C4orf48
NPR1
BSPRY
KL
Cycling TEC
mcTEC
cTEC
mTECI
mTECII
mTECIII/IV
TEC myo/neuro
Parathyroid
Avg. Exp.
% Exp.

Supplementary Figure S7

Dot plots of differentially expressed genes for thymic epithelial and parathyroid clusters across all sampled developmental time points (transcription factors are labeled in bold).

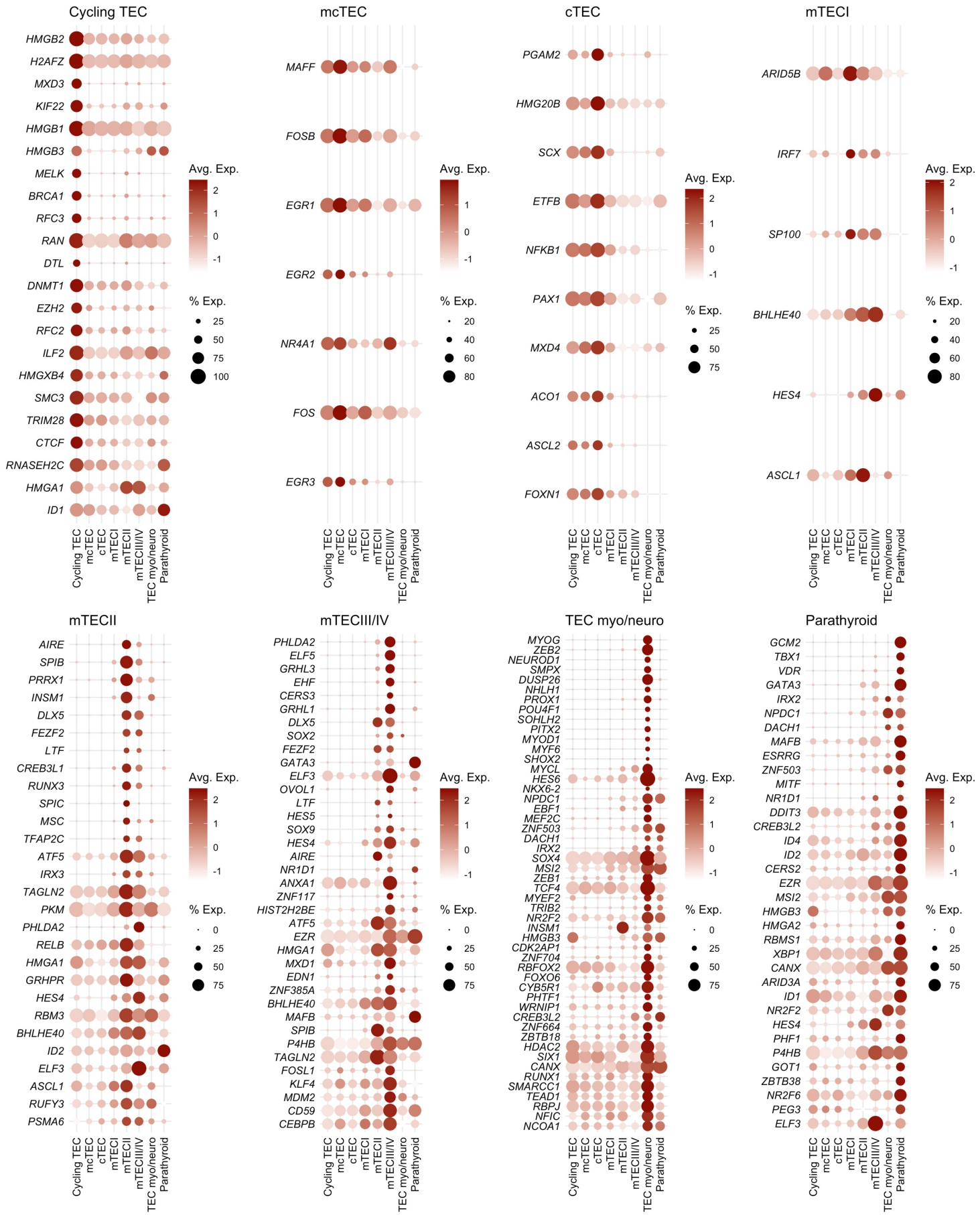
Cycling TEC
HMGB2
H2AFZ
MXD3
KIF22
HMGB1
HMGB3
MELK
BRCA1
RFC3
RAN
DTL
DNMT1
EZH2
RFC2
ILF2
HMGXB4
SMC3
TRIM28
CTCF
RNASEH2C
HMGA1
ID1
mcTEC
MAFF
FOSB
EGR1
EGR2
NR4A1
FOS
EGR3
cTEC
PGAM2
HMG20B
SCX
ETFB
NFKB1
PAX1
MXD4
ACO1
ASCL2
FOXN1
mTECI
ARID5B
IRF7
SP100
BHLHE40
HES4
ASCL1
mTECII
AIRE
SPIB
PRRX1
INSM1
DLX5
FEZF2
LTF
CREB3L1
RUNX3
SPIC
MSC
TFAP2C
ATF5
IRX3
TAGLN2
PKM
PHLDA2
RELB
HMGA1
GRHPR
HES4
RBM3
BHLHE40
ID2
ELF3
ASCL1
RUFY3
PSMA6
mTECIII/IV
PHLDA2
ELF5
GRHL3
EHF
CERS3
GRHL1
DLX5
SOX2
FEZF2
GATA3
ELF3
OVOL1
LTF
HES5
SOX9
HES4
AIRE
NR1D1
ANXA1
ZNF117
HIST2H2BE
ATF5
EZR
HMGA1
MXD1
EDN1
ZNF385A
BHLHE40
MAFB
SPIB
P4HB
TAGLN2
FOSL1
KLF4
MDM2
CD59
CEBPB
TEC myo/neuro
MYOG
ZEB2
NEUROD1
SMPX
DUSP26
NHLH1
PROX1
POU4F1
SOHLH2
PITX2
MYOD1
MYF6
SHOX2
MYCL
HES6
NKX6-2
NPDC1
EBF1
MEF2C
ZNF503
DACH1
IRX2
SOX4
MSI2
ZEB1
TCF4
MYEF2
TRIB2
NR2F2
INSM1
HMGB3
CDK2AP1
ZNF704
RBFOX2
FOXO6
CYB5R1
PHTF1
WRNIP1
CREB3L2
ZNF664
ZBTB18
HDAC2
SIX1
CANX
RUNX1
SMARCC1
TEAD1
RBPJ
NFIC
NCOA1
Parathyroid
GCM2
TBX1
VDR
GATA3
IRX2
NPDC1
DACH1
MAFB
ESRRG
ZNF503
MITF
NR1D1
DDIT3
CREB3L2
ID4
ID2
CERS2
EZR
MSI2
HMGB3
HMGA2
RBMS1
XBP1
CANX
ARID3A
ID1
NR2F2
HES4
PHF1
P4HB
GOT1
ZBTB38
NR2F6
PEG3
ELF3
Avg. Exp.
% Exp.
Cycling TEC
mcTEC
cTEC
mTECI
mTECII
mTECIII/IV
TEC myo/neuro
Parathyroid

Supplementary Figure S8

Dot plots of differentially expressed transcription factors for thymic epithelial and parathyroid clusters across all sampled developmental time points.

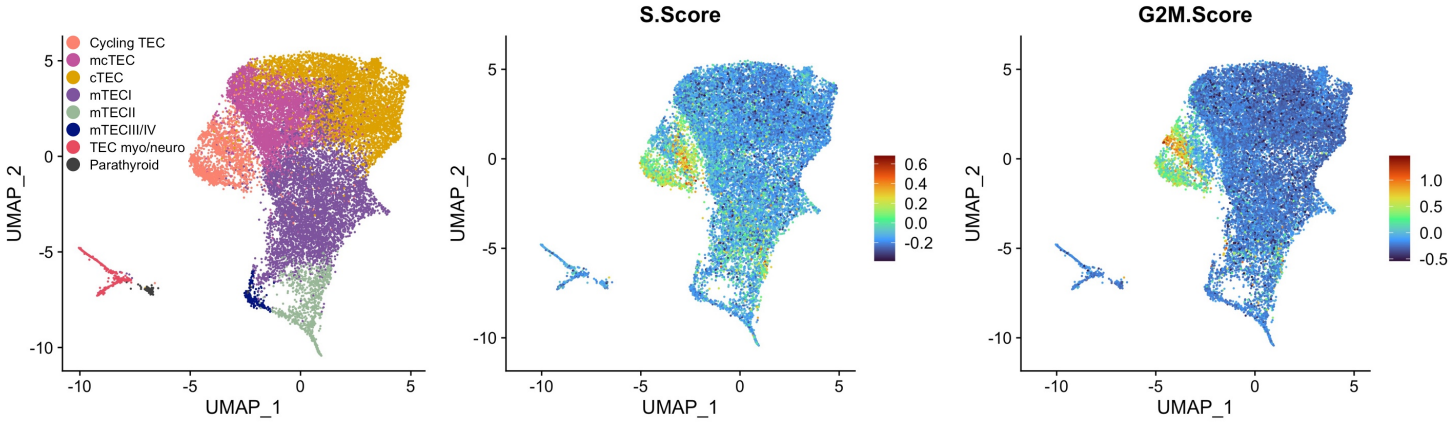
Cycling TEC
mcTEC
cTEC
mTECI
mTECII
mTECIII/IV
TEC myo/neuro
Parathyroid
UMAP_2
UMAP_1
S.Score
0.6
0.4
0.2
0.0
-0.2
G2M.Score
1.0
0.5
0.0
-0.5

Supplementary Figure S9

UMAP visualization of TECs across all sampled developmental time points colored by Seurat S and G2M phase scores.

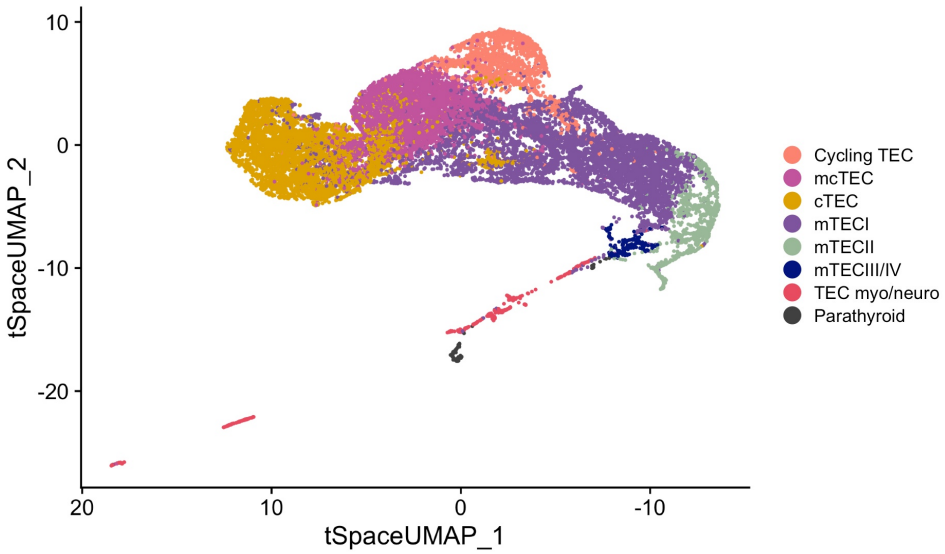
10
0
-10
-20
tSpaceUMAP_2
20
10
0
-10
tSpaceUMAP_1
Cycling TEC
mcTEC
cTEC
mTECI
mTECII
mTECIII/IV
TEC myo/neuro
Parathyroid

Supplementary Figure S10

tSpace UMAP visualization of all integrated TECs from embryonic, fetal and postnatal stages of development.

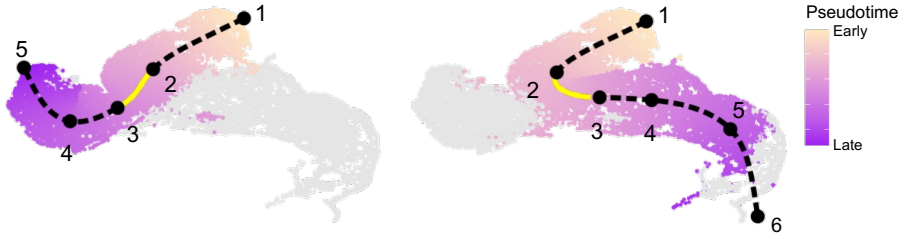
1
2
3
4
5
6
Pseudotime
Early
Late

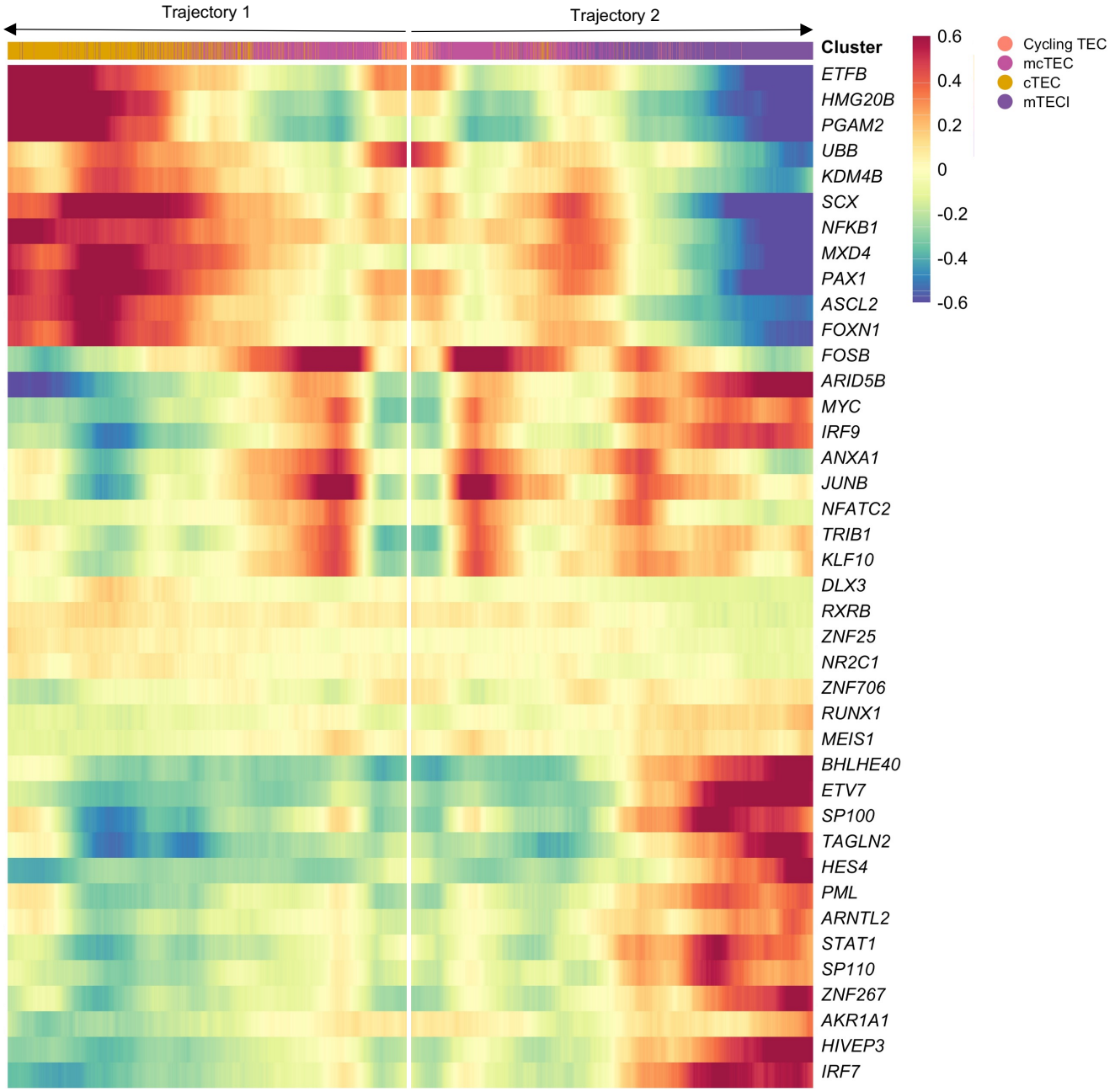
Trajectory 1
Trajectory 2
Cluster
Cycling TEC
mcTEC
cTEC
mTECI
0.6
0.4
0.2
0
-0.2
-0.4
-0.6
ETFB
HMG20B
PGAM2
UBB
KDM4B
SCX
NFKB1
MXD4
PAX1
ASCL2
FOXN1
FOSB
ARID5B
MYC
IRF9
ANXA1
JUNB
NFATC2
TRIB1
KLF10
DLX3
RXRB
ZNF25
NR2C1
ZNF706
RUNX1
MEIS1
BHLHE40
ETV7
SP100
TAGLN2
HES4
PML
ARNTL2
STAT1
SP110
ZNF267
AKR1A1
HIVEP3
IRF7

Supplementary Figure S11

Subset of tSpace UMAP from Fig. 6B with cortical and medullary trajectories separately colored by pseudotime. Pseudotime intervals (knots) identified by TradeSeq are superimposed and numbered chronologically (top). Heatmaps representing the rolling average of the top 40 differentially expressed transcription factors between knots 2 and 3 along trajectories 1 and 2 (bottom).

A

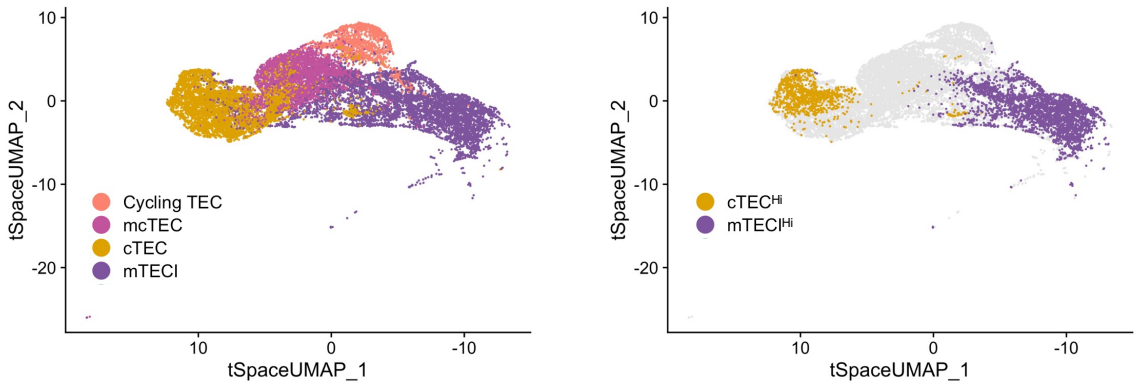
Cycling TEC
mcTEC
cTEC
mTECI
cTEC^{Hi}
mTECI^{Hi}
tSpaceUMAP_1
tSpaceUMAP_2

B

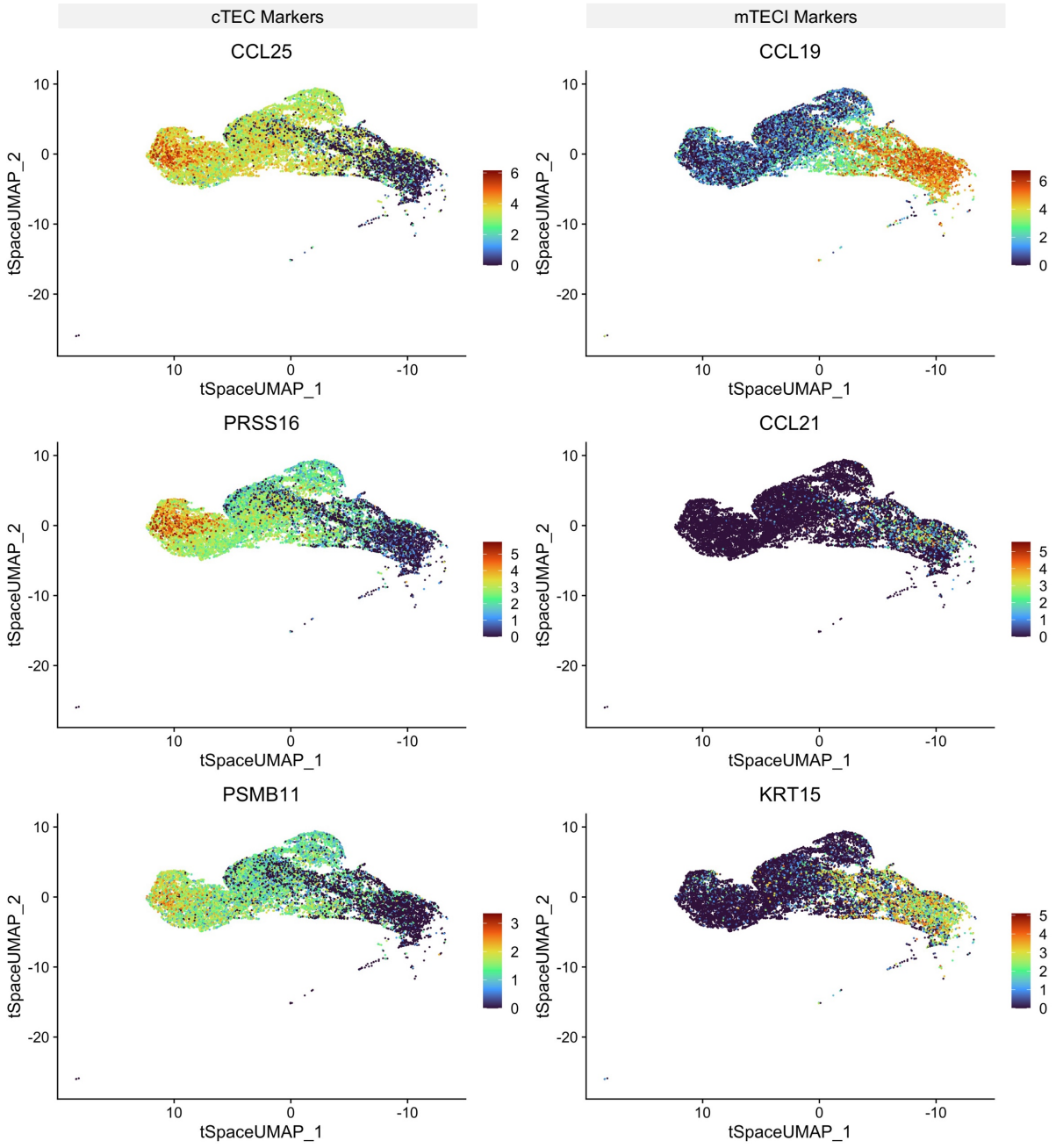
cTEC Markers
mTECI Markers
CCL25
CCL19
PRSS16
CCL21
PSMB11
KRT15
tSpaceUMAP_1
tSpaceUMAP_2

Supplementary Figure S12

(A) tSpace UMAP visualization of integrated TECs from embryonic, fetal and postnatal stages of development. mTECII, mTECIII/IV, TECmyo/neuro, and parathyroid epithelial cells not visualized (left). tSpace UMAP highlighted by populations with high canonical lineage marker expression (right). **(B)** tSpace UMAP with superimposed canonical cTEC and mTECI marker expression.

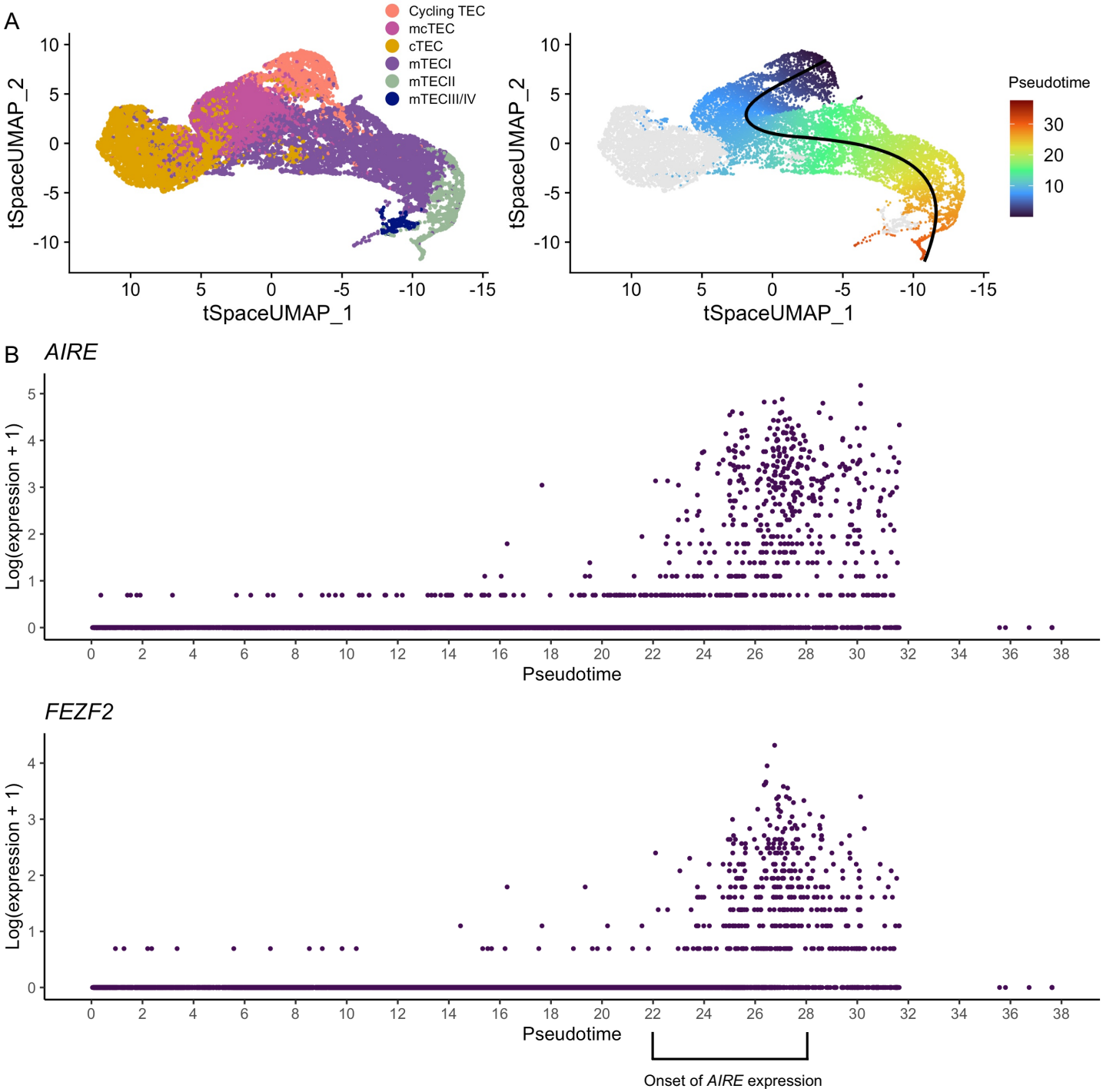
A
Cycling TEC
mcTEC
cTEC
mTECI
mTECII
mTECIII/IV
tSpaceUMAP_2
tSpaceUMAP_1
Pseudotime
B
AIRE
FEZF2
Log(expression + 1)
Pseudotime
Onset of AIRE expression

Supplementary Figure S13

(A) tSpace UMAP from Fig. 6B colored by cell type (left) and pseudotime values along the extended medullary trajectory (right). **(B)** Gene expression of cells along pseudotime of the extended medullary trajectory.

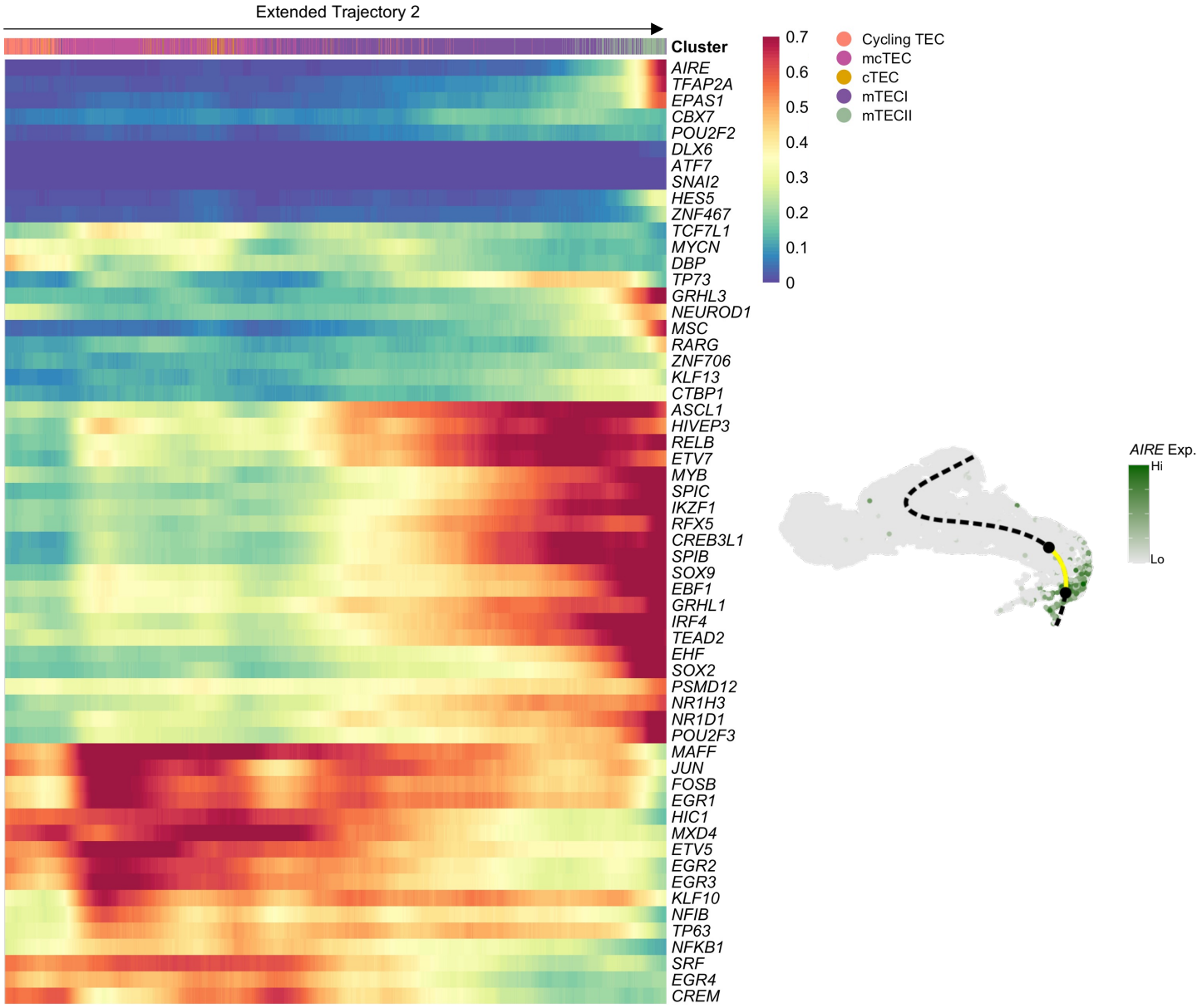
Extended Trajectory 2
Cluster
AIRE
TFAP2A
EPAS1
CBX7
POU2F2
DLX6
ATF7
SNAI2
HES5
ZNF467
TCF7L1
MYCN
DBP
TP73
GRHL3
NEUROD1
MSC
RARG
ZNF706
KLF13
CTBP1
ASCL1
HIVEP3
RELB
ETV7
MYB
SPIC
IKZF1
RFX5
CREB3L1
SPIB
SOX9
EBF1
GRHL1
IRF4
TEAD2
EHF
SOX2
PSMD12
NR1H3
NR1D1
POU2F3
MAFF
JUN
FOSB
EGR1
HIC1
MXD4
ETV5
EGR2
EGR3
KLF10
NFIB
TP63
NFKB1
SRF
EGR4
CREM
0.7
0.6
0.5
0.4
0.3
0.2
0.1
0
Cycling TEC
mcTEC
cTEC
mTECI
mTECII
AIRE Exp.
Hi
Lo

Supplementary Figure S14

Heatmap representing the rolling average expression of all transcription factor regulons with differential expression ($p<0.05$) along highlighted pseudotime region superimposed on tSpace UMAP from Fig. 6B.

Supplementary Table S1. metadata for sequenced samples

Sample ID	Organ	Age	Number of Cells	Mean Counts Per Cell	Mean Genes Per Cell	Median Mito Percentage	Gender	Tissue processing
C40_TH_TOT_2	Thymus	Post Conception Week 7	7180	11139	3054.5	1.97	Female	All cells
C40_TH_TOT_1	Thymus	Post Conception Week 7	6841	11293.8	3098.1	1.97	Female	All cells
C41_TH_TOT_2	Thymus	Post Conception Week 6	5789	14190.5	3544.9	2.61	Male	All cells
C41_TH_TOT_1	Thymus	Post Conception Week 6	5620	14244.3	3547.6	2.52	Male	All cells
KGW1_TH_EPCAM_45	Thymus	Post Conception Week 16	3046	21747	4135	7.29	Male	EPCAM positive selection, CD45 depletion
F83_TH_EPCAM	Thymus	Post Conception Week 17	3678	9575.2	2634.2	2.55	Female	EPCAM FACS sorted
KGW2_TH_EPCAM_45	Thymus	Post Conception Week 17	7634	11754	2993	6.81	Female	EPCAM positive selection, CD45 depletion
KGW3_TH_EPCAM_45	Thymus	Post Conception Week 18	8648	9349	2721	5.73	Male	EPCAM positive selection, CD45 depletion
T07_TH_EPCAM_S3	Thymus	3 Months Postnatal	3149	11355.6	2819.6	3.86	Male	EPCAM FACS sorted
KGW4_B_EPCAM	Bronchus	Post Conception Week 16	5920	15651	3525	7.69	Male	EPCAM positive selection
KGW5_B_EPCAM	Bronchus	Post Conception Week 17	4376	16449	3188	8.56	Female	EPCAM positive selection
KGW6_B_EPCAM	Bronchus	Post Conception Week 18	7414	15387	2979	9.43	Male	EPCAM positive selection
KGW7_L_EPCAM	Lung	Post Conception Week 16	3726	20366	3862	7.95	Male	EPCAM positive selection
KGW8_L_EPCAM	Lung	Post Conception Week 17	7075	11074	2810	8.11	Female	EPCAM positive selection
KGW9_L_EPCAM	Lung	Post Conception Week 18	7208	12965	3254	7.12	Male	EPCAM positive selection
KGW10_E_EPCAM	Esophagus	Post Conception Week 16	4603	16004	3513	7	Male	EPCAM positive selection
KGW11_E_EPCAM	Esophagus	Post Conception Week 17	6464	11431	2723	8.48	Female	EPCAM positive selection

Supplementary Table S1

Sample metadata. [Sample ID] TH: Thymus, B: Bronchus, L: Lung, E: Esophagus

Supplementary Table S2. Cluster markers			
Organ	**Tissue**	**Cell Type**	**Markers**
Thymus	Epithelial	mcTEC	*CTGF, DLK2*
Thymus	Epithelial	cTEC	*CCL25, PSMB11, KRT8*
Thymus	Epithelial	mTECI	*CCL19, KRT5, KRT14*
Thymus	Epithelial	mTECII	*AIRE, CLDN4*
Thymus	Epithelial	mTECIII/mTECIV	*KRT1, POU2F3*
Thymus	Epithelial	TECneuro	*NEUROD1, CHGA*
Thymus	Epithelial	TECmyo	*MYOD1, CHRNA1*
Thymus	Immune	Double-Negative Thymocytes	*TRDS, PTPRC, CD3D*
Thymus	Immune	Single-Positive/Double-Positive Thymocytes	*PTPRC, CD3D, CD4, CD8A, CD8B*
Thymus	Immune	Macrophage	*S100A9, RETN*
Thymus	Immune	Dendritic	*LAMP3*
Thymus	Mesenchymal	Fibroblast 1	*PDGFRA, ALDH1A2*
Thymus	Mesenchymal	Fibroblast 2	*FBN1*
Thymus	Endothelial	Vascular Endothelial	*PECAM1, CDH5, AQP1*
Thymus	Endothelial	Lymphatic Endothelial	*PROX1*
Thymus	Neuronal	Neuronal	*NRXN1*
Bronchus	Epithelial	Epithelial Basal	*KRT15, IL33, DLK2*
Bronchus	Epithelial	Club	*SCGB1A1, BPIFA1*
Bronchus	Epithelial	Goblet	*MUC5B, BPIFB1*
Bronchus	Epithelial	Submucosal Gland	*LTF*
Bronchus	Epithelial	Secretory Progenitor	*SFTPB, SCGB3A2*
Bronchus	Epithelial	Multiciliated	*FOXJ1, PIFO*
Bronchus	Epithelial	Bud Tip Progenitor	*SFTPC, SOX9*
Bronchus	Myoepithelial	Myoepithelial	*EPCAM, ACTA2*
Bronchus	Immune	T Cell	*PTPRC, CD3D*
Bronchus	Immune	B Cell	*PTPRC, MS4A1*
Bronchus	Immune	Macrophage	*PTPRC, S100A9, RETN*
Bronchus	Mesenchymal	Vascular Smooth Muscle	*PDGFRB, ACTA2*
Bronchus	Mesenchymal	Smooth Muscle	*ACTA2, DES*
Bronchus	Mesenchymal	Fibroblast	*PDGFRA, FBN1*
Bronchus	Mesenchymal	Cartilage	*CNMD*
Bronchus	Endothelial	Vascular Endothelial	*PECAM1, CDH5, AQP1*
Bronchus	Neuronal	Neuronal	*NRXN1*
Lung	Epithelial	Bud Tip Progenitor	*SFTPC, SOX9*
Lung	Epithelial	Bud Tip Progenitor Adjacent	*AGER, SFTPB*
Lung	Epithelial	Multiciliated	*FOXJ1, PIFO*
Lung	Epithelial	Secretory Progenitor	*SFTPB, SCGB3A2*
Lung	Epithelial	Epithelial Basal	*KRT15, IL33, DKL2*
Lung	Epithelial	Neuroendocrine	*CHGA*
Lung	Immune	T Cell	*PTPRC, CD3D*
Lung	Immune	B Cell	*PTPRC, MS4A1*
Lung	Immune	Macrophage	*PTPRC, S100A9, RETN*
Lung	Mesenchymal	Fibroblast	*PDGFRA, FBN1*
Lung	Mesenchymal	Mesothelial	*MSLN*
Lung	Mesenchymal	Vascular Smooth Muscle	*PDGFRB, ACTA2*
Lung	Mesenchymal	Smooth Muscle	*ACTA2, DES*
Lung	Endothelial	Vascular Endothelial	*PECAM1, CDH5, AQP1*
Lung	Endothelial	Lymphatic Endothelial	*PROX1*
Lung	Neuronal	Neuronal	*NRXN1*
Esophagus	Epithelial	Epithelial Basal	*KRT15, DLK2, CLDN4*
Esophagus	Epithelial	Suprabasal	*KRT13, KRT4, CLDN4*
Esophagus	Epithelial	Multiciliated	*FOXJ1, PIFO*
Esophagus	Epithelial	Gastric Epithelial	*TFF1, MUC5B*
Esophagus	Immune	T Cell	*PTPRC, CD3D*
Esophagus	Immune	Macrophage	*PTPRC, S100A9, RETN*
Esophagus	Mesenchymal	Fibroblast	*PDGFRA, FBN1*
Esophagus	Mesenchymal	Vascular Smooth Muscle	*PDGFRB, ACTA2*
Esophagus	Mesenchymal	Smooth Muscle	*ACTA2, DES*
Esophagus	Endothelial	Vascular Endothelial	*PECAM1, CDH5, AQP1*
Esophagus	Neuronal	Neuronal	*NRXN1*

Supplementary Table S2

Table contains canonical markers used for cluster annotation.

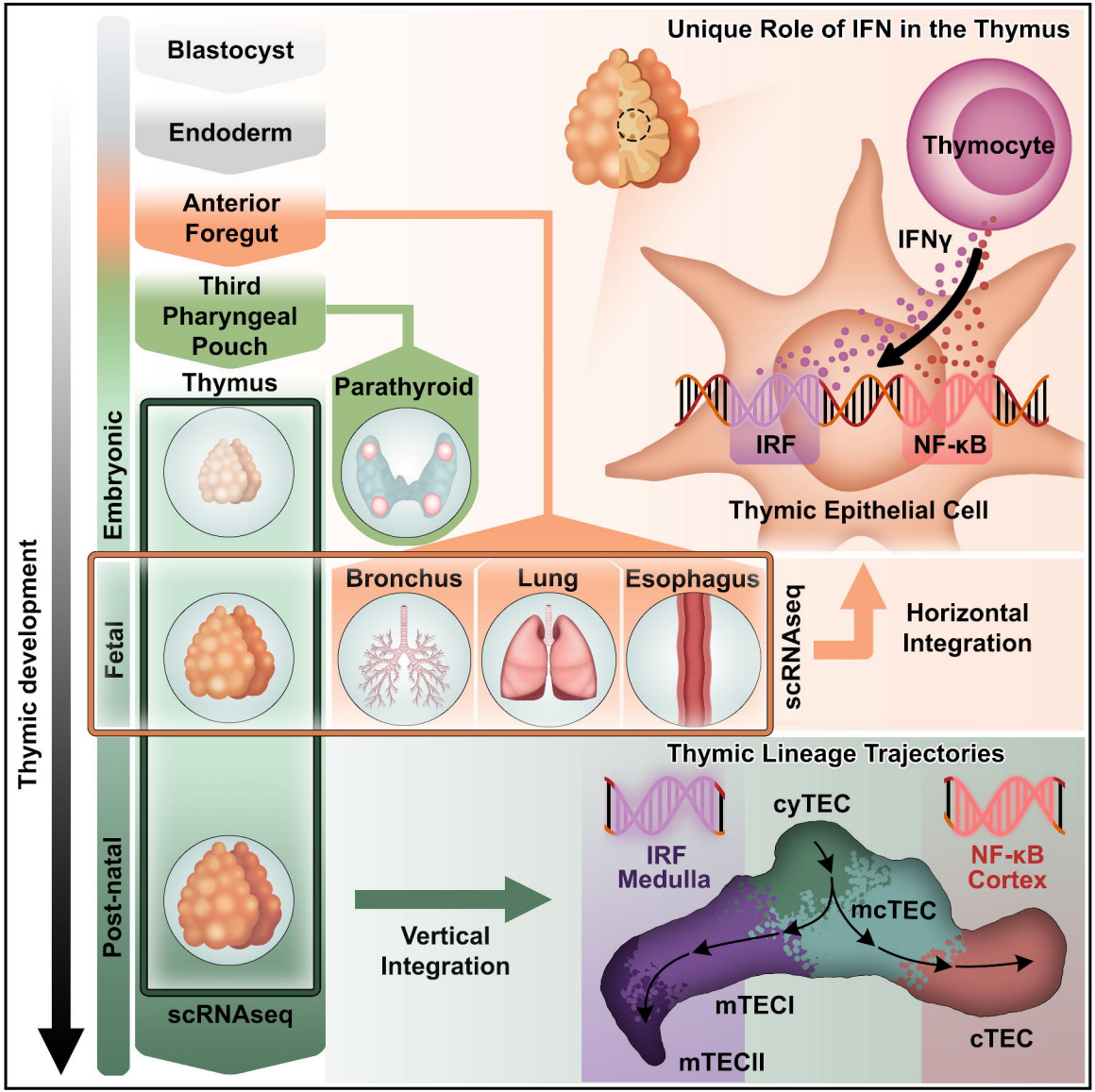
Thymic development
Embryonic
Fetal
Post-natal
Blastocyst
Endoderm
Anterior Foregut
Third Pharyngeal Pouch
Thymus
Parathyroid
Bronchus
Lung
Esophagus
scRNAseq
scRNAseq
Horizontal Integration
Vertical Integration
Unique Role of IFN in the Thymus
Thymocyte
IFNγ
IRF
NF-κB
Thymic Epithelial Cell
Thymic Lineage Trajectories
IRF
Medulla
NF-κB
Cortex
cyTEC
mcTEC
mTECI
mTECII
cTEC